INVESTIGATIONS ON TRANS-LUMINAL PHOTON DIFFUSION IN STEADY-STATE AND FREQUENCY-DOMAIN

By

ANQI ZHANG

Bachelor of Science in Electronic Information Science & Technology
East China Normal University
Shanghai, China
2005

Master of Science in Radio Physics
East China Normal University
Shanghai, China
2008

Submitted to the Faculty of the
Graduate College of the
Oklahoma State University
in partial fulfillment of
the requirements for
the Degree of
DOCTOR OF PHILOSOPHY
December, 2012

INVESTIGATIONS ON TRANS-LUMINAL PHOTON DIFFUSION IN STEADY-STATE AND FREQUENCY-DOMAIN

Dissertation Approved:

Dr. Daqing Piao

Dissertation Adviser

Dr. Charles F. Bunting

Dr. Weili Zhang

Dr. Jiahong Wu

Outside Committee Member

Dr. Sheryl A. Tucker

Dean of the Graduate College

ACKNOWLEDGEMENTS

Firstly I want to express my deep gratitude to my advisor Dr. Daqing Piao, who introduced this splendid field to me. During my more than four year's Ph.D. study, Dr. Piao guides me through my stumbling learning progress and helps me overcome every pitfall during my study. His persistent enthusiasm for knowledge has kept me engaged for research and made this dissertation possible. His kindness also makes my stay at OSU a cherishable memory.

I also need to thank Dr. Charles F. Bunting who inspires me with his personality and way of teaching, not to mention the knowledge of Electromagnetic I learnt from him.

I thank Dr. Weili Zhang for his support in my department and Dr. Jiahong Wu especially for his help on my Mathematics.

My thanks also extend to my former and current colleagues: Zhen Jiang, Guan Xu, Wei Sun, Yuanyuan Jiang and Sovanlal Mukherjee for their help on my research.

Above ground, I am greatly indebted to my father Peiyi Zhang, my mother Yuhua Gao for their never-ending support and my parents in-law Cilin Li and Jinlian Ouyang for their unswervingly love. Finally I want to thank my wife Shan Li, who blesses my life with bright light during every piece of darkness I have encountered.

The research projects have been supported by U.S. Army Medical Research Acquisition Activity grant #W81XWH-10-1-0836.

Name: ANQI ZHANG

Date of Degree: DECEMBER, 2012

Title of Study: INVESTIGATIONS ON TRANS-LUMINAL PHOTON DIFFUSION IN STEADY-STATE AND FREQUENCY-DOMAIN

Major Field: ELECTRICAL ENGINEERING

ABSTRACT:

This work presents the study of photon diffusion in a homogenous medium bounded externally (known as "concave") or internally (known as "convex") by an infinitely long circular cylindrical applicator. Focusing initially on steady-state condition, the photon diffusion in these two geometries is solved in cylindrical coordinates. The analytic solutions and their approximations are evaluated numerically for two specific cases: (1) the detector is placed only azimuthally with respect to the source and (2) the detector is placed only longitudinally with respect to the source. The effect of the applicator's curvature and radius on the photon fluence rate in comparison to that in the semi-infinite geometry is demonstrated qualitatively. The developed analytics are then examined through three approaches: (a) finite-element-method (FEM), (b) Monte Carlo (MC) simulation, and (c) experimental measurement. Despite that these quantitative examinations have to be conducted for applicators with large length-to-radius ratio to approximate the infinite-length condition modeled in the analytics, the results obtained for two "concave" and three "convex" applicator dimensions validated the quantitative accuracy of the analytic treatments in the diffusion regime. This work further demonstrates analytically for large radius applicator and verifies numerically using FEM and MC methods for small radius applicator the phenomenon that on the tissue-applicator interface of either "concave" or "convex" geometry there exists a unique set of spiral-paths, along which the steady-state photon fluence rate decays at a rate equal to that along a straight-line in a planar semi-infinite geometry. It is also found that for the medium containing an anomaly that is aligned azimuthally with the spiral-paths and has either positive or negative contrast of absorption or scattering coefficient over the background medium, the photon

fluence rate along the homogenous-medium associated spiral-paths is macroscopically indistinguishable from, and microscopically close to, that along a straight line in a semi-infinite geometry. The last chapter of this work provides the frequency-domain analysis of the photon diffusion in both “concave” and “convex” geometries. Employing the same methodology as that in the steady-state study, such physical quantities as the amplitude of AC photon fluence, the modulation depth and the phase are explicitly studied.

TABLE OF CONTENTS

LIST OF TABLES

LIST OF FIGURES

CHAPTER 1

BACKGROUND AND OVERVIEW

1.1 Diffusion regime and diffusion approximation

This work follows the notations used by Wang and Wu (Wang et al., 2007). The basic tissue optical properties are shown in Table 1. These properties yield the transport properties used in diffusion theory as given in Table 2. In discussing light transport, the following parameters are used: $\Phi(\vec{r},t)$ refer to photon fluence rate [W/m^2], $F(\vec{r})$ refer to the photon fluence [J/m^2], which is defined as the time-integrated fluence rate.

Table 1. Basic optical properties

Parameter	Symbol	Units
Absorption coefficient	μ_a	cm^{-1}
Scattering coefficient	μ_s	cm^{-1}
Anisotropy	g	dimensionless
Index of refraction	n	dimensionless

Table 2. Transport properties used in diffusion theory

Parameter	Symbol	Units
Reduced scattering coefficient	$\mu_s' = \mu_s(1-g)$	cm^{-1}
Transport mean free path	$l_t' = 1/(\mu_a + \mu_s')$	cm
Diffusion coefficient	$D = 1/[3(\mu_a + \mu_s')]$	cm
Optical penetration depth	$\delta = \sqrt{D/\mu_a}$	cm

The cumulative effect of photon absorption and scattering in biological tissue could be classified into two regimes: non-diffusion regime and diffusion regime (Jacques et al., 2008). When photons are delivered as a collimated beam into a medium, they have a direction of movement, known as ballistic photons. As the photons are scattered by interaction within a tissue, they lose their directionality and hence become eligible for diffusion.

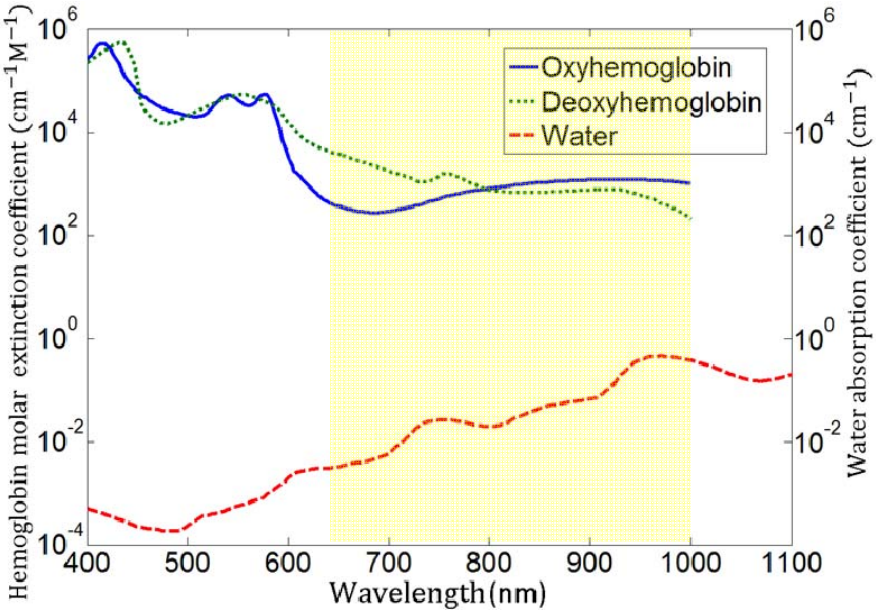

Fig. 1 Absorption spectrum of primary biological absorbers (Melanin not shown). (Wang et al., 2007)

The photon diffusion equation is expressed by (Wang et al., 2007; Jacques et al., 2008; Fantini et al., 1994; Arridge et al., 1992; Haskell et al., 1994; Contini et al., 1997):

$$\frac{\partial\Phi(\vec{r},t)}{c\partial t}+\mu_a\Phi(\vec{r},t)-\nabla\cdot\left[D\nabla\Phi(\vec{r},t)\right]=S(\vec{r},t) \qquad (1.1.1)$$

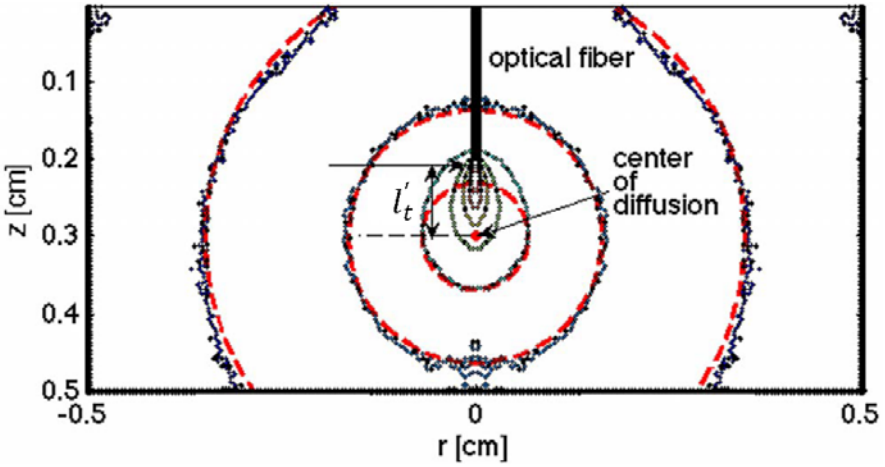

Fig. 2 Monte Carlo simulation of photons launched as collimated beams from optical fibers. The light appears to diffuse from a central point located one l_t' in front of the delivery fiber (red dot at $r = 0$, $z = 0.3cm$). Iso-concentration contours based on Monte Carlo are drawn as black dots and black line. Dashed red circular lines centered around the center of diffusion indicate the prediction of diffusion theory. Near the source, diffusion theory does not agree with the Monte Carlo simulation, but distant from the source agreement is good. The mismatched air/medium boundary at $z = 0$ slightly distorts the iso-concentration curves of the Monte Carlo simulation, so Monte Carlo and dashed lines of diffusion theory do not exactly match. (Optical properties: $\mu_a = 0.1cm^{-1}$, $\mu'_s = 100\,cm^{-1}$, $g = 0.90$, $n = 1.4$.)

where c is the speed of light and $S(\vec{r},t)$ is the source distribution. One approximation is made in the derivation of the diffusion equation: $\mu_s' >> \mu_a$. Most biological tissues are characterized by strong optical scattering and are referred to as either *scattering media* or *turbid media*. By contrast, the absorption originating mainly from hemoglobin, melanin, and water is weak in the

near-infrared spectral region as illustrated in Fig. 1. Melanin absorbs ultraviolet (UV) light strongly but longer-wavelength light less, and due to its complicated feature, it is not shown in Fig. 1. Hence, the approximation for deriving the diffusion equation is satisfied. In addition, it is also required that the observation point be sufficiently far from sources and boundaries.

Figure 2 compares the Monte Carlo simulation and diffusion theory descriptions of the distribution of light in an infinite medium where light is delivered as a collimated beam by an optical fiber submerged in the light scattering medium (Jacques et al., 2008). The figure illustrates that in a local region near the source, diffusion theory fails to accurately describe the light distribution. However, when distant from the source, diffusion theory is quite good, as if the collimated photons had been thrown forward by the optical fiber one transport mean free path l_t' in front of the fiber, and the diffusion process had emanated from this location.

1.2 Steady-state multi-wavelength near-infrared diffuse optical tomography

In steady-state also known as continuous wave (CW) domain, the diffusion equation becomes:

$$\mu_a \Phi(\vec{r}) - \nabla \cdot [D \nabla \Phi(\vec{r})] = S(\vec{r}) \tag{1.2.1}$$

In Eq. (1.2.1), μ_a and D are unknown and $\Phi(\vec{r})$ is also generally not known, except possible at a finite number of measurement sites. The basic idea for determining μ_a and D is to make measurements of optical quantities around or at part of the perimeter of the tissue volume for a set of known optical excitation positions. Denoting the measured photon fluence rate by $\Phi^M(\widetilde{D}, \widetilde{\mu}_a)$ and the calculated data using the forward solver by $\Phi^C(D, \mu_a)$, where $(\widetilde{D}, \widetilde{\mu}_a)$ and (D, μ_a) represent actually distributions and assumed or updated distributions in the investigated region, a discrete set of measured photon fluence rate can be expressed as based on Taylor expansion (Paulsen et al., 1995):

$$\Phi^M\left(\tilde{D},\tilde{\mu}_a\right)=\Phi^C\left(D,\mu_a\right)+\frac{\partial\Phi}{\partial D}\delta D+\frac{\partial\Phi}{\partial\mu_a}\delta\mu_a \tag{1.2.2}$$

, in which the assumed or updated optical property distributions $\left(D,\mu_a\right)$ are assumed to be close to the true profiles $\left(\tilde{D},\tilde{\mu}_a\right)$. Equation (1.2.2) leads to:

$$\delta\Phi = J\cdot\delta\mu \tag{1.2.3}$$

where

$$\delta\Phi = \Phi^M\left(\tilde{D},\tilde{\mu}_a\right)-\Phi^C\left(D,\mu_a\right) \tag{1.2.4}$$

$$J=\left[\frac{\partial\Phi}{\partial D}\quad\frac{\partial\Phi}{\partial\mu_a}\right] \tag{1.2.5}$$

$$\delta\mu=\begin{bmatrix}\delta D\\ \delta\mu_a\end{bmatrix} \tag{1.2.6}$$

The J is known as the Jacobian matrix and also referred to as the weight or sensitivity matrix. Based on Eq. (1.2.3) and solving it as an iterative scheme via Levenberg-Marquardt (LM) procedure gives (Dehghani et al., 2009):

$$\left(J^TJ+\overline{\lambda}I\right)^{-1}J^T\delta\Phi=\delta\mu \tag{1.2.7}$$

where λ is the Tikhonov regularization parameter. The μ_a and μ_s' distribution can be obtained based on calculated $\left(D,\mu_a\right)$.

However, the intrinsic pathophysiological processes such as angiogenesis and hypoxia are directly related to the physiological states of the tissue volume such blood oxygenation and chromophore concentrations, instead of absorption and scattering coefficient. By making measurements at multiple wavelengths, the chromophore concentrations can be calculated by

$$\left[\mu_a\right]=\left[\varepsilon\right]\cdot\left[C\right] \tag{1.2.8}$$

where $[\varepsilon]$ is the molar absorption spectra of the tissue's absorbing chromophores and $[C]$ is the concentration of these chromophores. Similarly, the scatter amplitude a and scatter power b can be obtained by

$$\mu_s' = a\lambda^{-b} \tag{1.2.9}$$

Instead of reconstructing for optical properties at each wavelength and then applying Eq. (1.2.8) and Eq. (1.2.9) in a post-processing step, these constrains can be incorporated into the reconstruction directly to estimate chromophore concentrations, scatter amplitude and scatter power and greatly reduces the ill-posedness of the inverse problem and leads to more determinant reconstruction results. For instance, considering oxy-hemoglobin (HbO_2), deoxy-hemoglobin (Hb) and water as the main absorbers in investigated tissue volumes and measuring at 7 wavelengths, the parameter space is reduced from 14 unknown parameters (μ_a and μ_s' at seven wavelengths) to 5 unknown parameters (C_{HbO_2}, C_{Hb}, C_{Water}, a and b) (Srinivasan et al., 2005). This scheme is also called "*spectral constraint case*". In the *spectral constraint case*, the Jacobian in Eq. (1.2.7) now relates the changes in concentrations and scattering parameters directly to changes in measurements. The new Jacobian becomes (Dehghani et al., 2009; Srinivasan et al., 2005)

$$J_{c,\lambda} = \left.\frac{\partial \Phi}{\partial C}\right|_{\lambda} = \left.\frac{\partial \Phi}{\partial \mu_a}\varepsilon\right|_{\lambda} = J_{\mu_a,\lambda} \otimes \left(\varepsilon_{\lambda}^{C_1,C_2,C_3}\right) \tag{1.2.10}$$

$$J_{a,\lambda} = \left.\frac{\partial \Phi}{\partial a}\right|_{\lambda} = \left.\frac{\partial \Phi}{\partial D}\frac{\partial D}{\partial a}\right|_{\lambda} = J_D\left(-3D^2\right)\left(\lambda^{-b}\right)\Big|_{\lambda} \tag{1.2.11}$$

$$J_{b,\lambda} = \left.\frac{\partial \Phi}{\partial b}\right|_{\lambda} = \left.\frac{\partial \Phi}{\partial D}\frac{\partial D}{\partial b}\right|_{\lambda} = J_D\left(-3D^2\right)\left(\mu_s'\right)\left(-\ln\lambda\right)\Big|_{\lambda} \tag{1.2.12}$$

1.3 Trans-luminal analytic model of photon diffusion

Using near-infrared (NIR) light to image large or deep tissue volumes non-invasively has largely been based upon transport modeling with the diffusion approximation to the radiative transport equation (Ishimaru 1989). Non-invasive diffuse optical imaging is always involved with some kind of applicator-tissue interface or air-tissue interface, because the light has to be delivered and detected at the surface of the tissue. For any specific applicator or imaging geometry, the analytic model predicting photon fluence rate to be measured at the applicator/tissue interface dictates the accuracy of calibrating the system using a known homogeneous medium and recovering unknown optical properties of a heterogeneous medium. The analytic solutions to photon diffusion in an infinite homogeneous medium are the least complicated approach, and are solved straightforwardly in spherical coordinates. For a homogenous medium bounded by an infinite plane edge, which conventionally is referred to as the semi-infinite geometry, the analytic solution to photon diffusion is also well-studied (Fantini et al., 1994) and has been applied widely to analyze raw data measured from surface tissue applicators and for image reconstruction.

When NIR light diffusion is utilized for imaging of breast, neonatal brain, joint, rodent, etc., the geometry of the applicator often has a planar or concave (with respect to the direction of source illumination) boundary. One example of breast imaging system is illustrated in Fig. 3 (Pogue et al., 2001; Poplack et al., 2007). When a medium is enclosed by a ring-shape applicator, the photon diffusion within the medium has been modeled as in an infinite medium for a ring applicator of considerable size (Srinivasan et al., 2007). For this type of ring applicator, the photon intensity measured at a site on the applicator interface and 180° to the source may resemble that measured in an infinite medium; however, the photon intensity measured at a site on the applicator interface but closer to the source should resemble more of that measured in a semi-infinite medium. This inconsistency implies the inaccuracy of modeling the photon diffusion for a ring applicator based on either infinite or semi-infinite geometry. Accurate

treatment of the circular concave boundary as for a ring-applicator requires analysis in cylindrical coordinates. The model of photon diffusion in a medium bounded externally by a circular cylindrical applicator has been investigated previously in several elegant studies. Arridge et al. (Arridge et al., 1992) used a boundary condition of zero-fluence at the applicator interface to derive the time-domain and frequency-domain solutions for finite and infinite cylinders using Bessel functions and modified Bessel functions. The more accurate extrapolated boundary condition (Haskell et al., 1994; Contini et al., 1997) was applied to similar concave applicator geometry, by Pogue et al. (Pogue et al., 1994) for finite cylinder and Sassaroli et al. (Sassaroli et al., 2001) for infinite cylinder, to express the time-domain solutions by use of Bessel functions. These studies provided important insight to photon diffusion in a medium bounded by a concave applicator, which mostly applies to diffuse optical imaging of breast. Sassaroli et al. (Sassaroli et al., 2001) also studied the effect of a concave boundary with diameters 30mm to 50mm, in comparison to the semi-infinite plan boundary in the perspective of inverse problem. The time-domain results for a concave applicator have been applied to frequency-domain by Fourier transformation as in (Pogue et al., 1994), and can be extended to steady-state by temporal integration.

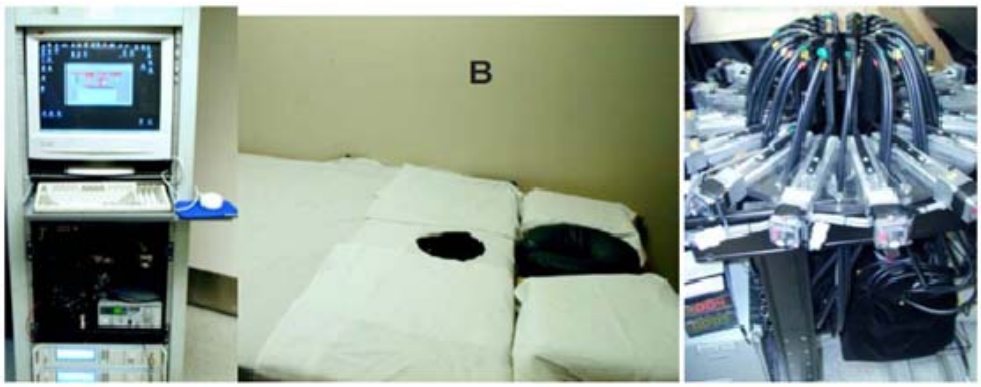

Fig. 3 Breast imaging system developed at Dartmouth

Recently work by our group (Piao et al., 2006; Piao et al., 2009) as well as others (Li et al., 2007; Boutet et al., 2009) has investigated different aspects of applying diffuse optical tomography to imaging internal organs such as prostate using an endo-rectal probe as illustrated in Fig. 4. This type of imaging geometry requires a convex-shaped applicator to be used. The analytic model of photon diffusion in compliance to such convex geometry, simplified by a diffusive medium bounded internally by a cylindrical applicator, has not been derived previously. Accurate modeling of photon propagation in a specific convex geometry could certainly be rendered by Monte Carlo method (Sassaroli et al., 2001). The finite-element solution of photon diffusion (Li et al., 2007; Piao et al., 2009) in such convex geometry may also prove sufficiently accurate in the diffusion regime. Given the availability of numerical means, finding the analytic model of photon diffusion is still imperative and important as it ultimately is beneficial to calibrating the measurement data and improving the reconstruction accuracy. What and how accurate such diffusion-based model could predict, at smaller scale of the convex-geometry for applications such as endo-rectal imaging, is especially interesting.

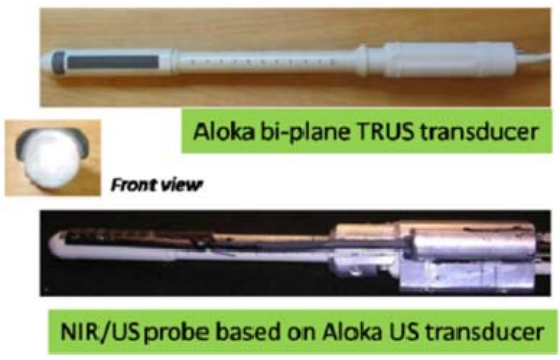

Fig. 4 Trans-rectal probe developed at Oklahoma State University

1.4 Hybrid NIR-US trans-rectal imaging at Oklahoma State University

In 2008, the integrated sagittal-imaging trans-rectal NIR/US applicator was developed, which consists of a custom-built NIR probe and a commercial bi-plane TRUS transducer, as shown in Fig. 5 (Jiang et al., 2008). The bi-plane TRUS probe is equipped with a proximal 7.5MHz sagittal-imaging transducer and a distal 5MHz transverse-imaging transducer. The sagittal TRUS transducer occupies a 60mm×10mm window. The diameters of the sagittal and transverse imaging sections of the TRUS probe are 18mm and 20mm, respectively. Adapting to the un-even TRUS cross-section, the NIR applicator is fabricated to a cap-shape and attached to the TRUS probe (Fig. 5 (a)-(e)). The NIR array substrate was machined from a black polycarbonate material to minimize the surface reflection. This substrate was then connected to an aluminum bracket and securely fastened to the TRUS handle using a bottom clamp. The rectangular TRUS handle (Fig. 5 (f)-(g)) ensured aligning the NIR applicator to the TRUS transducer. A slot of 60mm×10mm was opened up in the NIR applicator to expose the sagittal TRUS transducer.

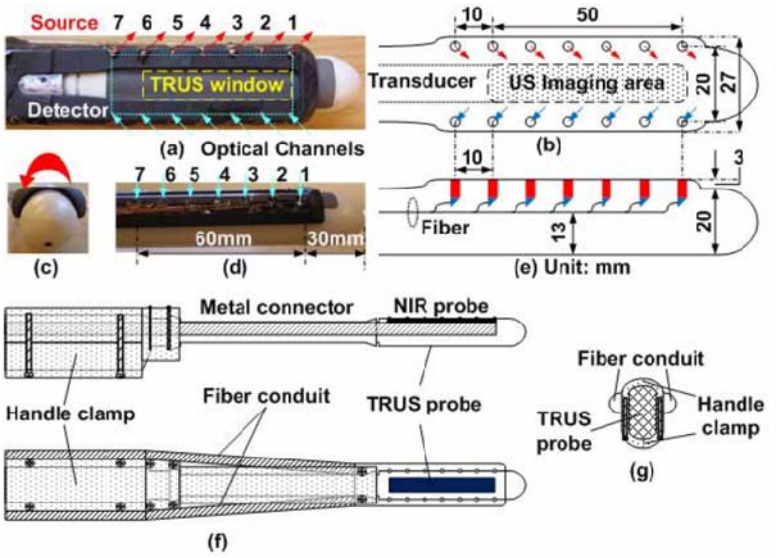

Fig. 5 The combined trans-rectal NIR/US probe: (a) top-view; (b) top-view dimension; (c) front-view; (d) side-view; (e) side-view dimension; (f) side and top views of the NIR/US alignment method; (g) rear-view of the NIR/US alignment method.

The combined trans-rectal NIR/US imager is schematically illustrated in Fig. 6(a) and the photograph is given in Fig. 6(b). The US scanner is an ALOKA SSD-900V portable machine. The US images are transferred to the main computer of the combined imager by a PCI image acquisition card (National Instruments PCI-1405). The NIR imager uses a custom-designed super-luminescent diode (SLD) (Superlumdiodes Inc.) that is pigtailed to a multi-mode fiber and delivers 100mW of 840nm NIR light with 14.2nm FWHM bandwidth. The SLD output beam is dispersed by a 1200 grooves/mm grating and collimated unto linearly aligned 7 fibers connecting to the source channels on NIR applicator. NIR light with slightly different wavelengths are coupled to the 7 fibers to form a spread-spectral-encoding of the source channels (Piao et al., 2006). The remitted lights collected by the 7 detection channels are coupled to a spectrometer

(Acton Research). The signal corresponding to the individual source channels are discriminated horizontally by the spectrometer. The signals corresponding to the individual detector channels are differentiated vertically based on the position of the detection channels on the spectrometer entrance slit. A 16-bit intensified CCD camera (Princeton Instruments) acquires a complete set of NIR imaging data. The NIR system resides on a custom-built cart that also houses the US scanner.

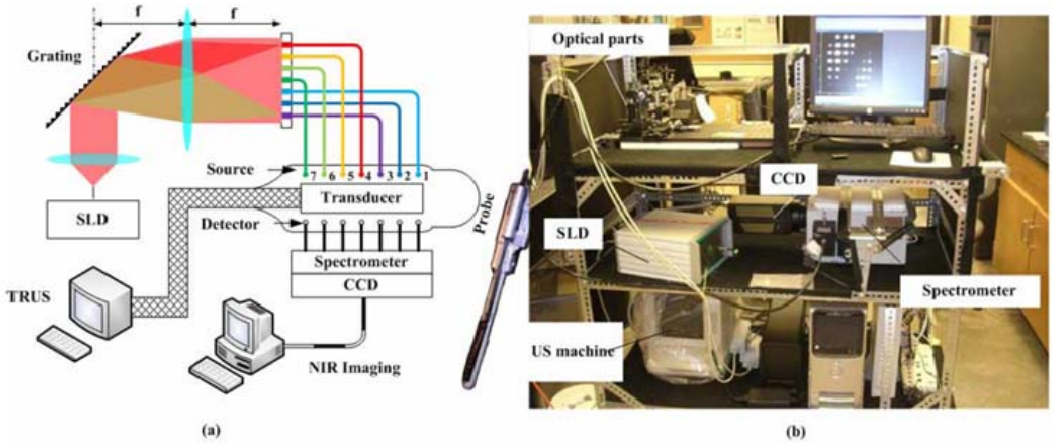

Fig. 6 The combined trans-rectal NIR/US system: (a) System diagram; (b) Photo of the system on a custom designed three-layer cart.

Figure 7 presents the *in-vivo* results of the canine prostate imaging (Jiang et al., 2009). The trans-rectal NIR absorption and US images were acquired at the middle of the right lobe, the middle line of the prostate, and the middle of the left lobe, which were obtained before the TVT injection, 14 days post-injection, and 35 days post-injection. The image dimensions are 60*30mm^2 (cranial-caudal*dorsal-ventral). On the day-35 US images of the right lobe and middle line, the hypoechoic region "L1" indicated an intra-prostatic mass; the large hypoechoic region "L2" indicated a mass ventral and caudal to the prostate that could have a connection with L1; the needle track (NT) on the right lobe denoted the needle trajectory for introducing the TVT cells with longitudinal hypoechoic regions, including L3, seen along the NT. On the day-35 NIR image

of the right lobe, the hyper-absorptive regions corresponded longitudinally to L1, L2, and L3. The growth of the tumor was indicated earlier by the NIR absorption images than by the TRUS as indicated by the day-14 images, and combining the information of NIR and TRUS led to earlier and more accurate findings of tumor growth than did TRUS alone.

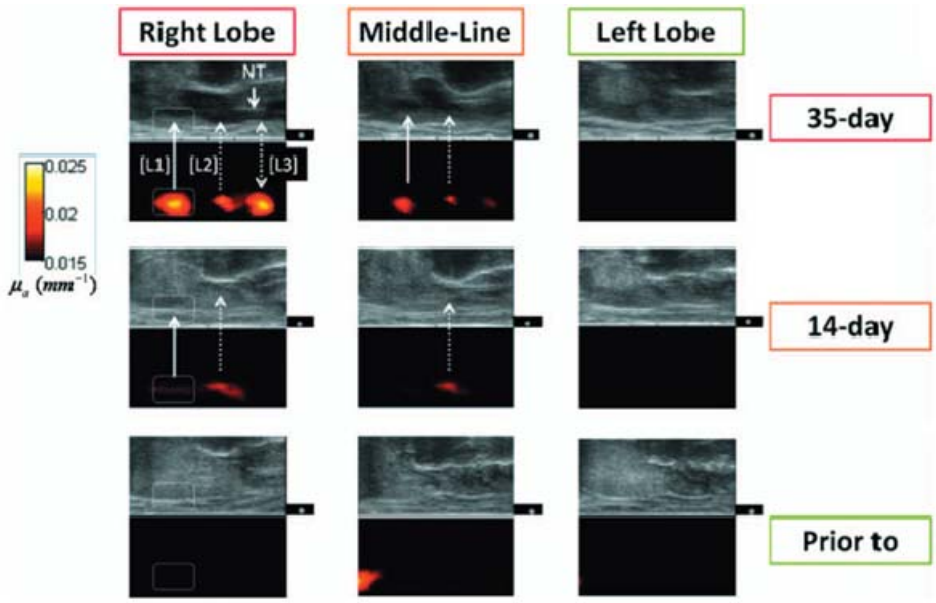

Fig. 7 *In vivo* trans-rectal NIR/US of TVT development in canine pelvic canal. The images were taken before the TVT injection, 14 days after the TVT injection when the US and rectal examination showed no evidence of tumor growth, and 35 days after the TVT injection when the tumor growth was evident on both US and rectal examination.

1.5 Overview

In this thesis, Chapter II and Chapter III devote to the development of the steady-state analytic model of trans-luminal photon diffusion. A new approach which explicitly depicts the decay of

photon fluence was proposed and validated. Chapter IV discusses a set of unique spiral paths on a cylindrical interface along which the decay of photon remission can be modeled as that along a straight line on a semi-infinite interface. Chapter V extends the mothodology employed in Chapter II for steady-state study to the frequency-domain analysis of the photon diffusion in trans-luminal geometries, and futher studies the unique spiral paths in frequency-domain.

CHAPTER II

TRANS-LUMINAL PHOTON DIFFUSION: STEADY-STATE THEORY

2.1 Analytic approach and geometries examined (Zhang et al., 2010)

2.1.1 Steady-state photon diffusion in an infinite medium---solution in cylindrical-coordinates

The steady-state photon diffusion equation is expressed by (Fantini et al., 1994; Arridge et al., 1992; Haskell et al., 1994; Contini et al., 1997) :

$$\nabla^2\Psi(\vec{r})-\frac{\mu_a}{D}\Psi(\vec{r})=-\frac{S(\vec{r})}{D} \tag{2.1.1}$$

where Ψ is the photon fluence rate at position $\vec{r}$, μ_a is the absorption coefficient, $D=\left[3(\mu_a+\mu_s')\right]^{-1}$ is the diffusion coefficient with μ_s' being the reduced scattering coefficient, and S is the source. Considering a source at $\vec{r}\,'$ of (ρ',φ',z') and a detector at $\vec{r}$ of (ρ,φ,z) in cylindrical-coordinates, the equation for the Green's function of Eq. (2.1.1) is

$$\nabla^2 G(\vec{r},\vec{r}\,')-k_0^2 G(\vec{r},\vec{r}\,')=-\delta(\vec{r}-\vec{r}\,') \tag{2.1.2}$$

where $k_0=\sqrt{\mu_a/D}$ is the effective attenuation coefficient. The Dirac delta function in Eq. (2.1.2) is

$$\delta(\vec{r}-\vec{r}\,')=\frac{1}{\rho}\delta(\rho-\rho')\delta(\varphi-\varphi')\delta(z-z') \tag{2.1.3}$$

where the delta functions for φ and z can be written in terms of inverse Fourier series and inverse Fourier transform, respectively, by

$$\delta(\varphi-\varphi')=\frac{1}{2\pi}\sum_{m=-\infty}^{\infty}e^{im(\varphi-\varphi')} \tag{2.1.4}$$

and

$$\delta(z-z') = \frac{1}{2\pi}\int_0^\infty dk\, e^{ik(z-z')} = \frac{1}{\pi}\int_0^\infty dk \cos\left[k(z-z')\right] \tag{2.1.5}$$

Substituting Eqs. (2.1.3) - (2.1.5) into Eq. (2.1.2) and expanding ∇^2 in Eq. (2.1.2) in cylindrical-coordinates lead to

$$\frac{1}{\rho}\frac{\partial}{\partial\rho}\left(\rho\frac{\partial G(\vec{r},\vec{r}')}{\partial\rho}\right) + \frac{1}{\rho^2}\frac{\partial^2 G(\vec{r},\vec{r}')}{\partial\varphi^2} + \frac{\partial^2 G(\vec{r},\vec{r}')}{\partial z^2} - k_0^2 G(\vec{r},\vec{r}')$$

$$= -\frac{1}{2\pi^2\rho}\delta(\rho-\rho')\sum_{m=-\infty}^{\infty}\int_0^\infty dk\, e^{im(\varphi-\varphi')}\cos\left[k(z-z')\right] \tag{2.1.6}$$

The Green's function can be expanded to a form similar to the right-hand-side of Eq. (2.1.6) as

$$G(\vec{r},\vec{r}') = \frac{1}{2\pi^2}\sum_{m=-\infty}^{\infty}\int_0^\infty dk \cdot g_m(k,\rho,\rho')\cdot e^{im(\varphi-\varphi')}\cos\left[k(z-z')\right] \tag{2.1.7}$$

where $g_m(k,\rho,\rho')$ is the radial Green's function to be solved. Substituting Eq. (2.1.7) into Eq. (2.1.6) leads to

$$\frac{1}{\rho}\frac{\partial}{\partial\rho}\left(\rho\frac{\partial g_m(k,\rho,\rho')}{\partial\rho}\right) - \left(k^2 + k_0^2 + \frac{m^2}{\rho^2}\right)g_m(k,\rho,\rho') = -\frac{1}{\rho}\delta(\rho-\rho')$$

(2.1.8)

We define

$$k_{eff}^2 = k^2 + k_0^2 \qquad \text{or} \qquad k_{eff} = \sqrt{k^2 + k_0^2} \tag{2.1.9}$$

Then Eq. (2.1.8) becomes

$$\frac{1}{\rho}\frac{\partial}{\partial\rho}\left(\rho\frac{\partial g_m(k,\rho,\rho')}{\partial\rho}\right) - \left(k_{eff}^2 + \frac{m^2}{\rho^2}\right)g_m(k,\rho,\rho') = -\frac{1}{\rho}\delta(\rho-\rho') \tag{2.1.10}$$

Solutions to the Helmholtz equation Eq. (2.1.10) can be derived by following Jackson's approach of solving Poisson's equation (Jackson, 1998) and using the asymptotic approximations of modified Bessel functions (Arfken et al., 2005). The solution details are given in the Appendix A. With the solution for $g_m(k,\rho,\rho')$, we have

$$G(\vec{r},\vec{r}') = \frac{1}{2\pi^2}\int_0^\infty dk \cdot \left\{\sum_{m=0}^{\infty} \varepsilon_m I_m(k_{eff}\rho_<) K_m(k_{eff}\rho_>)\cos[m(\varphi-\varphi')]\right\} \cdot \cos[k(z-z')] \tag{2.1.11}$$

where $\rho_<$ and $\rho_>$ indicate the smaller and larger radial coordinates of the source and the detector, and

$$\varepsilon_m = \begin{cases} 2, & m \neq 0 \\ 1, & m = 0 \end{cases} \tag{2.1.12}$$

Convolving the Green's function with the source term in Eq. (2.1.1), and assuming a point source, renders the cylindrical-coordinates solution to the steady-state photon diffusion in an infinite homogeneous medium as:

$$\Psi(\vec{r},\vec{r}') = \frac{S}{2\pi^2 D}\int_0^\infty dk \cdot \left\{\sum_{m=0}^{\infty} \varepsilon_m I_m(k_{eff}\rho_<) K_m(k_{eff}\rho_>)\cos[m(\varphi-\varphi')]\right\} \cdot \cos[k(z-z')] \tag{2.1.13}$$

2.1.2 Steady-state photon diffusion in an infinite homogeneous medium--solution in spherical-coordinates

The solution to Eq. (2.1.1) in spherical-coordinates is well-known as

$$\Psi(\vec{r},\vec{r}') = \frac{S}{4\pi D|\vec{r}-\vec{r}'|} e^{-k_0|\vec{r}-\vec{r}'|} \tag{2.1.14}$$

If the distance between a source and a detector is denoted by d, Eq. (2.1.14) is readily converted to

$$\ln(\Psi \cdot d) = -k_0 d + \ln\left(\frac{S}{4\pi D}\right) \tag{2.1.15}$$

Equation (2.1.15) indicates a linear relationship between the natural logarithm of the product of the fluence rate and the source-detector distance with respect to the source-detector distance, a characteristics useful for calibration with a homogeneous medium when an isotropic point source

can be assumed. For the same homogeneous medium and source-detector geometry, the solutions given by Eq. (2.1.14) and Eq. (2.1.13) shall be identical to each other, which will be numerically validated in Section 2.4 of this chapter.

2.1.3 Steady-state photon diffusion in a semi-infinite medium---solutions in spherical-coordinates

The effect of an applicator boundary on photon diffusion has been rigorously modeled by the index-miss-matched Robin-type boundary condition of

$$\Psi - 2AD\nabla\Psi \bullet \vec{n} = 0 \tag{2.1.16}$$

where $A = (1 + R_{eff})/(1 - R_{eff})$ and the R_{eff} is the effective reflection coefficient (Srinivasan et al., 2007) representing the percentage of the outgoing radiance integrated over all directions pointing toward the ambient medium that is converted to incoming radiance integrated over all directions pointing toward the scattering medium (Wang et al., 2007). The Robin-type boundary condition Eq. (2.1.16), which is evaluated on the physical boundary, can be surrogated by an almost equally accurate but more convenient approach by use of Type-I boundary condition that is being evaluated on an "imaginary" boundary. The "imaginary" boundary, referred to as the "extrapolated" boundary (Haskell et al., 1994; Contini et al., 1997), is located $2AD$ from the physical boundary and away from the medium. It is with respect to this extrapolated boundary that the negative "image" (Fine et al., 1998) of the source is introduced to set zero the fluence rate on this boundary.

We follow the notations introduced by Fantini et al. (Fantini et al., 1994) for the semi-infinite geometry having a directional source and an isotropic detector located on a planar boundary, as illustrated in Fig. 8(a). The directional source is modeled as an isotropic source placed one reduced scattering distance into the medium. Then, based on the extrapolated boundary approach, the steady-state photon fluence rate reaching the detector located on the

physical boundary is determined by the equivalent "real" isotropic source and its image source with respect to the extrapolated boundary, in spherical-coordinates, as:

$$\Psi = \Psi_{real} - \Psi_{imag} = \frac{S}{4\pi D l_{real}} e^{-k_0 l_{real}} - \frac{S}{4\pi D l_{imag}} e^{-k_0 l_{imag}} \tag{2.1.17}$$

where

$$l_{real} = \sqrt{d^2 + R_a^2}\,, \qquad R_a = 1/\mu_s' \tag{2.1.18}$$

$$l_{imag} = \sqrt{d^2 + (2R_b + R_a)^2}\,, \qquad R_b = 2AD \tag{2.1.19}$$

The d in Eq. (2.1.18) and Eq. (2.1.19) is the distance between the physical directional source and the detector, both located at the physical boundary, as in Eq. (2.1.15). For $d >> R_a, R_b$, Eq. (2.1.17) converts (Ntziachristos et al., 2000) to

$$\ln\left(\Psi \cdot d^2\right) = -k_0 \cdot d + \ln\left(\frac{S}{2\pi D} \cdot k_0 R_b (R_a + R_b)\right) \tag{2.1.20}$$

which is the model-basis for calibrating in a semi-infinite homogeneous medium.

2.1.4 The cylindrical interface geometries being investigated in this study

In this work, the "concave" geometry is defined as having the diffusive medium ***enclosed*** by an infinitely long cylindrical applicator, and the "convex" geometry as having the diffusive medium ***enclosing*** an infinitely long cylindrical applicator. The physical directional source is always modeled as an isotropic source placed one reduced scattering distance into the medium, as shown

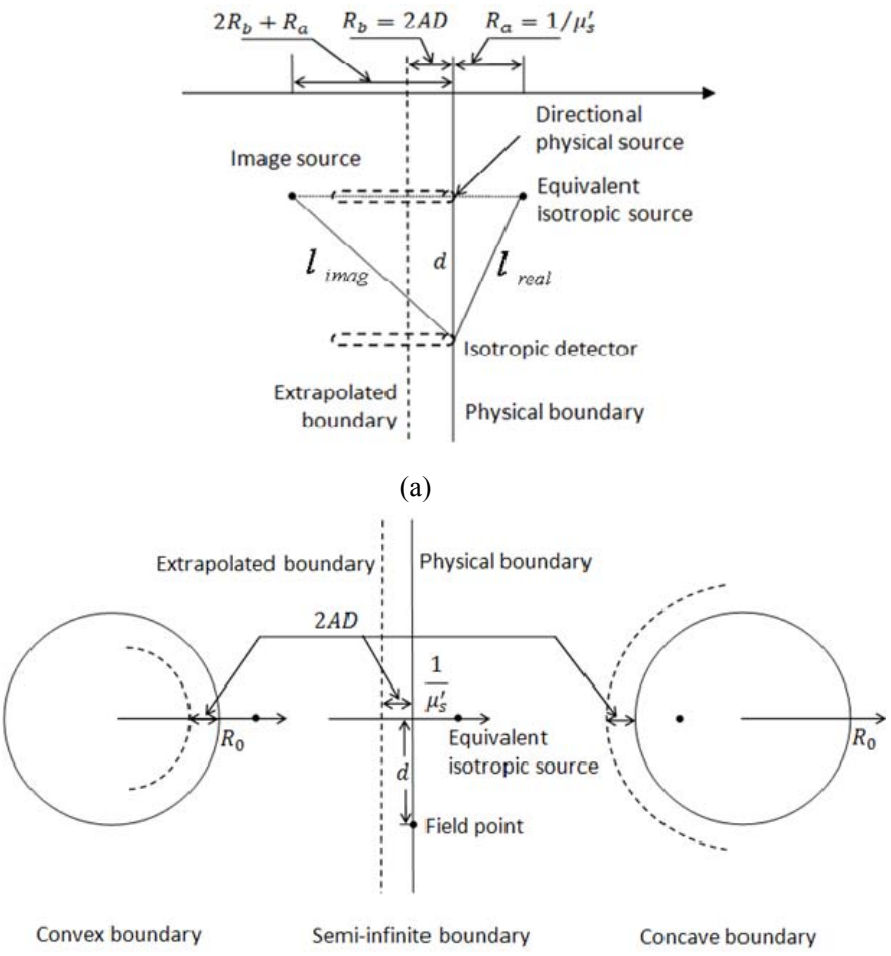

Fig. 8 (a) The semi-infinite geometry. The diffuse medium is right to the physical boundary, and the light is incident from the left. (b) The two cylindrical geometries in comparison to the semi-infinite geometry. The convex boundary represents that of a cylindrical applicator enclosed by the diffuse medium (e.g., imaging the prostate by a trans-rectal probe), and the concave boundary represents that of a cylindrical applicator enclosing the diffuse medium (e.g. imaging the breast by a ring probe).

in Fig. 8(b). Usually, the extrapolated boundary condition is applicable when a diffusive medium bonds with a non-scattering region----a valid representation of either external-imaging or internal-imaging optical applicator. Since the distance of the extrapolated boundary to the physical

boundary, $R_b = 2AD$ as in semi-infinite geometry, is derived from the general expression of the boundary condition in Eq. (2.1.16), this distance shall be considered as geometry-independent, therefore in the concave or convex geometry the extrapolated boundary shall also locate at a radial distance of $R_b = 2AD$ from the physical boundary and away from the diffusive medium. Apparently as the radius reaches infinity both concave and convex geometries approach the semi-infinite geometry. This feature serves as both the qualitative and quantitative measures of the analytic solutions derived for the concave and convex probe geometries.

2.2 Steady-state photon diffusion associated with concave or convex infinite cylindrical applicator

This session derives the cylindrical-coordinates solutions to steady-state photon diffusion in the concave and convex cylinder geometries. The same analytic principles apply to both the concave and convex geometries; however, the detailed analytic derivations of the two geometries are separately listed for completeness and for facilitating qualitative comparison between them.

2.2.1 External "concave" boundary ---Analytic solution

The concave geometry for a medium bounded externally by an infinitely long circular cylindrical applicator with radius R_0 is illustrated in Fig. 9. The physical source is located at (R_0, φ', z') and the detector is located at (R_0, φ, z), both on the physical boundary.

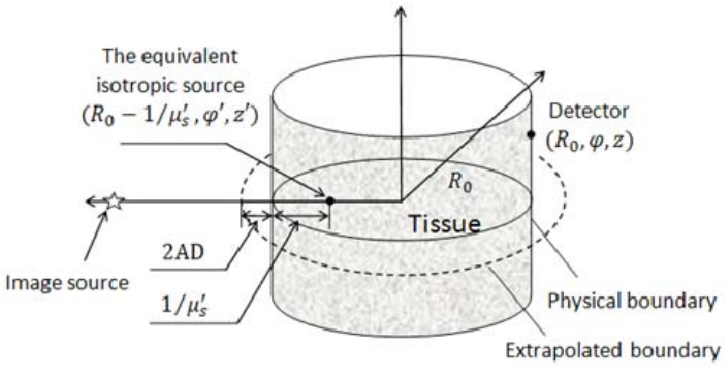

Fig. 9 Details of the concave geometry indicating the equivalent isotropic source and the extrapolated boundary. The image source of the isotropic source with respect to the extrapolated boundary shall be located along the radial direction of the isotropic source due to symmetry.

A. Photon diffusion under the extrapolated boundary condition

As shown in Fig. 9, the equivalent "real" isotropic source must locate at $(R_0 - R_a, \varphi', z')$ based on the symmetry of the geometry, and the extrapolated boundary shall locate at a radial distance of $R_b = 2AD$ outside the physical boundary. Based on the symmetry of the geometry, the image source of the "real" isotropic source with respect to the extrapolated boundary must also locate along the radial direction of the "real" isotropic or the physical source. This image source and the "real" isotropic source collectively set zero the photon fluence rate on the extrapolated boundary.

Based on Eq. (2.1.13), the photon fluence rate associated with the "real" isotropic source and evaluating on the extrapolated boundary, for which the source locates at $\rho_{r<} = R_0 - R_a$ and the detector locates at $\rho_{r>} = R_0 + R_b$, is

$$\Psi_{real}\Big|_{extr} = \frac{1}{2\pi^2 D}\int_0^\infty dk \cdot \cos\left[k(z-z')\right] \cdot\left\{\sum_{m=0}^{\infty} \varepsilon_m \, S\, I_m\left[k_{eff}\left(R_0 - R_a\right)\right] K_m\left[k_{eff}\left(R_0 + R_b\right)\right]\cos\left[m(\varphi-\varphi')\right]\right\}$$

(2.2.1)

where the notation "$_{left}\Big|_{right}$" indicates evaluating the "left" as a source on the "right" as a boundary. Similarly, the photon fluence rate associated with the image source and evaluating on the extrapolated boundary, for with the source locates at an unknown or yet-to-decide $\rho_{i>}$ but the detector locates at $\rho_{i<} = R_0 + R_b$, is

$$\Psi_{imag}\Big|_{extr} = \frac{1}{2\pi^2 D}\int_0^\infty dk \cdot\left\{\sum_{m=0}^{\infty} \varepsilon_m \, S_m^*\, I_m\left[k_{eff}\left(R_0 + R_b\right)\right] K_m\left[k_{eff}\,\rho_{i>}\right]\cos\left[m(\varphi-\varphi')\right]\right\}\cdot\cos\left[k(z-z')\right]$$

(2.2.2)

In Eq. (2.2.2), the S_m^* terms are also unknown or yet-to-decide, besides $\rho_{i>}$. Based on the essential concept of "image-source" (Fine et al., 1998; Cui et al., 2006), the two unknown terms S_m^* and $\rho_{i>}$ associated with the *m*-th order "image" source (the K_m component) can be expressed by a single unknown term of S_m associated with the same order "real" source (the I_m component) , that is

$$S_m^* K_m\left(k_{eff}\,\rho_{i>}\right) = S_m I_m\left[k_{eff}\,\rho_{r<}\right] = S_m I_m\left[k_{eff}\left(R_0 - R_a\right)\right] \tag{2.2.3}$$

Applying Eq. (2.2.3) to the extrapolated boundary condition of $\Psi_{real}\Big|_{extr} - \Psi_{imag}\Big|_{extr} = 0$, we have

$$S_m = S\frac{K_m\left[k_{eff}\left(R_0 + R_b\right)\right]}{I_m\left[k_{eff}\left(R_0 + R_b\right)\right]} \qquad m = 0, 1, 2, \cdots \tag{2.2.4}$$

Now for the "real" isotropic source but evaluating at the physical boundary, the source still locates at $\rho_{r<} = R_0 - R_a$ but the detector locates at $\rho_{r>} = R_0$. For the "image" source also evaluating at the physical boundary, the detector locates at $\rho_{i<} = R_0$, and the source terms are known through Eq. (2.2.3) and Eq. (2.2.4). Collectively the photon fluence rate sensed by a detector at the physical boundary becomes

$$\Psi = \Psi_{real}\big|_{phys} - \Psi_{imag}\big|_{phys}$$

$$= \frac{S}{2\pi^2 D}\int_0^\infty dk\Bigg\{\cos\left[k(z-z')\right]\cdot\sum_{m=0}^{\infty}\varepsilon_m I_m\left[k_{eff}\left(R_0-R_a\right)\right]K_m\left(k_{eff}R_0\right)$$

$$\cdot\left\langle 1-\frac{I_m\left(k_{eff}R_0\right)}{K_m\left(k_{eff}R_0\right)}\frac{K_m\left[k_{eff}\left(R_0+R_b\right)\right]}{I_m\left[k_{eff}\left(R_0+R_b\right)\right]}\right\rangle\cos\left[m(\varphi-\varphi')\right]\Bigg\} \qquad (2.2.5)$$

B. *The concave geometry with a large cylinder diameter----approaching the semi-infinite geometry*

As shown in Fig. 10, if a plane tangential to the cylinder at the physical source position is considered as an imaginary semi-infinite planar boundary, then the "real" isotropic source in this semi-infinite geometry still locates at $(R_0 - R_a, \varphi', z')$, but the image source of the "real" isotropic source with respect to this semi-infinite boundary will be at $(R_0 + R_a + 2R_b, \varphi', z')$.

According to Eq. (2.1.13) the photon fluence rate sensed by a detector on the cylinder boundary due to the image source of the "real" isotropic source associated with the semi-infinite boundary is

$$\Psi_{imag}^{semi}\big|_{phys} = -\frac{S}{2\pi^2 D}\int_0^\infty dk\cos\left[k(z-z')\right] \quad \cdot\sum_{m=0}^{\infty}\varepsilon_m I_m\left(k_{eff}R_0\right)K_m\left[k_{eff}\left(R_0+R_a+2R_b\right)\right]\cos\left[m(\varphi-\varphi')\right] \qquad (2.2.6)$$

The photon fluence rate sensed by a detector on the cylinder boundary due to the image source of the "real" isotropic source associated with the cylinder boundary, as seen in Eq. (2.2.5), can be rewritten to

$$\Psi_{imag}\big|_{phys} = -\frac{S}{2\pi^2 D}\int_0^\infty dk\cos\left[k(z-z')\right] \quad \cdot\sum_{m=0}^{\infty}\varepsilon_m I_m\left(k_{eff}R_0\right)K_m\left[k_{eff}\left(R_0+R_a+2R_b\right)\right]\cdot\eta_m\cos\left[m(\varphi-\varphi')\right] \qquad (2.2.7)$$

where

$$\eta_m = \frac{I_m\left[k_{eff}\left(R_0 - R_a\right)\right]}{I_m\left[k_{eff}\left(R_0 + R_b\right)\right]} \frac{K_m\left[k_{eff}\left(R_0 + R_b\right)\right]}{K_m\left[k_{eff}\left(R_0 + R_a + 2R_b\right)\right]} \tag{2.2.8}$$

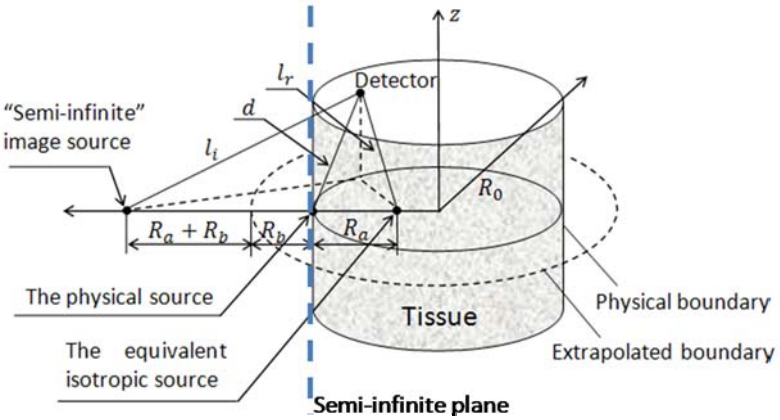

Fig. 10 The concave geometry and the "semi-infinite" image source which is the image source of the isotropic source with respect to a planar boundary tangential to the concave boundary at the location of the physical source.

If the cylinder diameter is sufficiently large, the modified Bessel functions in Eq. (2.2.8) can be simplified by their asymptotic expressions (Arfken et al., 2005), then Eq. (2.2.8) becomes

$$\eta_m = \sqrt{\frac{R_0 + R_a + 2R_b}{R_0 - R_a}} \tag{2.2.9}$$

Substituting Eq. (2.2.9) into Eq. (2.2.7) and comparing with Eq. (2.2.6) we have

$$\Psi_{imag}\Big|_{phys} = \Psi_{imag}^{semi}\Big|_{phys} \cdot \sqrt{\frac{R_0 + R_a + 2R_b}{R_0 - R_a}} \tag{2.2.10}$$

Hence, for the cylinder of sufficiently large diameter, Eq. (2.2.5) approximates to

$$\Psi = \Psi_{real}\Big|_{phys} - \Psi_{imag}\Big|_{phys} = \Psi_{real}\Big|_{phys} - \Psi_{imag}^{semi}\Big|_{phys} \cdot \sqrt{\frac{R_0 + R_a + 2R_b}{R_0 - R_a}} \tag{2.2.11}$$

As $R_0 \to \infty$, the $\Psi_{real}\big|_{phys}$ in Eq. (2.2.11) is essentially the same as the Ψ_{real} in Eq. (2.1.17), $\sqrt{(R_0 + R_a + 2R_b)/(R_0 - R_a)} \to 1$, and the $\Psi_{imag}^{semi}\big|_{phys}$ of Eq. (2.2.11) becomes the Ψ_{imag} in Eq. (2.1.17) because the detector located at (R_0, φ, z) reaches the imaginary semi-infinite boundary. This agrees with the physical aspect that an infinitely long concave cylinder boundary reaches a semi-infinite boundary as the radius of the cylinder becomes infinity. By using the spherical coordinate expression of the photon fluence rate given in Eq. (2.1.14), we can re-write Eq. (2.2.11) as

$$\Psi = \frac{S}{4\pi D}\frac{e^{-k_0 l_r}}{l_r} - \frac{S}{4\pi D}\frac{e^{-k_0 l_i}}{l_i}\sqrt{\frac{R_0 + R_a + 2R_b}{R_0 - R_a}} \tag{2.2.12}$$

2.2.2 Internal "convex" boundary---Analytic solution

The convex geometry for a medium bounded internally by an infinitely long circular cylindrical applicator with radius R_0 is illustrated in Fig. 11. The physical source is located at (R_0, φ', z') and the detector is located at (R_0, φ, z), both on the physical boundary.

A. <u>Photon diffusion under the extrapolated boundary condition</u>

As shown in Fig. 11, the equivalent "real" isotropic source must locate at $(R_0 + R_a, \varphi', z')$ based on the symmetry of the geometry, and the extrapolated boundary shall locate at a radial distance of $R_b = 2AD$ inside the physical boundary. Based on the symmetry of the geometry, the image source of the "real" isotropic source with respect to the extrapolated boundary must also locate along the radial direction of

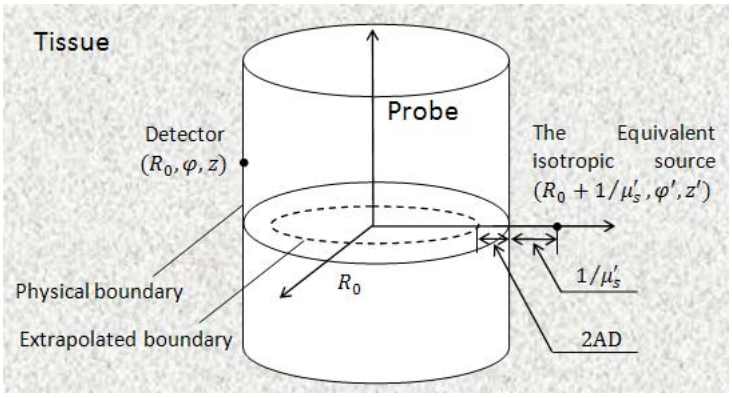

Fig. 11 Details of the convex geometry indicating the equivalent isotropic source and the extrapolated boundary.

the "real" isotropic or the physical source. This image source and the "real" isotropic source collectively set zero the photon fluence rate on the extrapolated boundary.

Based on Eq. (2.1.13), the photon fluence rate associated with the "real" isotropic source and evaluating on the extrapolated boundary, for which the source locates at $\rho_{r<} = R_0 - R_b$ and the detector locates at $\rho_{r>} = R_0 + R_a$, is

$$\Psi_{real}\Big|_{extr} = \frac{1}{2\pi^2 D}\int_0^\infty dk \cdot \cos\left[k(z-z')\right] \cdot \left\{\sum_{m=0}^{\infty} \varepsilon_m S\, I_m\left[k_{eff}(R_0 - R_b)\right] K_m\left[k_{eff}(R_0 + R_a)\right] \cos\left[m(\varphi - \varphi')\right]\right\}$$

(2.2.13)

where it uses the same notation "$_{left}\Big|_{right}$" as in Eq. (2.2.1). Similarly, the photon fluence rate associated with the image source and evaluating on the extrapolated boundary, for which the source locates at an unknown or yet-to-decide $\rho_{i<}$ but the detector locates at $\rho_{i>} = R_0 - R_b$, is

$$\Psi_{imag}\Big|_{extr} = \frac{1}{2\pi^2 D}\int_0^\infty dk \cdot \left\{\sum_{m=0}^{\infty} \varepsilon_m S_m^* I_m\left[k_{eff}\rho_{i<}\right] K_m\left[k_{eff}(R_0 - R_b)\right] \cos\left[m(\varphi - \varphi')\right]\right\} \cdot \cos\left[k(z-z')\right]$$

(2.2.14)

In Eq. (2.2.14), the S_m^* terms are also unknown or yet-to-decide, besides $\rho_{i<}$. Following the approach (Fine et al., 1998; Cui et al., 2006) as in Eq. (2.2.3), we have

$$S_m^* I_m\left(k_{eff}\,\rho_{i<}\right) = S_m K_m\left[k_{eff}\,\rho_{r>}\right] = S_m K_m\left[k_{eff}\left(R_0 + R_a\right)\right] \tag{2.2.15}$$

that expresses the two unknown terms S_m^* and $\rho_{i<}$ associated with the *m*-th order "image" source (the I_m component) by a single unknown term of S_m associated with the same order "real" source (the K_m component). Applying Eq. (2.2.15) to the extrapolated boundary condition of $\Psi_{real}\big|_{extr} - \Psi_{imag}\big|_{extr} = 0$ gives

$$S_m = S\,\frac{I_m\left[k_{eff}\left(R_0 - R_b\right)\right]}{K_m\left[k_{eff}\left(R_0 - R_b\right)\right]} \qquad m = 0, 1, 2, \cdots \tag{2.2.16}$$

Now for the "real" isotropic source but evaluating at the physical boundary, the source still locates at $\rho_{r>} = R_0 + R_a$ but the detector locates at $\rho_{r<} = R_0$. For the "image" source also evaluating at the physical boundary, the detector locates at $\rho_{i>} = R_0$, and the source terms are known through Eq. (2.2.15) and Eq. (2.2.16). Collectively the photon fluence rate sensed by a detector at the physical boundary becomes

$$\Psi = \Psi_{real}\big|_{phys} - \Psi_{imag}\big|_{phys} = \frac{S}{2\pi^2 D}\int_0^\infty dk \left\{ \cos\left[k\left(z - z'\right)\right] \cdot \sum_{m=0}^{\infty} \varepsilon_m I_m\left(k_{eff} R_0\right) K_m\left[k_{eff}\left(R_0 + R_a\right)\right] \right.$$
$$\left. \cdot \left\langle 1 - \frac{K_m\left(k_{eff} R_0\right)}{I_m\left(k_{eff} R_0\right)} \frac{I_m\left[k_{eff}\left(R_0 - R_b\right)\right]}{K_m\left[k_{eff}\left(R_0 - R_b\right)\right]} \right\rangle \cos\left[m\left(\varphi - \varphi'\right)\right] \right\} \tag{2.2.17}$$

B. *The convex geometry with a large cylinder diameter----approaching the semi-infinite geometry*

As shown in Fig.12, if a plane tangential to the cylinder at the physical source position is considered as a imaginary semi-infinite planar boundary, then the "real" isotropic source in this

semi-infinite geometry still locates at $(R_0 + R_a, \varphi', z')$, but the "image" source of the "real" isotropic source with respect to this semi-infinite boundary will be at $(R_0 - R_a - 2R_b, \varphi', z')$.

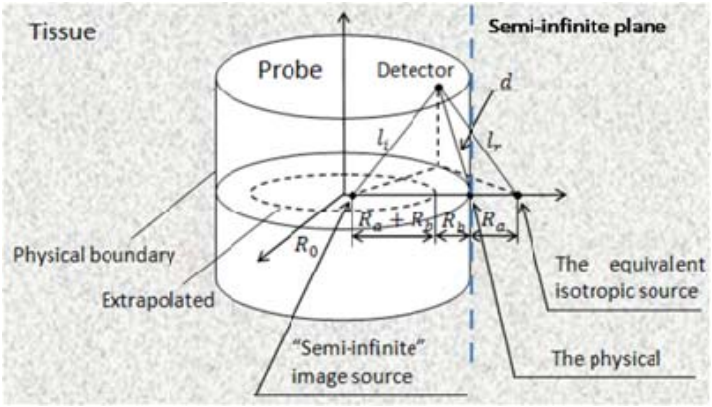

Fig. 12 The convex geometry and the "semi-infinite" image source which is the image source of the isotropic source with respect to a planar boundary tangential to the concave boundary at the location of the physical source.

According to Eq. (2.1.13) the photon fluence rate sensed by a detector on the cylinder boundary due to the image source of the "real" isotropic source associated with the semi-infinite boundary is

$$\Psi_{imag}^{semi}\Big|_{phys} = -\frac{S}{2\pi^2 D}\int_0^\infty dk \cos\left[k(z-z')\right] \cdot \sum_{m=0}^{\infty} \varepsilon_m I_m\left[k_{eff}\left(R_0 - R_a - 2R_b\right)\right] K_m\left(k_{eff} R_0\right) \cos\left[m(\varphi - \varphi')\right] \tag{2.2.18}$$

The photon fluence rate sensed by a detector on the cylinder boundary due to the image source of the "real" isotropic source associated with the cylinder boundary, as seen in Eq. (2.2.17), can be rewritten to

$$\Psi_{imag}\Big|_{phys} = -\frac{S}{2\pi^2 D}\int_0^{\infty} dk \cos\left[k(z-z')\right]$$

$$\cdot \sum_{m=0}^{\infty} \varepsilon_m I_m\left[k_{eff}\left(R_0 - R_a - 2R_b\right)\right] K_m\left(k_{eff} R_0\right) \cdot \eta_m \cos\left[m(\varphi - \varphi')\right] \qquad (2.2.19)$$

where

$$\eta_m = \frac{I_m\left[k_{eff}\left(R_0 - R_b\right)\right]}{I_m\left[k_{eff}\left(R_0 - R_a - 2R_b\right)\right]} \frac{K_m\left[k_{eff}\left(R_0 + R_a\right)\right]}{K_m\left[k_{eff}\left(R_0 - R_b\right)\right]} \qquad (2.2.20)$$

If the cylinder diameter is sufficiently large, the modified Bessel functions in Eq. (2.2.20) can be simplified by their asymptotic expressions (Arfken et al., 2005), then Eq. (2.2.20) becomes

$$\eta_m = \sqrt{\frac{R_0 - R_a - 2R_b}{R_0 + R_a}} \qquad (2.2.21)$$

Substituting Eq. (2.2.21) into Eq. (2.2.19) and comparing with Eq. (2.2.18) we have

$$\Psi_{imag}\Big|_{phys} = \Psi_{imag}^{semi}\Big|_{phys} \cdot \sqrt{\frac{R_0 - R_a - 2R_b}{R_0 + R_a}} \qquad (2.2.22)$$

Hence, for the cylinder of sufficiently large diameter, Eq. (2.2.17) approximates to

$$\Psi = \Psi_{real}\Big|_{phys} - \Psi_{imag}\Big|_{phys} = \Psi_{real}\Big|_{phys} - \Psi_{imag}^{semi}\Big|_{phys} \cdot \sqrt{\frac{R_0 - R_a - 2R_b}{R_0 + R_a}} \qquad (2.2.23)$$

As $R_0 \to \infty$, the $\Psi_{real}\big|_{phys}$ of Eq. (2.2.23) is essentially the same as the Ψ_{real} in Eq. (2.1.17), $\sqrt{\left(R_0 - R_a - 2R_b\right)/\left(R_0 + R_a\right)} \to 1$, and the $\Psi_{imag}^{semi}\big|_{phys}$ of Eq. (2.2.23) becomes the Ψ_{imag} in Eq. (2.1.17) because the detector located at (R_0, φ, z) reaches the imaginary semi-infinite boundary. This agrees with the physical aspect that an infinitely long convex cylinder boundary reaches a semi-infinite boundary as the radius of the cylinder becomes infinity. By using the spherical coordinate expression of the photon fluence rate given in Eq. (2.1.14), we can re-write Eq. (2.2.23) as

$$\Psi = \frac{S}{4\pi D}\frac{e^{-k_0 l_r}}{l_r} - \frac{S}{4\pi D}\frac{e^{-k_0 l_i}}{l_i}\sqrt{\frac{R_0 - R_a - 2R_b}{R_0 + R_a}} \qquad (2.2.24)$$

2.2.3 Summary of the solutions in cylindrical-coordinates

In cylindrical-coordinates, the steady-state photon fluence rate in an infinite homogenous medium is:

$$\Psi = \frac{S}{2\pi^2 D}\int_0^\infty dk \cos\left[k\left(z-z'\right)\right]\cdot\sum_{m=0}^{\infty}\varepsilon_m I_m\left(k_{eff}\rho_<\right)K_m\left(k_{eff}\rho_>\right)\cos\left[m\left(\varphi-\varphi'\right)\right] \qquad (2.2.25)$$

The steady-state photon fluence rate in a concave geometry imposed by an infinitely long circular cylindrical applicator for interrogating the medium internal to the applicator (e.g. breast imaging) is:

$$\Psi = \frac{S}{2\pi^2 D}\int_0^\infty dk\left\{\cos\left[k\left(z-z'\right)\right]\cdot\sum_{m=0}^{\infty}\varepsilon_m I_m\left[k_{eff}\left(R_0-R_a\right)\right]K_m\left(k_{eff}R_0\right)\right.$$

$$\left.\cdot\left\langle 1-\frac{I_m\left(k_{eff}R_0\right)}{K_m\left(k_{eff}R_0\right)}\frac{K_m\left[k_{eff}\left(R_0+R_b\right)\right]}{I_m\left[k_{eff}\left(R_0+R_b\right)\right]}\right\rangle\cos\left[m\left(\varphi-\varphi'\right)\right]\right\} \qquad (2.2.26\text{conC})$$

The steady-state photon fluence rate in a convex geometry imposed by an infinitely long circular cylindrical applicator for interrogating the medium external to the applicator (e.g. prostate imaging) is:

$$\Psi = \frac{S}{2\pi^2 D}\int_0^\infty dk\left\{\cos\left[k\left(z-z'\right)\right]\cdot\sum_{m=0}^{\infty}\varepsilon_m I_m\left[k_{eff}R_0\right]K_m\left[k_{eff}\left(R_0+R_a\right)\right]\right.$$

$$\left.\cdot\left\langle 1-\frac{K_m\left(k_{eff}R_0\right)}{I_m\left(k_{eff}R_0\right)}\frac{I_m\left[k_{eff}\left(R_0-R_b\right)\right]}{K_m\left[k_{eff}\left(R_0-R_b\right)\right]}\right\rangle\cos\left[m\left(\varphi-\varphi'\right)\right]\right\} \qquad (2.2.26\text{conV})$$

If the concave or convex geometry has large radial dimension, the photon fluence rate expressed by Eq. (2.2.26conC) and Eq. (2.2.26conV) can be approximated to

$$\Psi = \frac{S}{4\pi D}\frac{e^{-k_0 l_r}}{l_r} - \frac{S}{4\pi D}\frac{e^{-k_0 l_i}}{l_i}\sqrt{\frac{R_0+R_a+2R_b}{R_0-R_a}} \qquad (2.2.27\text{conC})$$

$$\Psi = \frac{S}{4\pi D}\frac{e^{-k_0 l_r}}{l_r} - \frac{S}{4\pi D}\frac{e^{-k_0 l_i}}{l_i}\sqrt{\frac{R_0-R_a-2R_b}{R_0+R_a}} \qquad (2.2.27\text{conV})$$

where l_r is defined as the distance from the detector to the "real" isotropic source, and l_i as the distance from the detector to the image source of the "real" isotropic source associated with the semi-infinite geometry that is tangential to the concave or convex geometry on the physical source point.

2.3 Steady-state photon diffusion in the infinite geometry---numerical verification of the cylindrical-coordinates solution

This section validates the cylindrical-coordinates solution Eq. (2.1.13) of the steady-state photon diffusion in a homogenous infinite medium, since Eq. (2.1.13) sets the foundation of the analytic derivations thereafter. As evaluating entities like Eq. (2.1.13) involves half-sided integration and summation up to the infinity, the numerical approaches shall provide sufficient accuracy within the framework imposed by the precision of the computer and the algorithm arithmetic.

For an infinite medium it is practical to define a source point arbitrarily at $(0,0,0)$ and a field point at $(\rho,0,0)$. Then the spherical-coordinates solution Eq. (2.1.14) can be rewritten as

$$\Psi = \frac{S}{4\pi D d} e^{-k_0 d} \tag{2.3.1}$$

where d is the source-detector distance. The Eq. (2.3.1) can be implemented in terms of the linear relationship between $\ln(\Psi d)$ and d as indicated in Eq. (2.1.15). Similarly the cylindrical-coordinates solution Eq. (2.2.25) in the same homogeneous infinite medium becomes

$$\Psi(\rho,\varphi) = \frac{S}{2\pi^2 D}\int_0^\infty dk \sum_{m=0}^{\infty} \varepsilon_m I_m(0) K_m\left(k_{eff}\rho_>\right) \tag{2.3.2}$$

The adaptive Gauss-Kronrod quadrature in MATLAB (Mathworks Inc, Natick, MA) is used to calculate the integrations in Eq. (2.3.2) as well as all the integrations appearing later. To effectively implement the integration and the infinite-summation terms in Eq. (2.3.2), it is

necessary to evaluate the range for the integration or the summation to be executed. Based on the asymptotic expression of the modified Bessel functions for large argument (Arfken et al., 2005), we have that for sufficiently large *k*, hence large k_{eff} ,

$$I\left(k_{eff}\rho_{<}\right)K\left(k_{eff}\rho_{>}\right)=\frac{1}{2k_{eff}\sqrt{\rho_{<}\rho_{>}}}e^{-k_{eff}(\rho_{>}-\rho_{<})} \tag{2.3.3}$$

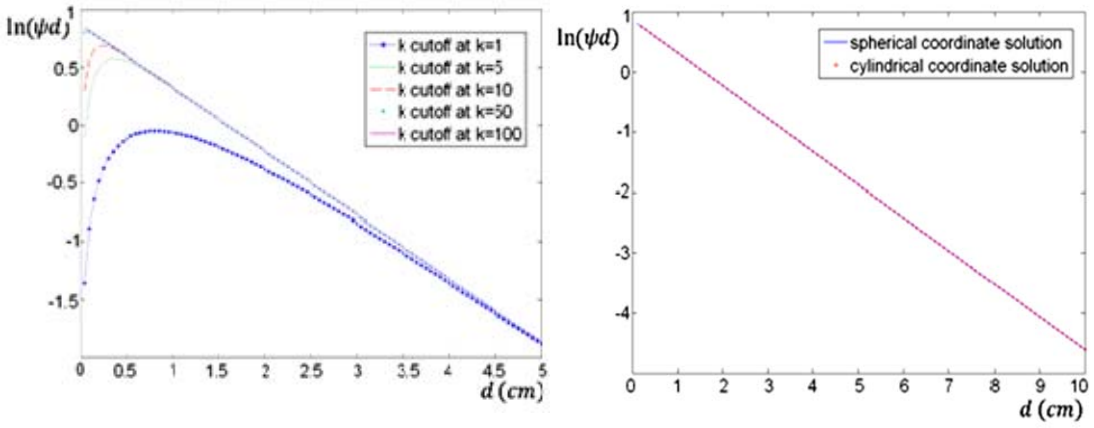

(a) (b)

Fig. 13 (a) Comparison of the contributions of the k terms when evaluating the cylindrical-coordinates solution to the steady-state photon diffusion in the homogenous infinite medium. (b) Comparison between the solutions, in spherical-coordinates and cylindrical-coordinates, to the steady-state photon diffusion in the homogenous infinite medium.

which asymptotically and quasi-exponentially reaches zero as *k* increases. Therefore for a given accuracy Eq. (2.3.2) can be numerically implemented with an upper-limit of *k,* because it also sets the upper limit of the integration. The contributions of higher *k* to the integration in Eq. (2.3.2) are evaluated in Fig. 13(a), for the first *m* term of $m=0$, using realistic optical and geometry

parameters including $\mu_a = 0.01cm^{-1}$, $\mu_s' = 10cm^{-1}$, $\varphi = 0$, and $d = 0.5 - 10cm$. The use of $\ln(\Psi d)$ versus d is necessary for evaluating Eq. (2.3.2) with respect to Eq. (2.3.1). The difference of setting k upper-limit at 50 or 100 is indistinguishable for source-detector distance greater than $1mm$, at the scale shown. The integration in Eq. (2.3.2) is therefore executed for $k = 50$ as the source-detector distance practically is much greater than $1mm$.

To evaluate the choice of m, we first check the following terms in Eq. (2.3.2), and denote it as Ω

$$\Omega = \sum_{m=0}^{\infty} \varepsilon_m I_m(0) K_m\left(k_{eff}\rho_>\right) \tag{2.3.4}$$

In Eq. (2.3.4), $I_m(0)$ will be nonzero only when $m = 0$. Hence, only the first m term need to be summated. Overall, Eq. (2.3.2) can be evaluated by integrating up to $k = 50$ and summing the first m terms.

Figure 13(b) evaluates Eq. (2.3.2) with respect to Eq. (2.3.1), for the parameters of $\mu_a = 0.01cm^{-1}$, $\mu_s' = 10cm^{-1}$, $\varphi = 0$, and $\rho = 0.5 - 10cm$ as in Fig. 13(a), and integrating the k up to 100 for $m = 0$. Figure 13(b) demonstrates that Eq. (2.3.2) is identical to Eq. (2.3.1) within the precision of the MATLAB arithmetic.

2.4 Steady-state photon diffusion in the "concave" and "convex" geometries-----numerical evaluation of the cylindrical-coordinates solutions

This section numerically evaluates the general solutions in Eq. (2.2.26) for the geometries having smaller cylinder radius and their approximations in Eq. (2.2.27) for the geometries having very large cylinder radius. These evaluations, for simplicity, are limited to two cases: (1) the source and detector locate at the same azimuth plane; (2) the source and detector locate longitudinally

with the same azimuthal angle. The results will indicate how the circular boundary affects the photon fluence rate with respect to a semi-infinite boundary, and justify qualitatively these analytic solutions and their approximations.

2.4.1 Specific geometry---source and detector located at the same azimuth plane

The geometries shown in Fig. 14 are chosen to study the effect of concave or convex boundary shape on photon diffusion for the source and detector located at the same azimuth plane. Then the "chord" distance d between the source and the detector is considered in a range from $0.5cm$ (assuring diffusion treatment) to $2R_0$, for optical properties set at $\mu_a = 0.01cm^{-1}$, $\mu_s' = 10\,cm^{-1}$, $A = 1$ and $S = 1$ (these parameters are used throughout the rest of the studies).

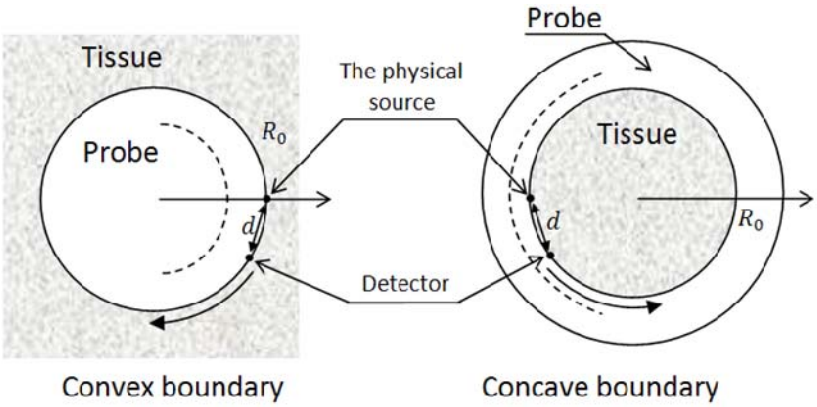

Fig. 14 The concave and convex geometries with the source and the detector located at the same azimuthal plane.

A. Numerical approaches

In this case, both the source and detector are on the same azimuthal plane, that is $z = z'$, therefore Eq. (2.2.26conC) and Eq. (2.2.26conV) can be rewritten as

$$\Psi = \frac{S}{2\pi^2 D}\int_0^\infty dk\left\{\sum_{m=0}^{\infty}\varepsilon_m I_m\left[k_{eff}\left(R_0 - R_a\right)\right]K_m\left(k_{eff}R_0\right)\right.$$
$$\left.\cdot\left\langle 1 - \frac{I_m\left(k_{eff}R_0\right)}{K_m\left(k_{eff}R_0\right)}\frac{K_m\left[k_{eff}\left(R_0 + R_b\right)\right]}{I_m\left[k_{eff}\left(R_0 + R_b\right)\right]}\right\rangle\cos\left[m\left(\varphi - \varphi'\right)\right]\right\} \quad (2.4.1\text{conC})$$

$$\Psi = \frac{S}{2\pi^2 D}\int_0^\infty dk\left\{\sum_{m=0}^{\infty}\varepsilon_m I_m\left(k_{eff}R_0\right)K_m\left[k_{eff}\left(R_0 + R_a\right)\right]\right.$$
$$\left.\cdot\left\langle 1 - \frac{K_m\left(k_{eff}R_0\right)}{I_m\left(k_{eff}R_0\right)}\frac{I_m\left[k_{eff}\left(R_0 - R_b\right)\right]}{K_m\left[k_{eff}\left(R_0 - R_b\right)\right]}\right\rangle\cos\left[m\left(\varphi - \varphi'\right)\right]\right\} \quad (2.4.1\text{conV})$$

For large *k*, hence large k_{eff}, the integrands of Eq. (2.4.1conC) and Eq. (2.4.1conV) become the following (Arfken et al., 2005)

$$I_m\left[k_{eff}\left(R_0 - R_a\right)\right]K_m\left(k_{eff}R_0\right)\left\langle 1 - \frac{I_m\left(k_{eff}R_0\right)}{K_m\left(k_{eff}R_0\right)}\frac{K_m\left[k_{eff}\left(R_0 + R_b\right)\right]}{I_m\left[k_{eff}\left(R_0 + R_b\right)\right]}\right\rangle$$
$$= \frac{e^{-k_{eff}R_a}}{2k_{eff}\sqrt{R_0\left(R_0 - R_a\right)}}\left(1 - e^{-2k_{eff}R_b}\right) \quad (2.4.2\text{conC})$$

$$I_m\left(k_{eff}R_0\right)K_m\left[k_{eff}\left(R_0 + R_a\right)\right]\left\langle 1 - \frac{K_m\left(k_{eff}R_0\right)}{I_m\left(k_{eff}R_0\right)}\frac{I_m\left[k_{eff}\left(R_0 - R_b\right)\right]}{K_m\left[k_{eff}\left(R_0 - R_b\right)\right]}\right\rangle$$
$$= \frac{e^{-k_{eff}R_a}}{2k_{eff}\sqrt{R_0\left(R_0 + R_a\right)}}\left(1 - e^{-2k_{eff}R_b}\right) \quad (2.4.2\text{conV})$$

It is again noted that as k_{eff} becomes sufficiently large both Eq. (2.4.2conC) and Eq. (2.4.2conV) asymptotically and quasi-exponentially approaches zero. Therefore in Eq. (2.4.1conC) and Eq. (2.4.1conV) the contribution of the integrands associated with *k* greater than a certain limit can be neglected. However, according to the IEEE standard for floating-point arithmetic (IEEE, 2008),

there is a limit for the biggest number and the smallest number to be stored. In Matlab the criterion (Moler et al., 1996) for overflow is 1.7977×10^{308} in decimal, and for underflow is 2.2251×10^{-308}. In Eq. (2.4.1conC) and Eq. (2.4.1conV), the modified Bessel functions of the first and second kinds are exponentially growing and decaying functions, for which overflow will readily occur for a large order *m* and underflow for a large argument *k*. To evaluate source and detector at the same azimuthal plane a larger order of *m* is necessary, and to evaluate the source and detector located longitudinally with the same azimuthal angle a large argument *k* is also becoming crucial. In both Eq. (2.4.1conC) and Eq. (2.4.1conV), since all the modified Bessel functions of the first and second kinds appear in pairs in the same order when multiplying with each other, a strategy of "pre-enlarge" and "pre-reduce" is implemented to ease the numerical manipulation. The principle is that instead of evaluating each modified Bessel function individually, the modified Bessel function of the first kind can be "pre-reduced" for large order *m* and the modified Bessel function of the second kind can be "pre-enlarged" by the same degree, by which the product of each pair shall remain unchanged. The outcome of this "pre-enlarge" & "pre-reduce" manipulation is demonstrated in Fig. 15(a) for a convex boundary of $R_0 = 2cm$, d changing from $0.1cm$ to $4cm$, k cutoff at 70, $\mu_a = 0.01cm^{-1}$, $\mu_s' = 10cm^{-1}$, $A = 1$, and $S = 1$. The *m* is summated from 0 to 150 (the dotted line with ripples) which was the limit to avoid overflow and underflow without applying the "pre-enlarge" & "pre-reduce" approach. After "pre-enlarge" & "pre-reduce", the summation can be made for *m* up to 500. Figure 15(a) indicates that this method of "pre-enlarge" & "pre-reduce" enables summing modified Bessel functions up to a large order of *m* by eliminating the ripples or noise seen when no such manipulation was employed.

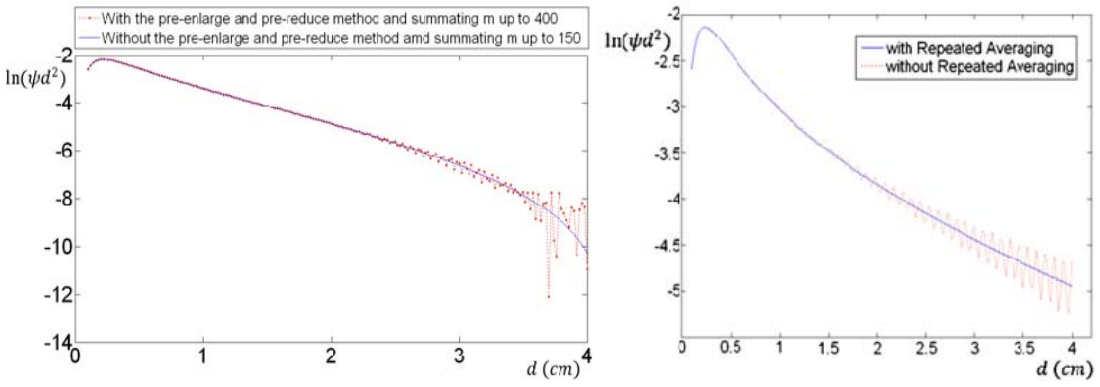

(a) (b)

Fig. 15 (a) The outcome of applying "pre-enlarge" and "pre-reduce" methods for $R_0 = 2cm$ in convex geometry. (b) The outcome of applying "repeated averaging" for $R_0 = 8cm$ in concave geometry.

Additionally, it is also found for Eq. (2.4.1conC) and Eq. (2.4.1conV) that the radius R_0 has a great effect on the evaluation outcome. For instance, when R_0 is as large as $8cm$ in Eq. (2.4.1conC), for $k = 40$, the integration does not converge sufficiently even for summating m up to 500 (the optical parameters are the same as used for Fig. 15(a)), but for a smaller radius $R_0 = 1cm$ the same integrand converges quickly at $m = 100$. A method of "repeated averaging" is thus employed to improve the convergence. The principle is to first examine if there is an oscillating pattern. If there is, the envelop of the maxima and minima of the oscillation is implemented to form a finite converging alternative series, and these maxima and minima are averaged through "repeated averaging" to approximate the value of the integrand. If an oscillating pattern is not formed, the last result is chosen as the value of the integrand. The results of applying such "repeated averaging" when evaluating Eq. (2.4.1conC) are shown in Fig. 15(b), in which m is summated up to 540 for $R_0 = 8cm$.

Based on these specific approaches of improving the outcome of numerical evaluations, the upper limits of k and m are evaluated individually for each set of computation conducted. For example, at a parameter setting of m terms up to 150, the effects of finite k cutoff value when evaluating Eq. (2.4.1) are shown in Fig. 16(a) for the concave boundary and Fig. 16(b) for the convex boundary. The difference between integrating k from 0 to 50 and from 0 to 100 is indistinguishable at the given scale, for both concave and convex boundaries. Therefore the cut-off value for k is set at 50 for this set of evaluation.

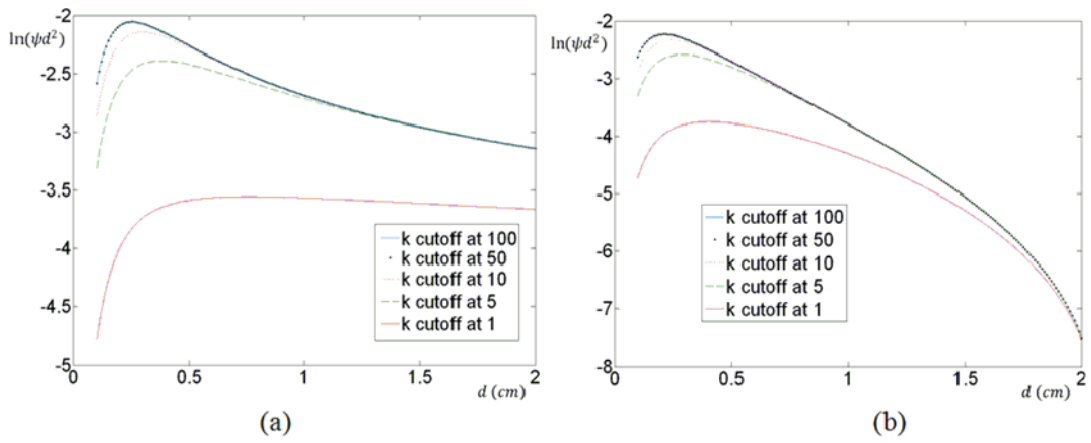

Fig. 16 Comparison of the contributions of k terms in the solution for source & detector located in the same azimuthal plane: (a) concave geometry; (b) convex geometry.

B. *Numerical evaluation of the general solutions for a cylinder applicator of radius up to 10cm*

The general solutions Eq. (2.4.1conC) and Eq. (2.4.1conV) are evaluated numerically with respect to a semi-infinite geometry in Fig. 17(a). The radius R_0 is chosen as 0.5cm, 1cm, 2cm, 5cm, and 10cm respectively. The figure is plotted for $\ln(\Psi d^2)$ versus d as it is the linear

relationship implied by Eq. (2.1.20) of semi-infinite geometry. It is noted again that d is assigned as the chord distance between the physical source and the detector points on the circular boundary. Therefore the maximum d for a radius of 0.5cm is 1cm, of 1cm is 2cm, etc., and the d is set to change from 0.1 to 4cm for the rest radii. On the azimuthal plane, the photon fluence rate associated with a given source-detector distance in a concave geometry is greater than that in a planar geometry for the same source-detector distance, and in a convex geometry it is smaller than that in a planar geometry. The overall qualitative feature, as anticipated, is that as the radius of the cylinder geometry increases, the photon fluence rate for the concave and convex boundaries asymptotically approaches that for a semi-infinite boundary.

C. *Numerical evaluation of the solutions approximated for a cylinder applicator of very large radius*

For the azimuthal geometry with large cylinder diameter, the distance terms in Eq. (2.2.27conC) and Eq. (2.2.27conV) can be expressed by

$$l_r = \left(R_a^2 + d^2 - \frac{R_a d^2}{R_0} \right)^{1/2} \qquad \text{(2.4.3conC)}$$

$$l_i = \left[\left(R_a + 2R_b \right)^2 + d^2 + \left(R_a + 2R_b \right) \frac{d^2}{R_0} \right]^{1/2} \qquad \text{(2.4.4conC)}$$

for concave boundary, and

$$l_r = \left(R_a^2 + d^2 + \frac{R_a d^2}{R_0} \right)^{1/2} \qquad \text{(2.4.3conV)}$$

$$l_i = \left[\left(R_a + 2R_b \right)^2 + d^2 - \left(R_a + 2R_b \right) \frac{d^2}{R_0} \right]^{1/2} \qquad \text{(2.4.4conV)}$$

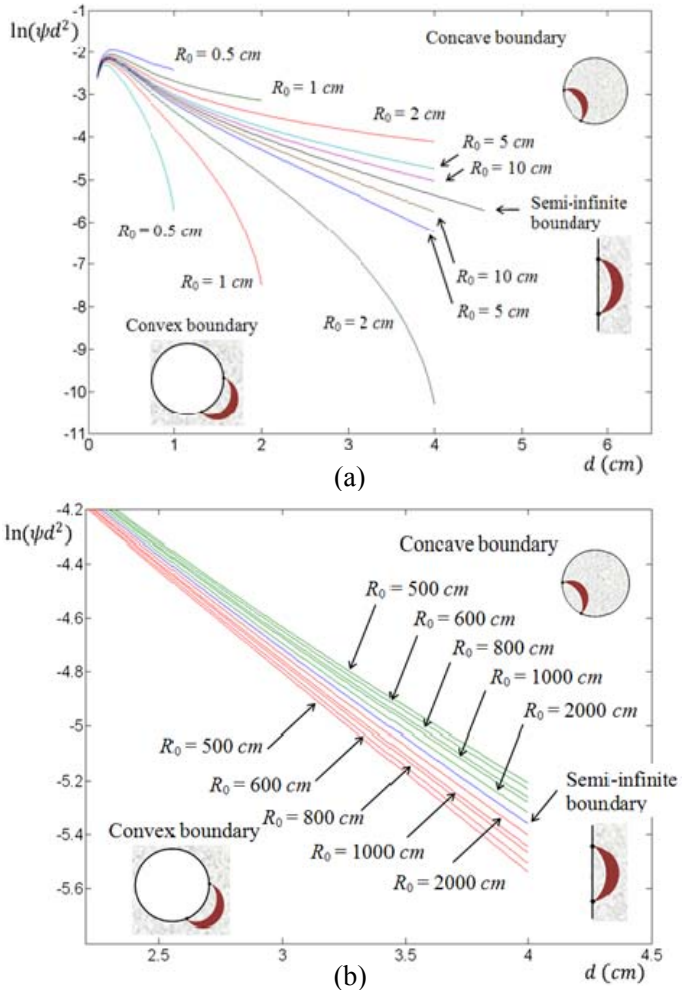

Fig. 17 (a) Comparison of the solutions for concave and convex geometries with respect to the semi-infinite geometry, for source & detector located at the same azimuthal plane. (b) Comparison of the solutions for concave and convex geometries having large cylinder radius with respect to the semi-infinite geometry, for source & detector located at the same azimuthal plane.

for convex boundary. The comparison of the two azimuthal geometries with respect to the semi-infinite geometry is given In Fig. 17(b), wherein the radius R_0 is chosen as 500*cm*, 600*cm*, 800*cm*, 1000*cm*, 2000*cm*. The results are shown only for *d* from 2.2 to 4*cm* to illustrate that both the concave and convex boundary asymptotically approaches the "linear" feature of the planar boundary for $\ln(\psi d^2)$ and *d*, but with radius-dependent differences in the slope and potentially in the intersection, both of which clearly will vanish as the radius becomes infinity.

2.4.2 Specific geometry---source and detector located longitudinally with the same azimuthal angle

The geometries shown in Fig. 18 are chosen to study the effect of concave or convex shape on photon diffusion for the source and detector located longitudinally with the same azimuth angle.

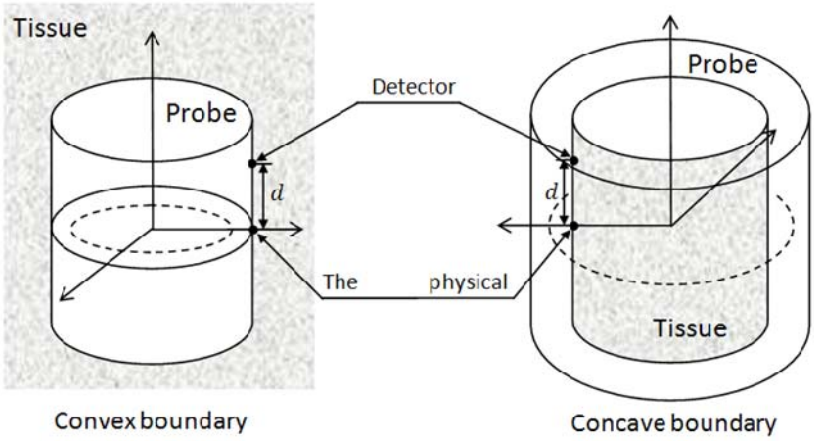

Fig. 18 The concave and convex geometries with source & detector located longitudinally with the same azimuthal angle.

A. Numerical approaches

For $\varphi = \varphi'$, we rewrite Eq. (2.2.26conC) and Eq. (2.2.26conV) as

$$\Psi = \frac{S}{2\pi^2 D}\int_0^\infty dk\left\{\cos\left[k(z-z')\right]\cdot\sum_{m=0}^{\infty}\varepsilon_m I_m\left[k_{eff}(R_0-R_a)\right]K_m\left(k_{eff}R_0\right)\right.$$

$$\left.\cdot\left\langle 1-\frac{I_m\left(k_{eff}R_0\right)}{K_m\left(k_{eff}R_0\right)}\frac{K_m\left[k_{eff}(R_0+R_b)\right]}{I_m\left[k_{eff}(R_0+R_b)\right]}\right\rangle\right\} \qquad (2.4.5\text{conC})$$

$$\Psi = \frac{S}{2\pi^2 D}\int_0^\infty dk\left\{\cos\left[k(z-z')\right]\cdot\sum_{m=0}^{\infty}\varepsilon_m I_m\left(k_{eff}R_0\right)K_m\left[k_{eff}(R_0+R_a)\right]\right.$$

$$\left.\cdot\left\langle 1-\frac{K_m\left(k_{eff}R_0\right)}{I_m\left(k_{eff}R_0\right)}\frac{I_m\left[k_{eff}(R_0-R_b)\right]}{K_m\left[k_{eff}(R_0-R_b)\right]}\right\rangle\right\} \qquad (2.4.5\text{conV})$$

The pervious analysis given for numerical evaluation of Eq. (2.4.2conC) and Eq. (2.4.2conV) still hold here, therefore the contribution due to large *k*, hence large k_{eff}, is neglected.

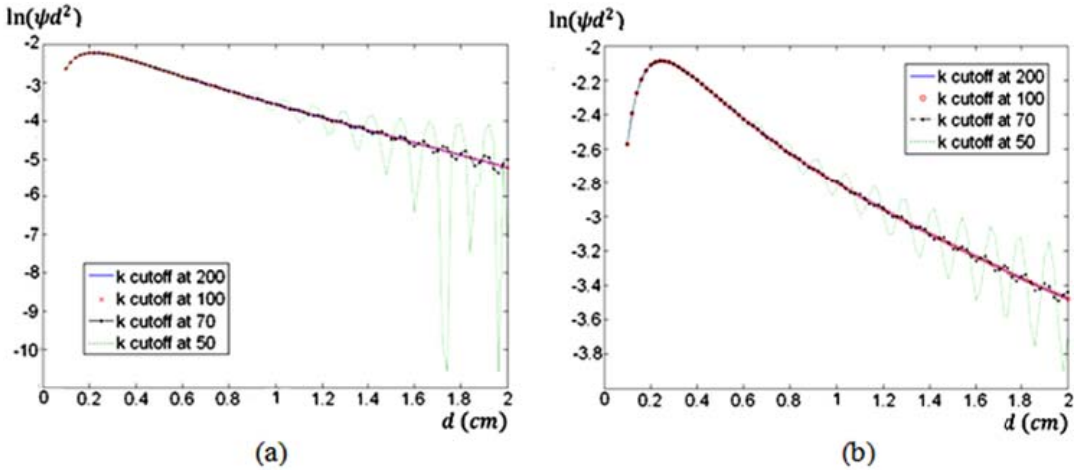

Fig. 19 Comparison of the contributions of k terms in the solution for source & detector located longitudinally with the same azimuthal angle: (a) concave boundary; (b) convex boundary.

The numerical manipulation methods of "pre-enlarge" & "pre-reduce" as well as "repeated averaging" discussed in section 2.4.1 are also applied here. The setting of *k* values are shown in Fig. 19(a) for concave boundary and Fig. 19(b) for convex boundary wherein the parameters used are $R_0 = 1cm$, d ranging from $0.5cm$ to $2cm$, and *m* summing from 0 to 100. It is observed that the plots for *k* cutoff at 100 and 200 are indistinguishable at the given scale. For this set of computation the up-limit for *k* is then set at 100. This up-limit of *k* is higher than that one used for evaluating the azimuthal plane. It is also found that the up-limit for *m* can be chosen much lower than the one used for evaluating the azimuthal plane. Again the upper limits of *k* and *m* are evaluated individually for each set of computation.

B. *Numerical evaluation of the general solutions for a cylinder applicator of radius up to 6cm*

The general solutions Eq. (2.4.5conC) and Eq. (2.4.5conV) are evaluated numerically with respect to semi-infinite geometry in Fig. 20(a). The radius R_0 is chosen as 1*cm*, 2*cm*, 3*cm*, and 6*cm* respectively. The figure is again plotted for $\ln(\Psi d^2)$ versus d as it is the linear relationship implied by Eq. (2.1.20) for a semi-infinite geometry, and d is the longitudinal distance between the physical source and the detector points on the circular boundary. The d in this geometry is not limited in range, but a range from 0.1 to 4*cm* is chosen for comparison with the azimuthal geometry of Fig. 17. Along the longitudinal direction, the photon fluence rate associated with a given source-detector distance in a concave geometry is smaller than that in a planar geometry for the same source-detector distance, and in a convex geometry it is greater than that in a planar geometry. The overall qualitative feature, as anticipated, is that as the radius of the cylinder geometry increases, the photon fluence rate for the concave and convex boundaries asymptotically approaches that for a semi-infinite geometry.

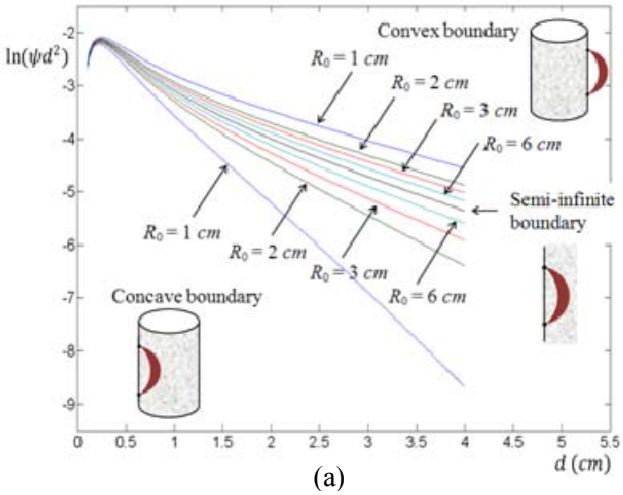

(a)

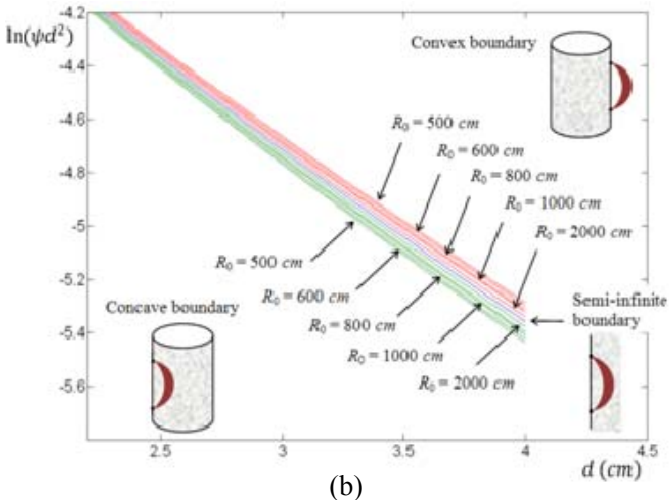

(b)

Fig. 20 (a) Comparison of the solutions for concave and convex geometries with respect to the semi-infinite geometry, for source & detector located longitudinally with the same azimuthal angle. (b) Comparison of the solutions for concave and convex geometries having large cylinder diameter with respect to the semi-infinite geometry, for source & detector located longitudinally with the same azimuthal angle.

C. *Numerical evaluation of the solutions for a cylinder applicator of very large radius*

For the longitudinal geometry with larger cylinder diameter, the distance terms in Eq. (2.2.27conC) and Eq. (2.2.27conV) can be expressed by

$$l_r = \left(R_a^2 + d^2\right)^{1/2} \tag{2.4.6}$$

$$l_i = \left[\left(R_a + 2R_b\right)^2 + d^2\right]^{1/2} \tag{2.4.7}$$

for both concave and convex geometries. The comparison of the two longitudinal geometries with respect to the semi-infinite geometry is given in Fig. 20(b) with the rest of the parameters the same as in Fig. 17(b). Again, both the concave and convex geometry asymptotically approaches the "linear" feature of the planar boundary for $\ln(\psi d^2)$ and d, but with radius-dependent differences in the slope and potentially in the intersection, both of which clearly will vanish as the radius becomes infinity.

Finally in terms of the computation time, for each single curve in Fig. 17 or Fig. 20 that includes on average 100 data points, it takes approximately 5 minutes to formulate on a 2.8 GHz CPU with 1.0GB of memory.

2.5 Discussions

The solution to photon diffusion in an infinite homogeneous medium derived in cylindrical coordinates likely will involve two Bessel functions. The solution could have different expressions, depending on the type (normal or modified, the first kind or the second kind) of Bessel functions used and how these functions being integrated in the solution. In Eq. (2.2.25), we have expressed the solution using the modified Bessel functions. The integration part of Eq. (2.2.25) is identical to that of the solution to Poisson equation in cylindrical coordinates given in (Jackson, 1998), except that the argument contains k_{eff} instead of k as in (Jackson, 1998). This solution may be advantageous as it demonstrates clearly the different roles of the source and the field points in the solution, by differentiating the radial coordinates of the source and field points

into the arguments specific to different kinds of the modified Bessel functions such that both of the modified Bessel functions will become valid in the geometry of interest.

Applying the solution in Eq. (2.2.25) leads to physically explicit interpretation in the two equations of Eq. (2.2.26) for a medium involving an external or internal cylindrical boundary. The equations in Eq. (2.2.26) are composed of two parts in the parenthesis: the first part is associated with the "real" isotropic source, and the second part is the contribution of the "image" source term that is represented by the "real" source term scaled by a factor. The scaling factor is related to the radius of the cylinder and the reflective index mismatch of the cylinder-medium interface that determines where the extrapolated boundary shall be placed. The equations in Eq. (2.2.27), which are derived for large radius concave and convex boundaries, are given in a format similar to that for semi-infinite geometry but with a shape-curvature-associated term that approaches unity as the radius of the cylinder approaches infinity.

The numerical evaluations in section 2.4 demonstrate the qualitative correctness of the analytic solutions in Eq. (2.2.26) for the two circular cylindrical geometries, within the limit of the current computer arithmetic. It is clearly shown that the solutions given in Eq. (2.2.26) asymptotically approach the semi-infinite medium solution as the applicator radius reaches infinity. For the specific case of having the source and detector located azimuthally on the same axial plane, the photon fluence rate is greater than the semi-infinite geometry for the concave boundary and smaller for the convex boundary given the same source-detector distance. This can be interpreted by the fact that, for the same source-detector distance, more near-field photons from the source could scatter and reach the detector in the concave geometry than in the semi-infinite geometry, but in the convex geometry it does the opposite. For the specific case of having the source and detector located longitudinally on the same azimuthal angle, the photon fluence rate is smaller than the semi-infinite geometry for the concave boundary and greater for the convex boundary given the same source-detector distance. This again can be interpreted by the fact that, for the same source-detector distance, less near-field photons from the source could

scatter and reach the detector in the concave geometry than in the semi-infinite geometry, but in the convex geometry it does the opposite.

2.6 Conclusion

The steady-state photon diffusion in a homogeneous medium bounded externally or internally by an infinitely long circular cylindrical applicator has been analyzed. The geometry of a diffusive medium bounded externally by a cylindrical applicator resembles that of imaging externally-accessible biological tissue such as the breast using a ring-type array. The geometry of a diffusive medium bounded internally by a cylindrical applicator resembles that of imaging internally-accessible biological tissue such as prostate using trans-rectal probe. Solutions to steady-state photon diffusion in these two geometries are derived in cylindrical coordinates by applying the extrapolated boundary condition and expressed in modified Bessel functions of the first and second kinds. Approximate solutions for large cylinder radius are also derived to the format close to that for semi-infinite geometry by including a shape-radius-associated term. The numerical evaluations are provided for the cases of having the source and the detector positioned only along the azimuthal or longitudinal directions. The results demonstrated that compared with a semi-infinite boundary, the concave boundary has smaller photon fluence decay in the azimuth direction but greater photon fluence decay along the longitudinal direction, compared with a semi-infinite geometry having the same source-detector distance. On the contrary, the convex boundary has greater photon fluence decay in the azimuth direction but smaller photon fluence decay along the longitudinal direction. As the radius of the concave or convex circular applicator becomes infinitely large, the results for these specific geometries reach the well-known condition for a semi-infinite medium, as expected. This theory and “qualitative” numerical evaluation

constitute the Chapter II of this thesis, which will be quantitatively examined in Chapter III, and extended to frequency-domain analysis in Chapter V.

CHAPTER III

QUANTITATIVE EXAMINATIONS OF THE STEADY-STATE THEORY

3.1 Introduction (Zhang A, Xu G et al., 2011)

In Chapter II, the solutions to the steady-state photon diffusion associated with "concave" and "convex" geometries were derived by employing the extrapolated boundary condition (Haskell et al., 1994; Contini et al., 1997) and expressed in closed forms using the modified Bessel functions. The validity of the approach in (Zhang et al., 2010), which has to our knowledge for the first time unified the analytic treatments of photon diffusion in both "concave" and "convex" geometries, was examined qualitatively for the case wherein the radial dimension of the tissue-applicator interface would reach infinity. As is expected, the decay rate of photon fluence for the case of applicator-radius approaching infinity was found to asymptotically reach that for a planar-interface case or the semi-infinite geometry. The analytic approach was then applied to the "concave" and "convex" geometries with the radial dimensions of the tissue-applicator interfaces comparable to those found in practical applications. For these "practical" geometries, the work in Chapter II further examined two specific configurations: (1) the source and the detector have the same longitudinal coordinate and are placed along the azimuth direction on the boundary; (2) the source and the detector have the same azimuth angle and are placed along the longitudinal direction on the boundary. For the case (1), which is called "*case-azi*" in this work, it was predicted that the decay rate of photon fluence would become smaller in the "concave" geometry and greater in the "convex" geometry, respectively, than that in a semi-infinite geometry for the same source–detector distance. For the case (2), which is called "*case-longi*" in this work, it was projected that the decay rate of photon fluence would be greater in the

"concave" geometry and smaller in the "convex" geometry, respectively, than that in a semi-infinite geometry for the same source–detector distance.

This chapter examines the predictions given in Chapter II for steady-state photon diffusion in the *case-azi* and *case-longi* configurations within the "concave" and "convex" geometries, by the following quantitative methods: (a) finite-element-method (FEM), (b) Monte Carlo (MC) simulation, and (c) experimental measurement. The predictions for *case-azi* and *case-longi* configurations in Part I, which were based upon solving the equation of photon diffusion analytically in the studied geometries, is to be firstly examined by solving the same equation of photon diffusion numerically in the same geometries using the widely-validated FEM solver. It is expected that the FEM-based results will support the analytic solution that has been proposed, but as both FEM and analytical solutions are based upon the model of photon diffusion, the expected model-data match between these two doesn't necessarily substantiate the validity of the analytic approach. The ultimate verification of any analytic approach of photon propagation requires examining it against experimental measurement or the "gold-standard" numerical method of MC. Among the three quantitative methods of FEM, MC, and experimental measurement employed in this work the experimental examination apparently has the least flexibility in the study design, therefore it becomes rational to conduct FEM and MC examinations by employing as many available parameters as possible for the experimental measurements. It is noted that the "infinitely" long cylindrical applicator modeled in Chapter II cannot be reproduced in any of the three methods of FEM, MC and experimental examination, but it can be approximated by one cylindrical applicator whose longitudinal dimension is much greater than its radial dimension, e.g. with large length-to-radius ratio.

The rest of this chapter is structured into the following sections: Section 3.2 reprints the analytic results derived in Chapter II that are relevant to the predictions for *case-azi* and *case-longi* configurations; Section 3.3 details the configurations of the FEM, MC, and experimental examinations; Section 3.4 evaluate the effect of the measurement errors associated with the

positioning of the source and detector due to the limitations of the experimental study, and discuss the rationale of minimizing the error-induced data-model deviation when the experimental measurements are grouped with FEM and MC for examining the analytic predictions; and Section 3.5 examines the analytic predictions of *case-azi* and *case-longi* configurations in two "concave" and three "convex" applicator dimensions against the FEM, MC, and experimental results, for a given set of medium optical properties.

3.2 Relevant analytic results derived in Chapter II

Same as in Chapter II, the following notations have been used: $\vec{r}_0 = (R_0, \varphi', z')$ is the position of the source, $\vec{r} = (R_0, \varphi, z)$ is the position of the field or the detector, S is the intensity of the source, Ψ is the photon fluence rate at the field/detector position, μ_a is the absorption coefficient, μ_s' is the reduced or transport scattering coefficient, $D = [3(\mu_a + \mu_s')]^{-1}$ is the diffusion coefficient, $R_a = 1/\mu_s'$ is the mean path-length for the photon to lose its history of incident direction and is used for modeling the directional source as an isotropic source placed into the medium, $R_b = 2AD$ is the distance from the extrapolated boundary to the physical boundary wherein A is a parameter determined by the refractive index mismatch across the tissue-applicator interface.

The steady-state photon fluence rate Ψ associated with a "concave" geometry of radius R_0 is

$$\Psi = \frac{S}{2\pi^2 D}\int_0^\infty dk \left\{ \cos\left[k(z-z')\right] \sum_{m=0}^{\infty} \varepsilon_m I_m\left[k_{eff}(R_0 - R_a)\right] K_m\left(k_{eff} R_0\right) \right.$$
$$\left. \cdot \left\langle 1 - \frac{I_m\left(k_{eff} R_0\right)}{K_m\left(k_{eff} R_0\right)} \frac{K_m\left[k_{eff}(R_0 + R_b)\right]}{I_m\left[k_{eff}(R_0 + R_b)\right]} \right\rangle \cos\left[m(\varphi - \varphi')\right] \right\} \quad (3.2.1\text{conC})$$

where I_m and K_m are the modified Bessel functions of the first and second kind at order m, respectively. Similarly, the steady-state photon fluence rate Ψ associated with a "convex" geometry of radius R_0 is

$$\Psi = \frac{S}{2\pi^2 D}\int_0^\infty dk\left\{\cos\left[k(z-z')\right]\sum_{m=0}^{\infty}\varepsilon_m I_m\left(k_{eff}R_0\right)K_m\left[k_{eff}\left(R_0+R_a\right)\right]\right.$$
$$\left.\cdot\left\langle 1-\frac{K_m\left(k_{eff}R_0\right)}{I_m\left(k_{eff}R_0\right)}\frac{I_m\left[k_{eff}\left(R_0-R_b\right)\right]}{K_m\left[k_{eff}\left(R_0-R_b\right)\right]}\right\rangle\cos\left[m(\varphi-\varphi')\right]\right\} \quad (3.2.1\text{conV})$$

For equations in Eq. (3.2.1), if the source and the detector locate at the same azimuth plane, e.g. in *case-azi* configuration, we have:

$$\Psi = \frac{S}{2\pi^2 D}\int_0^\infty dk\left\{\sum_{m=0}^{\infty}\varepsilon_m I_m\left[k_{eff}\left(R_0-R_a\right)\right]K_m\left(k_{eff}R_0\right)\left\langle 1-\frac{I_m\left(k_{eff}R_0\right)}{K_m\left(k_{eff}R_0\right)}\frac{K_m\left[k_{eff}\left(R_0+R_b\right)\right]}{I_m\left[k_{eff}\left(R_0+R_b\right)\right]}\right\rangle\cos\left[m(\varphi-\varphi')\right]\right\}$$
(3.2.2conC)

$$\Psi = \frac{S}{2\pi^2 D}\int_0^\infty dk\left\{\sum_{m=0}^{\infty}\varepsilon_m I_m\left(k_{eff}R_0\right)K_m\left[k_{eff}\left(R_0+R_a\right)\right]\left\langle 1-\frac{K_m\left(k_{eff}R_0\right)}{I_m\left(k_{eff}R_0\right)}\frac{I_m\left[k_{eff}\left(R_0-R_b\right)\right]}{K_m\left[k_{eff}\left(R_0-R_b\right)\right]}\right\rangle\cos\left[m(\varphi-\varphi')\right]\right\}$$
(3.2.2conV)

and if the source and the detector locate longitudinally with the same azimuth angle, e.g. *in case-longi* configuration, we have:

$$\Psi = \frac{S}{2\pi^2 D}\int_0^\infty dk\left\{\cos\left[k(z-z')\right]\sum_{m=0}^{\infty}\varepsilon_m I_m\left[k_{eff}\left(R_0-R_a\right)\right]K_m\left(k_{eff}R_0\right)\left\langle 1-\frac{I_m\left(k_{eff}R_0\right)}{K_m\left(k_{eff}R_0\right)}\frac{K_m\left[k_{eff}\left(R_0+R_b\right)\right]}{I_m\left[k_{eff}\left(R_0+R_b\right)\right]}\right\rangle\right\}$$
(3.2.3conC)

$$\Psi = \frac{S}{2\pi^2 D}\int_0^\infty dk\left\{\cos\left[k(z-z')\right]\sum_{m=0}^{\infty}\varepsilon_m I_m\left(k_{eff}R_0\right)K_m\left[k_{eff}\left(R_0+R_a\right)\right]\left\langle 1-\frac{K_m\left(k_{eff}R_0\right)}{I_m\left(k_{eff}R_0\right)}\frac{I_m\left[k_{eff}\left(R_0-R_b\right)\right]}{K_m\left[k_{eff}\left(R_0-R_b\right)\right]}\right\rangle\right\}$$
(3.2.3conV)

3.3 Configuration of the quantitative examinations

3.3.1 Configuration of the FEM solver to the equation of photon diffusion

The FEM-based computation (Huang et al., 2003; Zhou et al., 2008) of photon diffusion is based on our work (Musgrove et al., 2007) of solving the equation of steady state photon diffusion under a Robin type boundary condition using NIRFAST (Dehghani et al., 2009). It is noted that the source term in FEM is often defined as a distributed, Gaussian source, matching the intensity profile at the tip of the optical fiber, and the source may therefore be defined over more than one element (Dehghani et al., 2009). The source term in FEM is thus different from the basis of Green's function in analytic treatment. This difference is expected to cause a mismatch between FEM and analytical results as the source-detector distance becomes comparable to the spatial dimension of the Gaussian source even though both methods are based on the same model of photon propagation. The finite-element meshes for the *case-azi* and *case-longi* configurations of the concave geometry are shown in Fig. 21(a) and (b), respectively. Two sets of the concave-geometry are considered: one has a radius of 0.95*cm* and a length of 40*cm*, and the other has a radius of 2.53*cm* and a length of 40*cm*. The radii of the two concave-geometry sets are chosen the same as those used in the experiments, but the length-to-radius ratios of the two geometry sets are 2.62 times of those used in the experimental study. The larger length-to-radius ratio is necessary to bridging between the model prediction based on an infinitely long "concave" geometry and the experimental data obtained from a long yet finite "concave" applicator. For the *case-azi* geometry denser meshes are placed along the mid-azimuth plane on the boundary for evaluating the solution along the azimuth direction. Similarly for the *case-longi* geometry denser meshes are placed along the longitudinal direction on the boundary for evaluating the solution along the longitudinal direction. The domain of FEM modeling with a radius of 2.53*cm* is discretized into a mesh of 22182 tetrahedral elements and 4988 nodes. The domain of FEM modeling with a radius

of 0.95*cm* is discretized into mesh of the same density as that in the radius of 2.53*cm*. For the convex geometry the FEM volumes used for both *case-azi* and *case-longi* configurations is illustrated in Fig. 21(c). Three sets of the "convex" geometry are considered: all have a longitudinal dimension of 40*cm* and an outer radius of 15*cm*, and the inner radii are 1.27*cm*, 2.41*cm* and 5.07*cm*, respectively. The radii of the three "convex" geometry sets are chosen the same as those found in the experiments, but the length-to-radius ratios of the three geometry sets are also 2.62 times of those employed in the experimental study as that in the "concave" geometry. The discretized domain of the "convex" geometry is illustrated in Fig. 21(d) which shows only the *case-azi* configuration and does not visualize the meshes at the outer surfaces for the purpose of clarification. The domain of FEM modeling with an inner radius of 1.27*cm* is discretized into a mesh of 90856 tetrahedral elements and 17545 nodes. The domains of FEM modeling with inner radii of 2.31*cm* and 5.07*cm* are discretized into meshes of the same density as that in the radius of 1.27*cm*. The value of A is experimentally determined (detailed in section 3.3.4) as being 1.86 for the interface between the tissue/medium and the applicator.

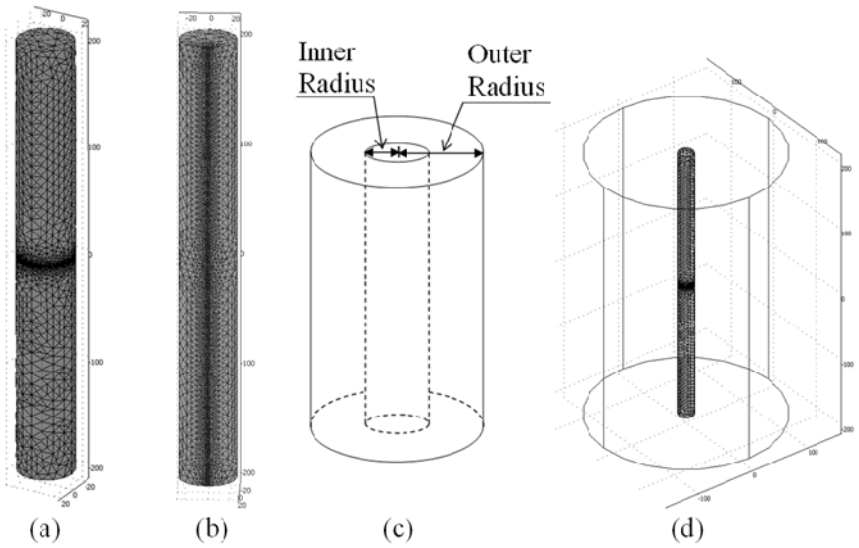

Fig. 21 3D-rendering of the finite element mesh of the cylindrical applicator: (a) "concave" geometry for the *case-azi* configuration shown with denser mesh along the azimuth direction at the outer surface of the cylinder domain; (b) "concave" geometry for the *case-longi* configuration shown with denser mesh along the longitudinal direction at the outer surface of the cylinder domain; (c) "convex" geometry for both *case-azi* and *case-longi* configurations; (d) discretization of the "convex" imaging volume for the *case-azi* configuration shown with denser mesh along the azimuth direction at the inner surface of the cylinder domain.

3.3.2 Configuration of the Monte Carlo simulation

The MC model was adapted from a program previously developed for simulating photon migration in cylindrical blood vessels (Yao et al., 2005). The "concave" and "convex" geometries for MC simulation are illustrated in Fig. 22 with (a) and (c) for the *case-azi* configurations, and (b) and (d) for the *case-longi* configurations, respectively. For both *case-azi* and *case-longi*

configurations, two sets of the "concave" applicator dimensions are considered: one has a radius of 0.95*cm* and a length of 40*cm*, the other has a radius of 2.53*cm* and a length of 40*cm*, and three sets of the "convex" applicator dimensions are considered: all have a longitudinal dimension of 40*cm* and an outer radius of 15*cm*, and the inner radii are 1.27*cm*, 2.41*cm* and 5.07*cm*, respectively. The dimensions of these geometries are identical to those used for FEM evaluations. A single point "pencil-beam" source and a set of isotropic detectors (1*mm* in diameter) were positioned at the tissue-applicator interface as shown in Fig. 22 based on the *case-azi* or *case-longi* configuration. The experimentally determined value of A = 1.86 on the tissue-applicator interface is implemented in MC as a 30% probability of photon re-entering the modeled tissue-domain after reaching the applicator boundary. The number of incident photons ranged from 5×10^7 for "convex" geometry with small radius to 2×10^8 for the "concave" geometry. All recordings had smaller than 10% error (the ratio of the standard deviation to the mean).

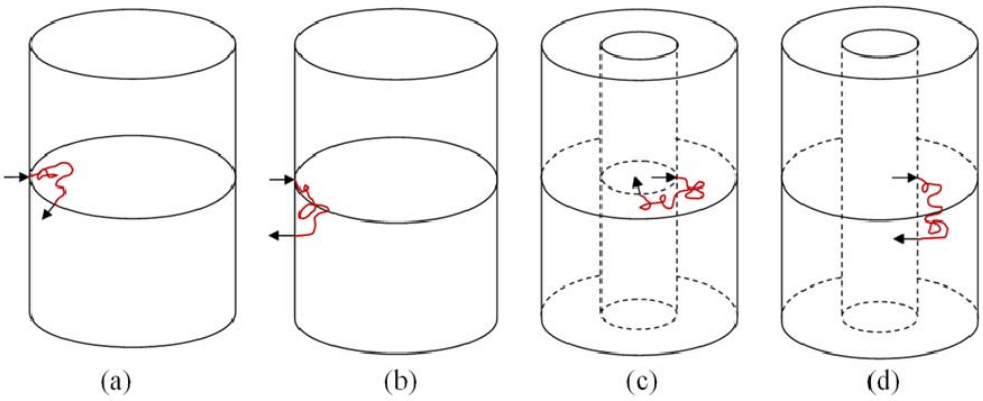

Fig. 22 Geometry of the Monte Carlo simulation: (a) "concave" geometry for *case-azi* configuration; (b) "concave" geometry for *case-longi* configuration; (c) "convex" geometry for *case-azi* configuration; (d) "convex" geometry for *case-longi* configuration.

3.3.3 Configuration of the experimental study

A. Dimensions of the applicators in "concave" and "convex" geometries

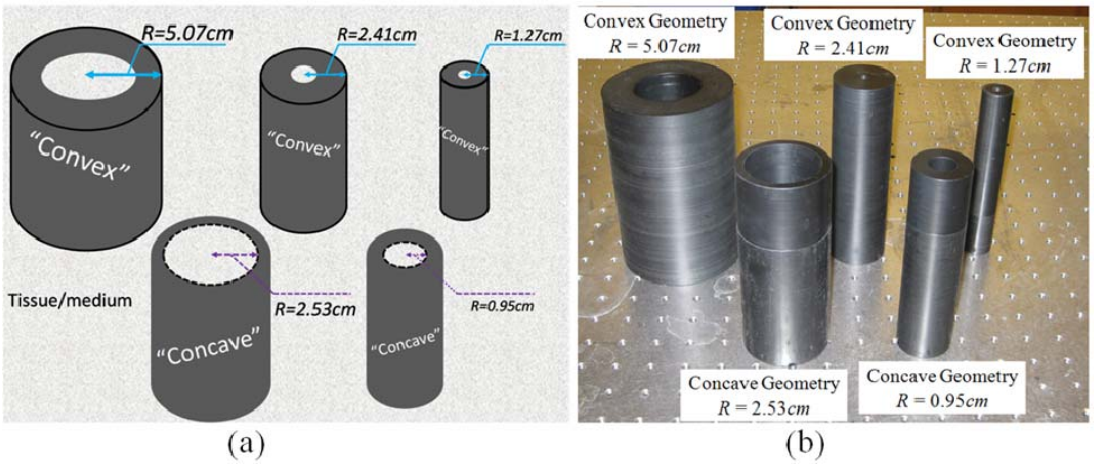

Fig. 23 Five cylindrical applicators made from the same black acetal material, shown by the: (a) sketch, and (b) photograph. The lower-front 2 with radii of 0.95*cm* and 2.53*cm* were used for the "concave" geometry and the upper-rear 3 with radii of 1.27*cm*, 2.41*cm* and 5.07*cm* were used for the "convex" geometry.

Five pieces of cylindrical applicators, shown schematically in Fig. 23(a) and photographed in Fig. 23(b), were fabricated from pre-sorted 6" long (15.24*cm* in length, comparing to the 40*cm* long imaging domain used for FEM and MC simulation) raw black acetal materials. These cylindrical pieces could be used for both "concave" and "convex" imaging geometries; however, due to the difficulty of fabricating both the "external" and "internal" surfaces of the same cylindrical applicator under identical machining processes to make the boundary conditions consistent, each piece was used for either the "concave" or "convex" imaging geometry, but not for both. Two applicator pieces with inner radii of 0.95*cm* and 2.53*cm*,

respectively, were used as the "concave" imaging geometry whereat the measurement was made along the inner surface (the dashed line on the two pieces at the lower row of Fig. 23(a)) *enclosing* the tissue-medium, and three applicator pieces with outer radii of 1.27*cm*, 2.41*cm* and 5.07*cm*, respectively, were used as the "convex" imaging geometry whereat the measurement was made along the outer surface (the solid line on the three pieces at the upper row of Fig. 23(a)) *enclosed by* the tissue-medium. Therefore for each group of *case-azi* or *case-longi* measurements, the results contained 2 sets from the "concave" geometries with different radii and 3 sets from the "convex" geometries with different radii.

B. Configuration of the measurement assembly using the cylindrical applicator

The analytic treatments in Chapter II utilized a well-known important approach of modeling a directional illumination (from a fiber) as an isotropic source placed into the medium at a distance of $1/\mu_s'$ from the directional incident point. The FEM solver adopted this approach of modeling a fiber illumination by simply placing an "equivalent" isotropic source at the $1/\mu_s'$ distance into the medium. In the MC simulation, since the incident photon is strictly forward launched ("pencil beam"), the condition of "equivalent" isotropic source at the $1/\mu_s'$ distance is also satisfied. In the experimental study, placing the facet of an illumination fiber evenly on the applicator-tissue interface can mimic the condition of "equivalent" isotropic source; however, the accuracy of the setup was limited by the variable practicability among the different applicator pieces employed and would not be as desirable as those in FEM and MC studies. The examination of the analytic predictions for *case-azi* and *case-longi* configurations also was in need of continuously translating either the source or the detector fiber azimuthally or longitudinally, which further discouraged the experimental implementation that involved inserting a fiber in the wall of the applicator piece unless it would be the only feasible choice. It

has been argued that the measurement of diffuse photon is insensitive to the orientation of the detector fiber (Polishchuk et al., 2007); nevertheless, using an isotropic detector shall provide measurement of the photon diffusion that is minimally affected by the orientation of the detector fiber. In light of all these restrictions, the experimental design physically placed a fiber with an isotropic diffuser tip as the source in the medium at a distance of $1/\mu_s'$ from the tissue-applicator boundary instead of inserting a regular fiber through the applicator wall, and used a fiber with isotropic sensing tip as the detector.

A diffuser (Medlight SD200) with a spherical tip of 2*mm* in diameter was used as the isotropic source and an isotropic probe (Medlight IP159) with a spherical tip of 1.59*mm* in diameter was used for detection of the diffuse photon. The 785*nm* light from a laser diode (Thorlabs, model HL7851G) operating at constant power mode was fiber-coupled to the spherical diffuser. The isotropic detector probe was coupled to a spectrometer (Princeton Instruments, SpectraPro-2300i, not necessary for the measurement but kept for system integrity and convenience of use) for read-out of the detected photon intensity by a 16-bit CCD camera (Photometrics Cascade 512F).

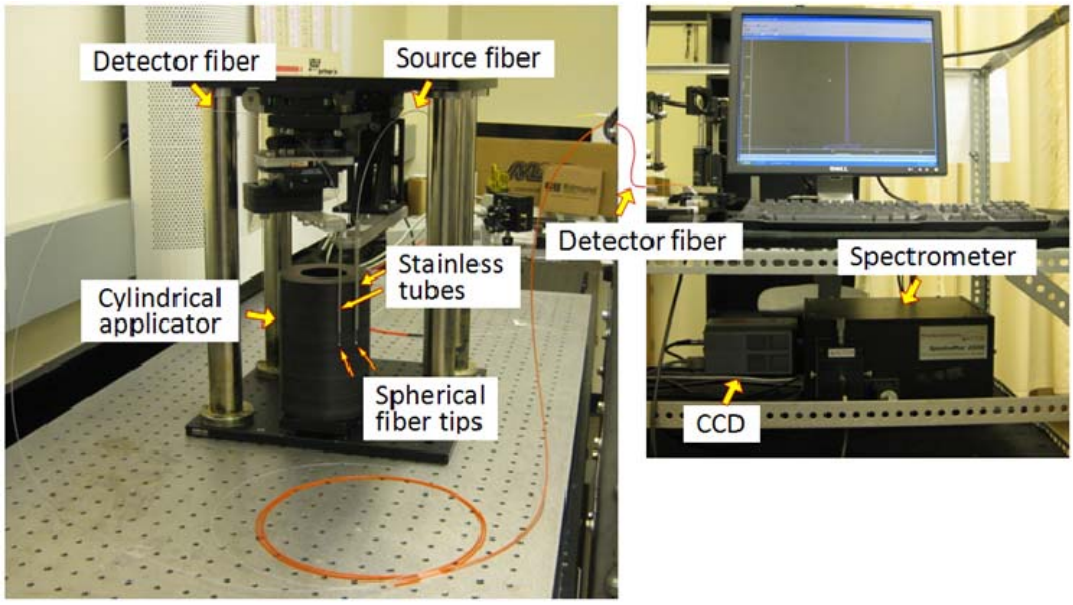

Fig. 24 Photographs of the experimental setup for the *case-azi* configuration in the "convex" geometry. The tank that housed the intralipid solution for immersing the setup is not shown.

The source and the detector fibers were fixed individually in stainless tubes (except for the detection fiber shown in the configuration in Fig. 26(a) only) which were then fixated to the positioning structure. The stainless tube for housing the source fiber had a diameter of 4.76*mm* (3/16") and the one for fixing the detector fiber has a diameter of 3.18*mm* (1/8"). Figure 24 is an exemplary photograph of the complete setup for measurement of *case-azi* configuration in the "convex" geometry, wherein the source and detector fibers were placed azimuthally and outside of the cylindrical applicator at the same longitudinal coordinate. The entire positioning assembly as shown on the bread-board was then immerged in a large tank filled with bulk Intralipid solution as the homogenous medium.

C. Control of the source-detector distance for measurement in the case-azi configuration

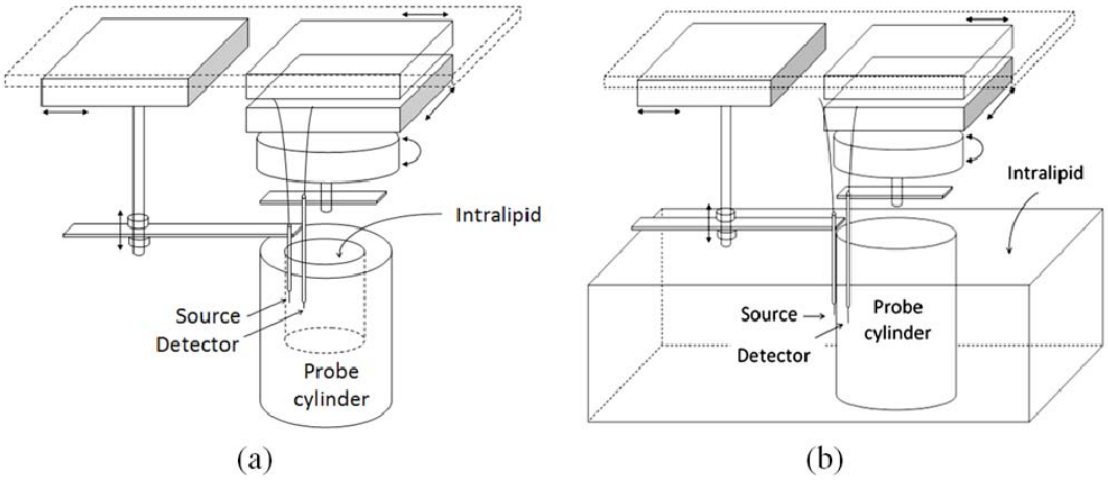

Fig. 25 Illustration of the experimental setup for the *case-azi* configurations. (a) "concave" geometry with the source and the detector placed azimuthally in proximity to the inner surface of the cylinder applicator; (b) "convex" geometry with the source and the detector placed azimuthally in proximity to the outer surface of the cylinder applicator.

For the *case-azi* configuration in "concave" geometry as shown in Fig. 25(a), the isotropic detector was fixed at the inner surface of the cylindrical applicator and the isotropic source was placed at a distance of $1/\mu_s'$ inward from the inner surface. The isotropic source rotated iso-azimuthally with respect to the isotropic detector and the center of the applicator curvature. The intralipid solution filled the inside of the cylindrical applicator. For the *case-azi* configuration in "convex" geometry as shown in Fig. 25(b), both the isotropic source and detector were placed at the outer surface of the cylinder applicator, with the source placed a distance of $1/\mu_s'$ outward from the outer surface. The isotropic source rotated iso-azimuthally with respect to the isotropic detector and the center of the applicator curvature. The intralipid solution filled up the tank that

housed the cylinder applicator. The azimuth plane that contains the source and the detector was at halfway along the longitudinal working range of the cylinder applicator to minimize the effect of the finite-length of the applicator. The chord distance *d* between the positions of the modeled directional source and the detector on the applicator surface was calculated by $d = 2R\sin(\theta/2)$, where the angle θ between the azimuth coordinates of the source and the detector was directly read out from the rotational stage controlling the source position.

D. Control of the source-detector distance for measurement in the case-longi configuration

For the *case-longi* configuration in "concave" geometry as shown in Fig. 26(a), the isotropic detector fiber without the stainless tube passed through the wall of the cylindrical applicator and was fixed at the inner surface of the applicator. The isotropic source was placed at a distance of $1/\mu_s'$ inward from the inner surface of the applicator and translated longitudinally. The intralipid solution filled the inside of the cylindrical applicator. For the *case-longi* configuration in "convex" geometry as shown in Fig. 26(b), the cylindrical applicator was placed horizontally. The isotropic detector housed by the stainless tube was placed on the outer surface of the applicator. The isotropic source was placed a distance of $1/\mu_s'$ outward from the outer surface, and translated longitudinally with respect to the isotropic detector. The intralipid solution filled the tank that housed the cylindrical applicator and most part of the fiber-holding stainless tubes.

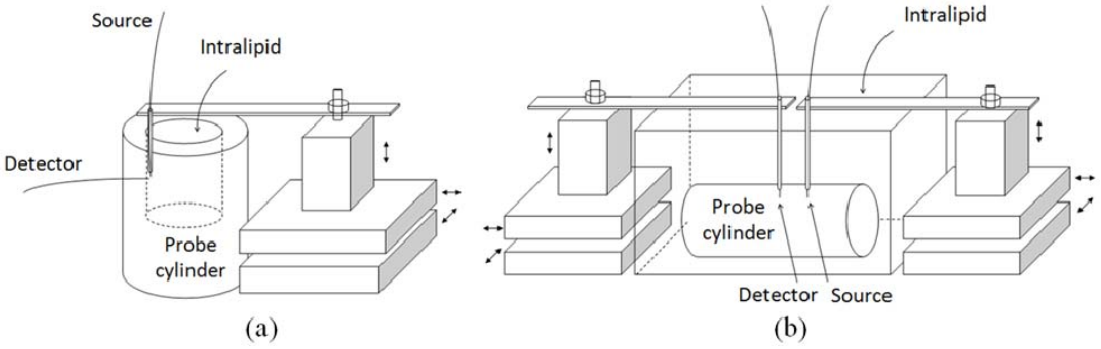

Fig. 26 Illustration of the experimental setup for the *case-longi* configurations. (a) "concave" geometry with the detector penetrating the cylinder wall and the source placed longitudinally in proximity to the inner surface of the cylinder applicator; (b) "convex" geometry with the source and the detector placed longitudinally in proximity to the outer surface of the cylinder applicator.

In the experimental study, all measurements were based on a bulk Intralipid solution of 0.5% in concentration. This concentration of Intralipid solution gave $\mu_s' = 5cm^{-1}$ at $785nm$ (Michels et al., 2008), with which $1/\mu_s' = 2mm$ so there was sufficient space to place the 1mm-radius spherical diffuser source away from the applicator surface, and the scattering-dominant condition was also satisfied as $\mu_a = 0.025\,cm^{-1}$ (Driver et al., 1989). Using single concentration of the Intralipid solution undoubtedly limited the experimental examinations to single set of μ_a and μ_s' of the medium properties; however, if the analytical treatment had been incorrect, none of the predictions made could have matched with the experimental results.

3.3.4 Experimental determination of the ***A*** *value*

In the experimental examinations all of the parameters appearing in Eqs. (3.2.2conC), (3.2.2conV) or (3.2.3conC), (3.2.3conV) were known except for the A value appearing in

$R_b = 2AD$. A is determined by the refractive index mismatch between an applicator material and the diffuse medium, usually based on the assumption of a tissue-air interface even though that does not accurately represent the tissue-applicator interface. In this study the A value must be experimentally determined in order to assure the accuracy of model-data examination.

The determination of the A value involved two steps. In the first step the same set of isotropic diffuser source and detector as that used for the studies in Section 3.3.3 were immerged in the same 0.5% Intralipid solution to form an infinite-medium geometry. The measurement of photon diffusion in this infinite-medium geometry was specified by the well-known formula of

$$\ln(\Psi \cdot d) = -\sqrt{\frac{\mu_a}{D}}d + \ln\left(\frac{S}{4\pi D}\right) \tag{3.3.1}$$

where d is the source-detector distance. The source term $S/4\pi D$ or the intercept term $\ln(S/4\pi D)$ was found by fitting the experimental data to the linear relationship between $\ln(\Psi \cdot d)$ and d. In the second step a semi-infinite geometry was constructed using a large plate of black acetal which was materially the same as that used for the studies in Section 3.3.3. The measurement of photon diffusion in this semi-infinite medium geometry was specified by the formulas (Fantini et al., 1994) of

$$\Psi = \frac{S}{4\pi D l_{real}} e^{-k_0 l_{real}} - \frac{S}{4\pi D l_{imag}} e^{-k_0 l_{imag}} \tag{3.3.2}$$

where

$$l_{real} = \sqrt{d^2 + R_a^2}\,, \qquad R_a = 1/\mu_s' \tag{3.3.3}$$

$$l_{imag} = \sqrt{d^2 + (2R_b + R_a)^2}\,, \qquad R_b = 2AD \tag{3.3.4}$$

By substituting the value of $S/4\pi D$ obtained from Eq. (3.3.1) into Eq. (3.3.2) and fitting the experimental data Ψ to different A values, the A value was determined as 1.86 after averaging four sets of measurements (A = 1.897, 1.806, 1.905, 1.814).

3.4 Analysis of the measurement error associated with inaccurate positioning of the source and detector

3.4.1 Effect of the radial positioning errors of the source and the detector

In the analytic solutions both the source and the detector are assumed as infinitesimally small whereas the isotropic source and detector used in the experiments had finite sizes, specifically spherical tips with diameters of 2*mm* and 1.59*mm*, respectively. In all the experimental setups except the one shown in Fig. 26(a), the source and detector fibers were firstly fixed in stainless tubes which were then fixed onto the positioning stages. Thus the detector might not have been located precisely on the surface of the applicator, and the source might not have been positioned precisely $1/\mu_s'$ from the surface of the applicator. To model how much the measurement could be affected due to the positioning error, Eqs. (3.2.1conC) and (3.2.1conV) are rewritten to

$$\Psi = \frac{S}{2\pi^2 D}\int_0^\infty dk\left\{\cos\left[k(z-z')\right]\sum_{m=0}^{\infty}\varepsilon_m I_m\left(k_{eff}\rho_{r<}\right)K_m\left(k_{eff}\rho_{r>}\right)\right.$$
$$\left.\cdot\left\langle 1-\frac{I_m\left(k_{eff}\rho_{r>}\right)}{K_m\left(k_{eff}\rho_{r>}\right)}\frac{K_m\left[k_{eff}\left(R_0+R_b\right)\right]}{I_m\left[k_{eff}\left(R_0+R_b\right)\right]}\right\rangle\cos\left[m(\varphi-\varphi')\right]\right\} \qquad (3.4.1\text{conC})$$

$$\Psi = \frac{S}{2\pi^2 D}\int_0^\infty dk\left\{\cos\left[k(z-z')\right]\sum_{m=0}^{\infty}\varepsilon_m I_m\left(k_{eff}\rho_{r<}\right)K_m\left(k_{eff}\rho_{r>}\right)\right.$$
$$\left.\cdot\left\langle 1-\frac{K_m\left(k_{eff}\rho_{r<}\right)}{I_m\left(k_{eff}\rho_{r<}\right)}\frac{I_m\left[k_{eff}\left(R_0-R_b\right)\right]}{K_m\left[k_{eff}\left(R_0-R_b\right)\right]}\right\rangle\cos\left[m(\varphi-\varphi')\right]\right\} \qquad (3.4.1\text{conV})$$

where $\rho_{r<}$ and $\rho_{r>}$ indicate the smaller and larger radial coordinates of the source and the detector. For the "concave" geometry $\rho_{r<} = R_0 - R_a$ and $\rho_{r>} = R_0$; for the "convex" geometry, $\rho_{r<} = R_0$ and $\rho_{r>} = R_0 + R_a$ (Zhang at el., 2010). When there is positioning error for the source

or the detector in the azimuth plane, the $\rho_{r<}$ and $\rho_{r>}$ for the "concave" geometry and "convex" geometry can be expressed respectively as

$$\rho_{r<} = R_0 - R_a - \xi\big|_{source}\,, \qquad \rho_{r>} = R_0 - \xi\big|_{detector} \qquad \text{(3.4.2conC)}$$

$$\rho_{r<} = R_0 + \xi\big|_{detector}\,, \qquad \rho_{r>} = R_0 + R_a + \xi\big|_{source} \qquad \text{(3.4.2conV)}$$

where $\xi\big|_{subscript}$ denotes the shift of the position of the *subscript* from the intended location in the azimuth plane. The details of $\rho_{r<}$ and $\rho_{r>}$ in the azimuth plane are shown in Fig. 27(a) and (b) for "concave" and "convex" geometries, respectively. By using the notations $\rho_{r<}$ and $\rho_{r>}$ defined in Eq. (3.4.2), Eqs. (3.2.2conC) and (3.2.2conV) for the *case-azi* configuration can be converted to

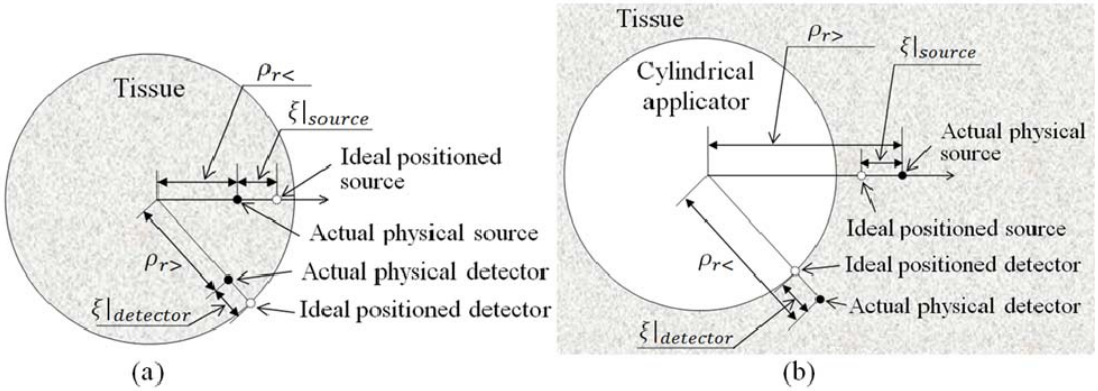

Fig. 27 Details of $\rho_{r<}$ and $\rho_{r>}$ in the azimuth plane: (a) "concave" geometry: (b) "convex" geometry.

$$\Psi = \frac{S}{2\pi^2 D}\int_0^\infty dk\left\{\sum_{m=0}^{\infty}\varepsilon_m I_m\left(k_{eff}\rho_{r<}\right)K_m\left(k_{eff}\rho_{r>}\right)\left\langle 1-\frac{I_m\left(k_{eff}\rho_{r>}\right)}{K_m\left(k_{eff}\rho_{r>}\right)}\frac{K_m\left[k_{eff}\left(R_0+R_b\right)\right]}{I_m\left[k_{eff}\left(R_0+R_b\right)\right]}\right\rangle\cos\left[m(\varphi-\varphi')\right]\right\}$$

(3.4.3conC)

$$\Psi = \frac{S}{2\pi^2 D}\int_0^\infty dk\left\{\sum_{m=0}^{\infty}\varepsilon_m I_m\left(k_{eff}\rho_{r<}\right)K_m\left(k_{eff}\rho_{r>}\right)\left\langle 1-\frac{K_m\left(k_{eff}\rho_{r<}\right)}{I_m\left(k_{eff}\rho_{r<}\right)}\frac{I_m\left[k_{eff}\left(R_0-R_b\right)\right]}{K_m\left[k_{eff}\left(R_0-R_b\right)\right]}\right\rangle\cos\left[m\left(\varphi-\varphi'\right)\right]\right\}$$

(3.4.3conV)

and Eqs. (3.2.3conC), (3.2.3conV) for the *case-longi* configuration can be converted to

$$\Psi = \frac{S}{2\pi^2 D}\int_0^\infty dk\left\{\cos\left[k\left(z-z'\right)\right]\sum_{m=0}^{\infty}\varepsilon_m I_m\left(k_{eff}\rho_{r<}\right)K_m\left(k_{eff}\rho_{r>}\right)\left\langle 1-\frac{I_m\left(k_{eff}\rho_{r>}\right)}{K_m\left(k_{eff}\rho_{r>}\right)}\frac{K_m\left[k_{eff}\left(R_0+R_b\right)\right]}{I_m\left[k_{eff}\left(R_0+R_b\right)\right]}\right\rangle\right\}$$

(3.4.4conC)

$$\Psi = \frac{S}{2\pi^2 D}\int_0^\infty dk\left\{\cos\left[k\left(z-z'\right)\right]\sum_{m=0}^{\infty}\varepsilon_m I_m\left(k_{eff}\rho_{r<}\right)K_m\left(k_{eff}\rho_{r>}\right)\left\langle 1-\frac{K_m\left(k_{eff}\rho_{r<}\right)}{I_m\left(k_{eff}\rho_{r<}\right)}\frac{I_m\left[k_{eff}\left(R_0-R_b\right)\right]}{K_m\left[k_{eff}\left(R_0-R_b\right)\right]}\right\rangle\right\}$$

(3.4.4conV)

Equations (3.4.3conC), (3.4.3conV) and (3.4.4conC), (3.4.4conV) were numerically implemented, by letting $\xi\big|_{detector}$ changing from 0 to 1*mm* and $\xi\big|_{source}$ changing from -0.5*mm* to 0.5*mm*, to assess the effect of the positioning errors of the source and the detector in the azimuth plane within 1*mm*, based on the set of parameters including $\mu_a = 0.025cm^{-1}$, $\mu_s' = 5cm^{-1}$, $A = 1.86$, and $S = 1$. The "concave" geometry dimensions being evaluated had the radii of 0.95*cm* and 2.53*cm*, and the "convex" geometry dimensions being evaluated had the radii of 1.27*cm*, 2.41*cm* and 5.07*cm*, respectively, as those studies in Section 3.3. The results for the *case-azi* configuration are shown in Fig. 28. Figure 28(a) presents the results for the source fixed but the detector shifted radially on the same azimuth plane by 0*mm*, 0.5*mm* and 1*mm* respectively. Figure 28(b) presents the results for the detector fixed but the source shifted radially on the same azimuth plane by -0.5*mm*, 0*mm* and 0.5*mm*. For the evaluations in Fig. 28, the longitudinal positioning of the source and the detector has been assumed accurate. It is indicated from Fig. 28(a) and (b) that for source-detector distances greater than approximately five times of the transport mean free path length ($\geq 5/\mu_s' = 1cm$ in this case), the 1*mm* radial positioning error of source and detector in the azimuth plane would have negligible effect upon the measurement of photon fluence.

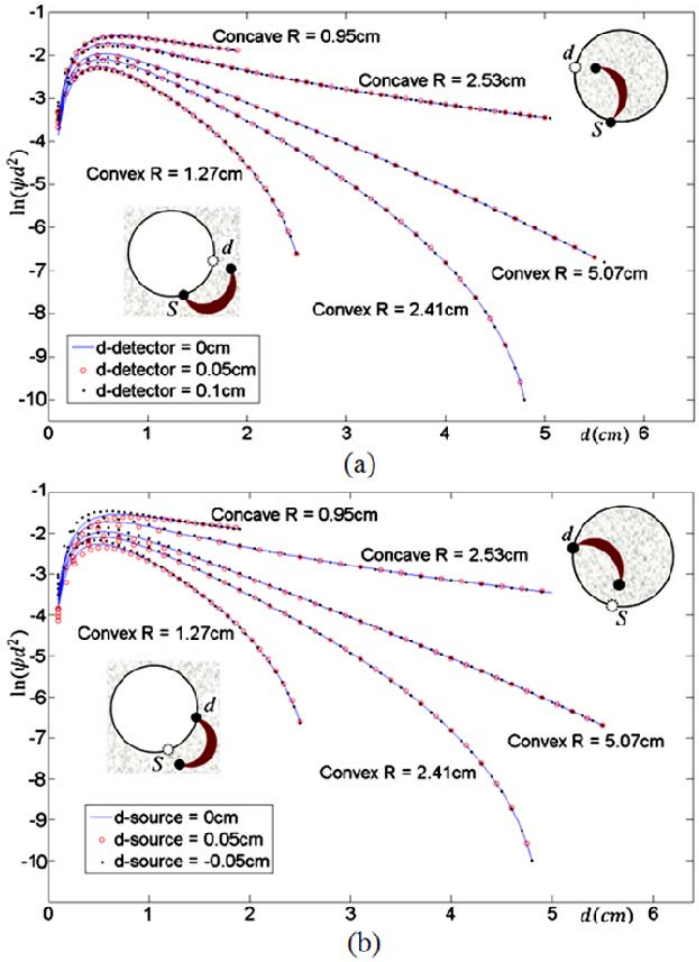

Fig. 28 The effect of positioning error of source or detector in *case-azi* configurations: (a) the source is fixed but the detector is shifted radially by 0*mm*, 0.5*mm* and 1*mm* respectively: (b) the detector is fixed but the source is shifted radially by -0.5*mm*, 0*mm* and 0.5*mm* respectively. The conditions for (a) are (b) are not identical due to the requirement of an isotropic source placed $1/\mu_s'$ distance into the medium whereas the detector is ideally located on the surface.

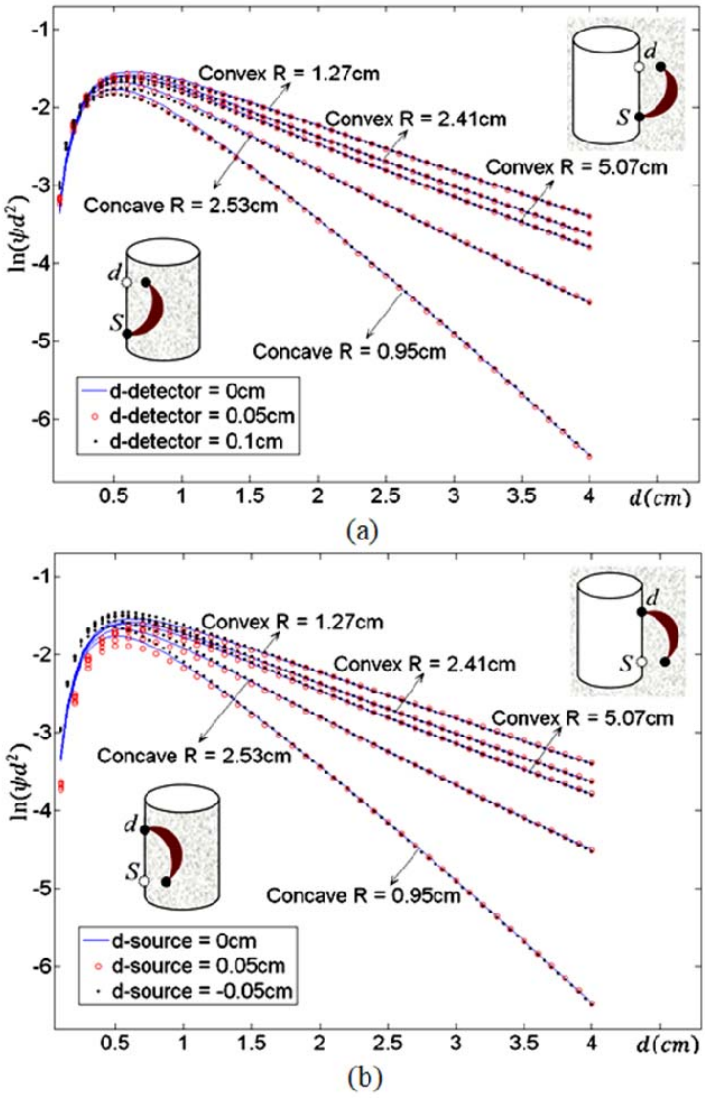

Fig. 29 The effect of positioning error of source or detector in *case-longi* configurations: (a) the source is fixed but the detector is shifted radially by 0*mm*, 0.5*mm* and 1*mm* respectively. (b) the detector is fixed but the source is shifted radially by -0.5*mm*, 0*mm* and 0.5*mm* respectively. The conditions for (a) are (b) are not identical due to the requirement of an isotropic source placed $1/\mu_s'$ distance into the medium whereas the detector is ideally located on the surface.

The results for the *case-longi* configuration are shown in Fig. 29. Figure 29(a) is for the source fixed but the detector shifted radially on the same azimuth plane by 0*mm*, 0.5*mm* and 1*mm* respectively. Figure 29(b) is for the detector fixed but the source shifted radially on the same azimuth plane by -0.5*mm*, 0*mm* and 0.5*mm* respectively. For the evaluations in Fig. 29, the longitudinal positioning of the source and the detector has been assumed accurate. Figure 29(a) and (b) again indicate that the 1*mm* radial positioning error of source and detector has negligible effect to the measurements of photon fluence when the source-detector distance is greater than approximately 5 transport mean free path lengths ($\geq 5/\mu_s'$). Based on Fig. 28 and 29, it was expected that the experimental measurement in the diffusion regime of the given setup should be insensitive to small inaccuracy of the radial positions of the source and the detector.

3.4.2 Effect of the initial error of the source-detector distance

In the analytical evaluation, the source-detector distance is precisely determined. In the experimental measurement, either the source or the detector was fixed, and the other was translated continuously starting from an initial value of source-detector distance that was subjected to an error. The effect due to the error of this initial measurement of source-detector distance is investigated in Fig. 30(a) and (b). The evaluations are similar to those in Fig. 28 and 29, with the changes being made from varying the radial position of source or detector to instead increasing or decreasing the initial source-detector distances respectively by 0.5*mm*, 1*mm* and 2*mm*.

The curves shown in Fig. 30(a) and (b) have been shifted vertically with respect to the one with the defined initial distance to give more direct comparisons. It is indicated from Fig. 30 that for both the *case-azi* and *case-longi* configurations, the effect of the error of the initial source-detector distance resembles changing the radius of the cylindrical applicator as demonstrated in

Fig. 17 for the *case-azi* and Fig. 20 for the *case-longi* configurations in Chapter II. This agrees with the expectation that the measurement of the photon fluence decay will be sensitive to the initial source-detector distance, but it also implies that experimental measurements with an uncertainty of the initial source-detector distance is justifiable using analytical predictions by slightly varying the radius parameter in the computation.

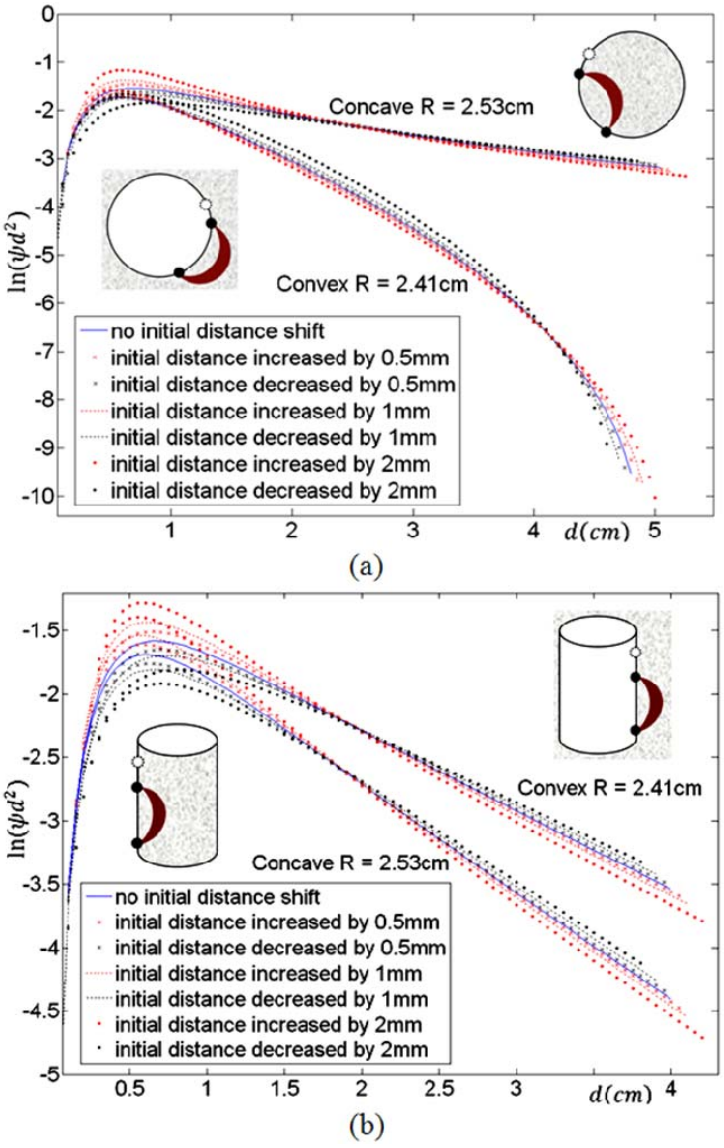

Fig. 30 The effect of the measurement error of the initial source-detector distance. The initial source-detector distance is changed +0.5*mm*, -0.5*mm*, +1*mm*, -1*mm*, +2*mm* and -2*mm*, respectively, for (a) *case-azi* configuration and (b) *case-longi* configuration.

3.5 Results of quantitative examination

This section compares the analytic predictions made for the *case-azi* and *case-longi* configurations with respect to the results obtained from FEM, MC, and experimental examinations. The differences in the source-intensity settings in all of these quantitative measurements were compensated by a vertical shift for each of them in Fig. 31 presented below in order for the analytic predictions to compare with. The results for the *case-azi* configuration are given in Fig. 31(a). The shortest source-detector distance implemented in the analytic predictions, FEM and MC simulations were seen as at or below $0.1cm$, but that in the experimental examinations had been at approximately $1cm$. This was due to the consideration of maximizing the measurement consistency, because each set of data corresponding to the available range of source-detector distance was acquired by setting the source power and CCD gain as fixed, rather than as variable to only accommodate a larger dynamic range. As indicated previously, the measurement of the initial source-detector distance was subjected to an error due to the spherical diffuser tips as well as other experimental limitations, but the error was controlled to be within $0.9mm$ for the *case-azi* and $0.5mm$ for the *case-longi* configurations, respectively.

The decay rate of photon fluence for the *case-azi* configuration made by analytic predictions was compared with those by FEM, MC, and experimental examinations in Fig. 31(a). The data are plotted for $\ln(\psi d^2)$ as a function of d to verify the different trends of photon fluence decay expected for the "concave" and "convex" geometries, with respect to that for a semi-infinite medium which is largely linear over the entire range of source-detector distance. It was predicted analytically that the decay rate of photon fluence of the *case-azi* configuration in "concave" geometry would be smaller than that in the semi-infinite medium, which was expected as the decreasing magnitude of the curve's slope toward longer source-detector distance, e.g. the curve becoming upward bended. It had also been predicted analytically that the decay rate of photon fluence of the *case-azi* configuration in "convex" geometry would be greater than that in

the semi-infinite medium, which was expected as the increasing magnitude of the curve's slope toward longer source-detector distance, e.g. the curve becoming downward bended.

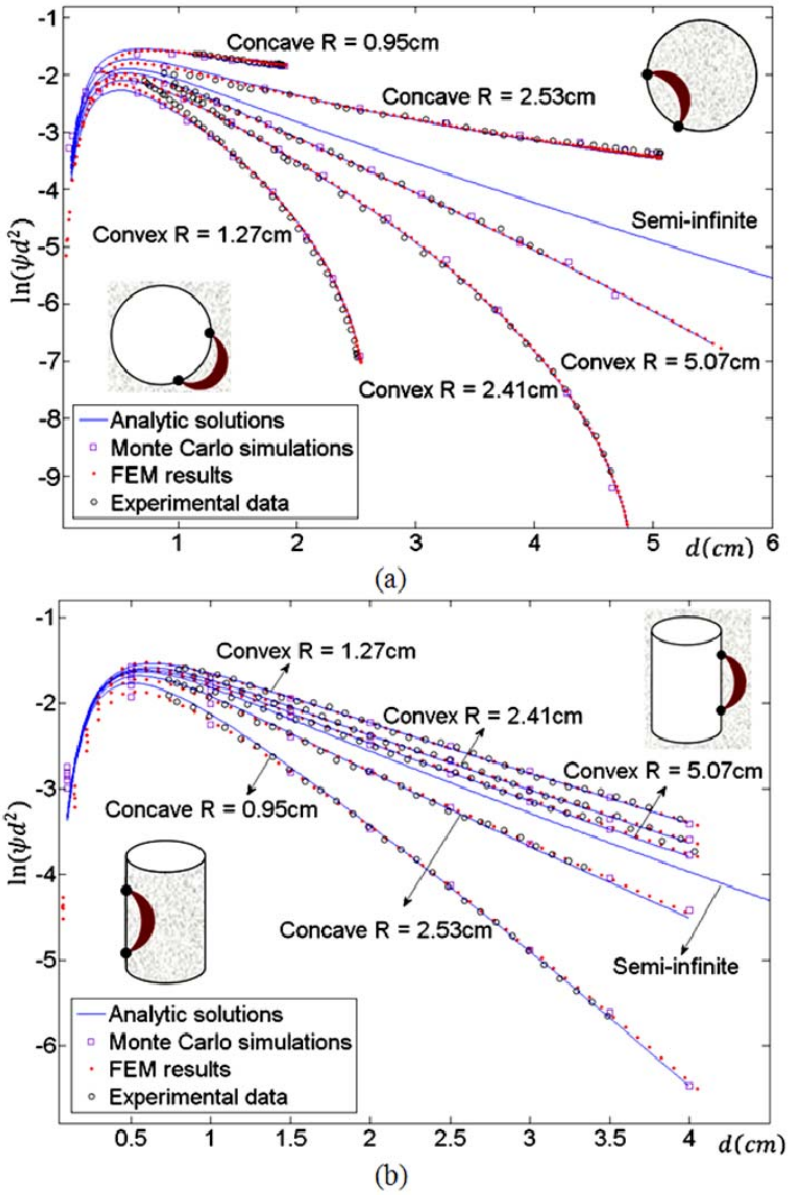

Fig. 31 The comparisons of analytic prediction, FEM simulation, MC simulation, and experimental results for both "concave" and "convex" geometries: (a) *case-azi* configuration; (b) *case-longi* configuration. The optical properties are $\mu_a = 0.025cm^{-1}$, $\mu_s' = 5cm^{-1}$, $A = 1.86$, and $S = 1$.

For the *case-azi* configurations of "concave" geometry and "convex" geometry that have the same radius parameter, it has also been predicted that the deviation of the "upward-bending" curve of "concave" geometry from the semi-infinite line (e.g. the magnitude of the slope difference between them) is smaller than that of the "downward-bending" curve of "convex" geometry from the semi-infinite line. The comparison for the decay rate of photon fluence for the *case-longi* configuration is shown in Fig. 31(b). Contrary to that in the *case-azi* configuration, in the "concave" geometry the decay rate of photon fluence is larger than that in the semi-infinite medium, and in the "convex" geometry the decay rate of photon fluence is smaller than that in the semi-infinite medium. However, for both the "concave" and "convex" geometries, the slope of the curve in either "concave" or "convex" geometry tends to be largely constant, with the slope of "concave" geometry greater in magnitude than that of semi-infinite medium and the slope of "convex" geometry smaller in magnitude than that of semi-infinite medium.

It was observed that the analytical, FEM, MC, and experimental measurements agree with each other qualitatively, in terms of the pattern of deviation from the semi-infinite geometry, for the entire range of source-detector distances investigated for both *case-azi* and *case-longi* configurations. For source-detector distances greater than approximately five times of the transport mean free path, the results from the four methods agree quantitatively with each other.

3.6 Discussions

Numerous studies have demonstrated that the assumption of a spherically isotropic source in the diffusion model accurately reflects experimental data when the source is centered one transport scattering distance within the medium from the boundary. This type of "equivalent" representation of a directional source by an inwardly-displaced isotropic source can well quantify the fluence rate at distances greater than 3–5 transport scattering lengths from the source (Farrell

et al., 1992). The agreement shown in this work among the four methods, for a considerable range of source-detector separations as long as they are greater than approximately 5 transport scattering lengths, is again supportive of the "diffusion" treatment of directional source using a spherically isotropic source placed one transport scattering distance into the medium, even for concave or convex geometries with considerably small radius. At sub-diffusion regime, a disagreement is expected between diffusion model and experimental result which in this work has been carried out by MC simulation as physical measurement for the given geometries became impractical at source-detector distances shorter than approximately 5 transport scattering lengths. Between the diffusion based analytical quantification and FEM simulation for sub-diffusion regime, however, the analytical result is slightly closer to the MC results than the FEM simulation is. This is largely due to the fact that for the given spatial dimension the spatial impulse source employed in the analytical solution is physically analogous to the launching of strictly forward-directional photons at a single point in MC simulation, whereas the size-effect of the spatially distributed Gaussian source profile implemented in FEM is manifested at shorter distances from the source. Besides, our treatment of boundary effect, e.g. the probability of boundary-reaching photon returning to the medium, in the MC simulation was based on the experimental measurements by use of "extrapolated" boundary condition as in the analytical model, whereas a Robin-type boundary condition was used by the FEM. The subtle difference in the boundary conditions could have been amplified at sub-diffusion regime.

The analytic model investigated in Chapter II and utilized in this chapter assumes that the cylindrical applicator is infinitely long whereas the one tested in our experiments has finite-length. For the *case-azi* configurations shown in Fig. 31(a), all experimental measurements have been confined in an azimuth plane that is several centimeters away from the edge of the applicator. The results in Fig. 31(a) show no noticeable edge-effect which is specified as the degree of the model-data mismatch being proportional to the radius of the applicator. For the *case-longi* configuration shown in Fig. 31(b), either the source or the detector has been translated 4*cm* from the middle of

the applicator toward the edge, and the edge effect may be perceived as slightly larger deviation of the experimental data from the analytical predictions for larger applicator radius that gives smaller length-to-radius ratio. The effect of the finite-length of the applicator may be accounted for by considering the effects of two additional "image sources" of the physical source, with respect to the two longitudinal boundary-facets, or modeled rigorously by deriving the Green's function specific to the geometry of finite cylindrical applicator. In fact, Liemart et al (Liemert et al., 2010) has had extensive analysis of photon diffusion in finite "concave" cylindrical applicator geometry for time-domain and frequency-domain measurements. Their derivation of the Green's function for the time-domain or frequency-domain photon diffusion in the finite "concave" geometry used the cosine transform and Hankel transform, which can be readily extended to finite "convex" applicator geometry to understand time-domain or frequency-domain photon diffusion in a geometry similar to that investigated in our experiments. Our analytic approach in Chapter II has been for the steady-state photon diffusion only by expanding the Green's function in Fourier series and Fourier transform; however, our approach provides the first insights for the models of photon diffusion in both "concave" and "convex" geometries. The analytic treatment in Chapter II involved a real k in the solution of steady-state photon diffusion. By implementing a complex k in the analytic process, the approach may be extended to frequency domain analysis for both "concave" and "convex" geometries, which will be further discussed in Chapter V, but for time-domain analysis, the method of Liemart et al. may be the method to follow. The approaches by Liemart et al. and that demonstrated in (Zhang et al., 2010) are complimentary, and when combined may render analytic solutions to more geometries and measurement conditions.

Our unified modeling of both "concave" and "convex" geometries has given the opportunity of observing some previously less-known patterns of photon diffusion associated with cylindrical applicator. Fig. 31 verified that for the specific case of having the source and detector located azimuthally on the same axial plane, the decay rate of photon fluence is smaller

in the “concave” geometry and greater in the “convex” geometry, respectively, than that in the semi-infinite geometry for the same source-detector distance. For the specific case of having the source and detector located longitudinally with the same azimuth angle, the decay rate of photon fluence is greater in the “concave” geometry and smaller in the “convex” geometry, respectively, than that in the semi-infinite geometry for the same source-detector distance. These interesting findings imply the existence of a potentially “spiral” direction on the surface of both the concave cylindrical applicator and the convex cylindrical applicator, along which the decay rate of photon fluence could be equivalent to that in a planar surface or a semi-infinite geometry. This interesting phenomenon of photon diffusion that may associate with a cylindrical applicator is predicted as “spiral-planar equivalence”. If the existence of such a “planar-equivalent” spiral direction inside or outside a cylindrical applicator is verified, for certain trans-lumenal sensing or imaging applications the semi-infinite geometry may be implemented for greatly simplified modeling and rapid recovery of tissue optical properties. The next chapter discusses such “spiral-planar equivalence” phenomenon.

3.7 Conclusion

Chapter II analytically examined the steady-state photon diffusion along the azimuth direction or the *case-azi* configuration and the longitudinal direction or *case-longi* configuration, in the infinitely long “concave” and “convex” applicator geometries. This chpater quantitatively examined the predictions of Chapter II for the *case-azi* configuration that the decay rate of photon fluence would become smaller in the “concave” geometry and greater in the “convex” geometry, respectively, than that in the semi-infinite geometry for the same source–detector distance. This chapter also examined predictions of Chapter II for the *case-longi* configuration which suggested that the decay rate of photon fluence would be greater in the “concave” geometry and smaller in

the “convex” geometry, respectively, than that in the semi-infinite geometry for the same source–detector distance. The results of three quantitative examination approaches including (a) finite-element-method (FEM), (b) Monte Carlo (MC) simulation, and (c) experimental measurement on finite cylindrical-applicator geometries with large length-to-radius ratio validated the qualitative trend predicted in Chapter II and verified the quantitative accuracy of the analytic treatment presented in Chapter II in the diffusion regime of the measurement, at a given set of absorption and reduced scattering coefficients of the medium.

CHAPTER IV

UNIQUE SPIRAL PATHS IN STEADY-STATE TRANS-LUMINAL PHOTON DIFFUSION

4.1 Introduction (Zhang A, Piao D et al., 2011; Zhang A, Piao D, Bunting CF et al., 2012)

The theory of diffuse photon propagation (Ishimaru et al., 1989) is the basis of a number of bio-optical imaging approaches, including optical spectroscopy and optical tomography, which are extensively used for interrogating functional status of tissue volumes in the diffusion regime. Diffuse optical techniques are most conveniently employed as a non-invasive imaging modality, which inevitably involves a physical interface between the tissue and the imaging applicator or in some cases the air. Most of these interfaces are in the form of either a planar shape, to which the semi-infinite geometry fits well, or a curved "concave" surface of a relatively large radius with the center of the curvature located at the same side of the medium to be imaged, which is modeled quite accurately as a semi-infinite boundary. A recent study of diffuse optical imaging involved deploying the applicator in a body cavity (Piao et al., 2006). The tissue-applicator interface in that study, which differs significantly from a semi-infinite geometry, was rendered by a "convex" curvature of small radius with the center of the curvature located opposite to the tissue to be imaged. In diffuse optical tomography arbitrary surfaces are detailed by means of numerical tools such as finite element method (FEM) (Arridge et al., 1993), therefore the effects of the shape and size of a tissue-applicator interface are accurately accounted for in the forward computation, even for the applicator of small radius as long as the diffusion regime is concerned. On the other hand, in many diffuse optical sensing or spectroscopy applications the quantization of tissue optical properties is essentially based upon an analytic model specific to the studied geometry, of which a planar semi-infinite model is frequently implemented.

For a medium enclosed by a cylindrical boundary, several studies, including an extensive early work by Arridge et al. (Arridge et al., 1992) and a recent one by Liemert et al. (Liemert et al., 2010), have established the theoretical frameworks for modeling photon diffusion in such concave-shaped geometry. Using the general analytic results introduced in those featured works, one could calculate the diffuse photon remission along any directions on the concave-interface, including two orthogonal directions, namely the longitudinal and the azimuth directions. A pictorial examination of such "concave" interfaces would reveal that, for the same line-of-sight distance between the source and the field/detector positions, the diffuse photon remission along the azimuth direction should be *greater* than that on the semi-infinite interface, and conversely for that along the longitudinal direction. Furthermore, as the radius of the concave interface reaches infinity, the diffuse photon remission along either azimuth or longitudinal direction shall progress asymptotically to that along a straight-line on a semi-infinite interface. Such salient features relative to the concave-interfaced geometry have been examined for steady-state photon remission in a new analytical study in Chapter II of this thesis and validated by quantitative methods including FEM solution of photon diffusion equation, Monte-Carlo (MC) simulation, and experiment in Chapter III of this thesis. The studies in Chapter II and Chapter III have also examined the convex-interfaced geometry. In the convex-interfaced geometry the diffuse photon remissions along the longitudinal and the azimuth directions are found to be the opposite to those in concave-interfaced geometry when comparing to that along a straight-line in a semi-infinite geometry given the same line-of-sight source-detector distance, and as the radius of the interface reaches infinity both remissions progress asymptotically to that along a straight line on the semi-infinite geometry. If the radius of the concave or convex interface becomes considerably small, e.g. a couple of centimeters, the diffuse photon remissions along the longitudinal and the azimuth directions deviate significantly from that along a straight-line on the semi-infinite interface. Such deviation entails curvature-specific and radius-specific modeling of the photon diffusion in the associated geometries.

In this chapter, we demonstrate an interesting phenomenon of diffuse photon remission associated with a long concave or convex cylindrical applicator. It refers to the plausibility that for a long concave or convex cylindrical applicator a unique set of spiral paths exists on the tissue-applicator interface, along which the diffuse photon remission is essentially modeled by that along a straight line on a semi-infinite interface, given the same line-of-sight source-detector distance. Section 4.2 details the approach leading to the analytic representation of the spiral paths for concave and convex geometries of large radius with homogeneous-medium conditions. Section 4.3 presents the numerical approach used to find the spiral paths for concave and convex geometries of smaller radius with homogeneous-medium conditions. Section 4.4 provides the FEM and Monte Carlo simulations, examining the photo diffusion along the defined spiral profile identified in Section 4.3. Section 4.5 employs the Born approximation to analyze the perturbation introduced to the photon fluence rate by a single heterogeneity with contrast in absorption and reduced scattering coefficient. Section 4.6 implements numerically the analytic results from Section 4 to the case of single heterogeneity with weak perturbation strength, to examine the photon fluence rate along the spiral paths identified for the otherwise homogeneous medium. Section 4.7 quantifies the effect of single heterogeneity of strong perturbation strength to the photon fluence rate along the spiral paths identified for the otherwise homogeneous medium, by the use of FEM. Both Sections 4.6 and 4.7 limits the evaluations to the case of single heterogeneity aligned azimuthally with the spiral paths; however, four cases of the contrast of the heterogeneity are considered: (1) positive absorption contrast, (2) negative absorption contrast, (3) positive reduced scattering contrast, and (4) negative reduced scattering contrast. Section 4.8 discusses the dependence of the spiral paths upon the optical properties of the homogeneous medium as well as the radial dimension of the concave or convex geometry.

4.2. Spiral paths associated with concave and convex geometries of large radii

The general case of a source and a detector located on the tissue-applicator interface is illustrated in Fig. 32(A) and (B), for ***concave*** and ***convex*** geometries, respectively. The tissue enclosed by the interface in the ***concave*** geometry or enclosing the interface in the ***convex***

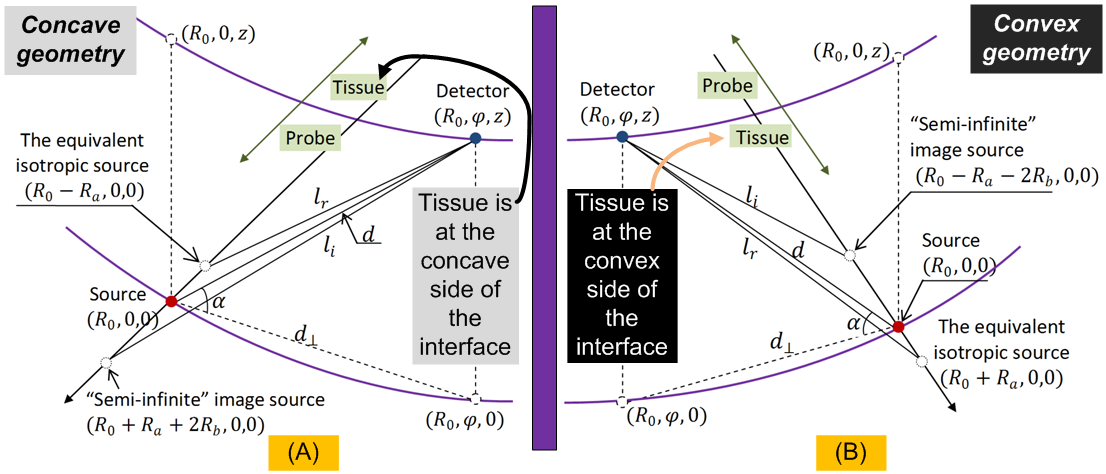

Fig. 32 Notations and physical entities of concave or convex geometry for analytic evaluation of photon fluence rate associated with larger radius. (A) The tissue is at the concave side of the circular cylindrical tissue-applicator interface, so the equivalent isotropic source of the physical source that illuminates into the medium is located closer to the center axis than the physical source is. (B) The tissue is at the convex side of the circular cylindrical tissue-applicator interface, so the equivalent isotropic source of the physical source that illuminates into the medium is located farther from the center axis than the physical source is.

geometry has an absorption coefficient μ_a, a reduced scattering coefficient μ_s', a diffusion coefficient *D,* and an effective attenuation coefficient $k_0 = \sqrt{\mu_a / D}$. The radius of the infinitely long circular cylindrical interface is R_0, therefore by cylindrical coordinates, the source with an intensity of *S* locates at (R_0, 0, 0) and the detector locates at (R_0, φ, z). The line-of-sight distance between the source (R_0, 0, 0) and the detector (R_0, φ, z) is denoted by *d*. The projection of *d* to the azimuthal plane or the projection of *d* perpendicular to the longitudinal axis of the cylindrical interface is denoted as $d_\perp = d \cdot \cos\alpha$, where α is the angle between *d* and $d_\perp$. The position of the detector with respect to the source can then be represented by $(\alpha, d_\perp)$. If keeping the source fixed at (R_0, 0, 0) and increasing the radius R_0, the detector will eventually reach a plane that is tangential to the shown cylindrical interface and intersects with the interface at the longitudinal line crossing the source (R_0, 0, 0). Such a plane forms the "semi-infinite geometry" limit of the ***concave*** or ***convex*** geometry.

4.2.1 Analytic representation of the spiral-paths associated with concave geometry of large radii

Consider the ***concave*** geometry shown in Fig. 32(A). The source illuminating into the tissue at (R_0, 0, 0) can be represented by an isotropic source at (R_0-R_a, 0, 0), where $R_a = 1/\mu_s'$. An extrapolated boundary in the imaginary "semi-infinite geometry" will be placed at $R_b = 2AD$, where A is a parameter determined by the refractive index mismatch across the tissue-applicator interface, outward from the source (R_0, 0, 0). For the equivalent isotropic source at (R_0-R_a, 0, 0), its image source with respect to the extrapolated boundary of the imaginary "semi-infinite geometry" locates at (R_0+Ra+2R_b, 0, 0).

Denote l_r as the distance from the detector (R_0, φ, z) to the equivalent "real" isotropic source at (R_0-R_a, 0, 0), and l_i as the distance from the detector (R_0, φ, z) to the "image" source

(R_0+Ra+2R_b, 0, 0) associated with the imaginary semi-infinite geometry. For R_0>>d>>R_a, R_b, the photon fluence rate at the detector position can be expressed by as in Chapter II

$$\Psi = \frac{S}{4\pi D}\frac{e^{-k_0 l_r}}{l_r} - \frac{S}{4\pi D}\frac{e^{-k_0 l_i}}{l_i}\sqrt{\frac{R_0 + R_a + 2R_b}{R_0 - R_a}} \tag{4.2.1}$$

and we have

$$l_r = d\sqrt{\left[1 + \frac{R_a^2}{d^2} - \frac{R_a}{R_0}(\cos\alpha)^2\right]} \tag{4.2.2}$$

$$l_i = d\sqrt{\left[1 + \frac{(R_a + 2R_b)^2}{d^2} + \frac{R_a + 2R_b}{R_0}(\cos\alpha)^2\right]} \tag{4.2.3}$$

Since

$$\sqrt{\frac{R_0 + R_a + 2R_b}{R_0 - R_a}} = \left(1 + 2\frac{R_a + R_b}{R_0 - R_a}\right)^{1/2} \approx 1 + \frac{R_a + R_b}{R_0 - R_a} \tag{4.2.4}$$

and for d>>R_a, R_b one has $k_0 d >> 1$, so Taylor-series expansion gives

$$\frac{e^{-k_0 d\sqrt{1+\Delta}}}{d\sqrt{1+\Delta}} \approx \frac{e^{-k_0 d}}{d}\left[1 - \frac{1}{2}(k_0 d + 1)\Delta\right] \approx \frac{e^{-k_0 d}}{d}\left[1 - \frac{1}{2}(k_0 d)\Delta\right] \tag{4.2.5}$$

where Δ<<1. Using Eqs. (4.2.2) to (4.2.5), Eq. (4.2.1) simplifies to

$$\Psi = \frac{S}{4\pi D}\frac{e^{-k_0 d}}{d}\left\{\left[1 - \frac{1}{2}k_0 d\left(\frac{R_a^2}{d^2} - \frac{R_a}{R_0}(\cos\alpha)^2\right)\right]\right.$$
$$\left. - \left[1 - \frac{1}{2}k_0 d\left(\frac{(R_a + 2R_b)^2}{d^2} + \frac{R_a + 2R_b}{R_0}(\cos\alpha)^2\right)\right]\left(1 + \frac{R_a + R_b}{R_0 - R_a}\right)\right. \tag{4.2.6}$$

which can be further derived to the form of (the derivation is detailed in Appendix B)

$$\frac{\partial \ln(\Psi \cdot d^2)}{\partial d} = -\left\{k_0 + \frac{1}{2k_0 R_b(R_0 - R_a)} - \left[\frac{2R_0 - R_a + 2R_b}{2R_0 R_b(R_0 - R_a)}\right]\cos\alpha \cdot d_\perp\right\} \tag{4.2.7}$$

Equation (4.2.7) characterizes the decay-rate of photon fluence along the direction defined by angle α, with respect to the line-of-sight source-detector distance *d*. For *case-longi* configuration, the detector locates at (R_0, 0, z), so $\alpha = \pi/2$ and $d_\perp = 0$, then Eq. (4.2.7) becomes

$$\frac{\partial \ln\left(\Psi \cdot d^2\right)}{\partial d} = -\left[k_0 + \frac{1}{2k_0 R_b\left(R_0 - R_a\right)}\right] \tag{4.2.8}$$

For *case-azi* configuration, the detector locates at (R_0, φ, 0), so $\alpha = 0$ and $d_\perp = d$, then Eq. (4.2.7) becomes

$$\frac{\partial \ln\left(\Psi \cdot d^2\right)}{\partial d} = -\left\{k_0 + \frac{1}{2k_0 R_b\left(R_0 - R_a\right)} - \left[\frac{2R_0 - R_a + 2R_b}{2R_0 R_b\left(R_0 - R_a\right)}\right] d\right\} \tag{4.2.9}$$

The first term k_0 in the right hand-side of Eqs. (4.2.8) and (4.2.9) characterizes the decay-rate of photon fluence along a straight-line on a semi-infinite interface. It is clear by Eq. (4.2.8) that the photon fluence along the longitudinal direction in a ***concave*** geometry decays ***faster*** than the photon fluence along a straight-line in the semi-infinite geometry. However the decay-rate of photon fluence (comparing to k_0) along the azimuthal direction in a ***concave*** geometry as described by Eq. (4.2.9) is inexplicit due to the two terms of opposite signs after k_0. It can be shown that the 3rd term at the right-hand side of Eq. (4.2.9) is greater in magnitude than the 2nd term for general diffusion regime, therefore Eq. (4.2.9) actually accounts for the ***smaller*** decay-rate of photon fluence along the azimuthal direction in a ***concave*** geometry than that along a straight-line in the semi-infinite geometry.

From Eq. (4.2.7) it is straightforward to conclude that if the coordinates of the detector $\left(\alpha, d_\perp\right)$ with respect to the source satisfy the condition of

$$\cos\alpha = \frac{1}{k_0 d_\perp}\frac{R_0}{2R_0 - R_a + 2R_b} \tag{4.2.10}$$

then the decay-rate of photon fluence over the line-of-sight source-detector distance *d* in the ***concave*** geometry is identical to that over the same *d* in the semi-infinite geometry. Equation (4.2.10) implies that α changes as the detector displaces azimuthally away from the source.

4.2.2 Analytic representation of the spiral-paths associated with convex geometry of large radii

Consider the convex geometry shown in Fig. 32(B). A source illuminating into the tissue at (R_0, 0, 0) can be represented by an isotropic source at (R_0+R_a, 0, 0). An extrapolated boundary in the imaginary "semi-infinite geometry" will be placed at $R_b = 2AD$ inward from the source (R_0, 0, 0). For the equivalent isotropic source at (R_0+R_a, 0, 0), its image source with respect to the extrapolated boundary of the imaginary "semi-infinite geometry" locates at (R_0-Ra-2R_b, 0, 0).

Denote l_r as the distance from the detector (R_0, φ, z) to the equivalent "real" isotropic source at (R_0+R_a, 0, 0), and l_i as the distance from the detector (R_0, φ, z) to the "image" source (R_0-Ra-2R_b, 0, 0) associated with the imaginary semi-infinite geometry. For R_0>>d>>R_a, R_b, the photon fluence rate at the detector position can be expressed by as in Chapter II

$$\Psi = \frac{S}{4\pi D}\frac{e^{-k_0 l_r}}{l_r} - \frac{S}{4\pi D}\frac{e^{-k_0 l_i}}{l_i}\sqrt{\frac{R_0 - R_a - 2R_b}{R_0 + R_a}} \tag{4.2.11}$$

and we have

$$l_r = d\sqrt{\left[1 + \frac{R_a^2}{d^2} + \frac{R_a}{R_0}(\cos\alpha)^2\right]} \tag{4.2.12}$$

$$l_i = d\sqrt{\left[1 + \frac{(R_a + 2R_b)^2}{d^2} - \frac{R_a + 2R_b}{R_0}(\cos\alpha)^2\right]} \tag{4.2.13}$$

Since

$$\sqrt{\frac{R_0 - R_a - 2R_b}{R_0 + R_a}} = \left(1 - 2\frac{R_a + R_b}{R_0 + R_a}\right)^{1/2} \approx 1 - \frac{R_a + R_b}{R_0 + R_a} \tag{4.2.14}$$

Using Eqs. (4.2.12) to (4.2.14) and (4.1.15), Eq. (4.2.11) simplifies to

$$\Psi = \frac{S}{4\pi D}\frac{e^{-k_0 d}}{d}\left\{\left[1-\frac{1}{2}k_0 d\left(\frac{R_a^2}{d^2}+\frac{R_a}{R_0}(\cos\alpha)^2\right)\right]\right.$$

$$\left.-\left[1-\frac{1}{2}k_0 d\left(\frac{(R_a+2R_b)^2}{d^2}-\frac{R_a+2R_b}{R_0}(\cos\alpha)^2\right)\right]\left(1-\frac{R_a+R_b}{R_0+R_a}\right)\right\} \quad (4.2.15)$$

which can be further derived to the form of (the derivation is detailed in Appendix C)

$$\frac{\partial \ln(\Psi\cdot d^2)}{\partial d} = -\left\{k_0 - \frac{1}{2k_0R_b(R_0+R_a)} + \left[\frac{2R_0+R_a-2R_b}{2R_0R_b(R_0+R_a)}\right]\cos\alpha\cdot d_\perp\right\} \quad (4.2.16)$$

Equation (4.2.16) characterizes the decay-rate of photon fluence along the direction defined by angle α, with respect to the line-of-sight source-detector distance d. For *case-longi* configuration, the detector locates at (R_0, 0, z), so $\alpha = \pi/2$ and $d_\perp = 0$, then Eq. (4.2.16) becomes

$$\frac{\partial \ln(\Psi\cdot d^2)}{\partial d} = -\left[k_0 - \frac{1}{2k_0R_b(R_0+R_a)}\right] \quad (4.2.17)$$

For *case-azi* configuration, the detector locates at (R_0, φ, 0), so $\alpha = 0$ and $d_\perp = d$, then Eq, (4.2.16) becomes

$$\frac{\partial \ln(\Psi\cdot d^2)}{\partial d} = -\left\{k_0 - \frac{1}{2k_0R_b(R_0+R_a)} + \left[\frac{2R_0+R_a-2R_b}{2R_0R_b(R_0+R_a)}\right]d\right\} \quad (4.2.18)$$

The first term k_0 in the right hand-side of Eqs. (4.2.17) and (4.2.18) characterizes the decay-rate of photon fluence along a straight-line on a semi-infinite interface. It is clear by Eq. (4.2.17) that the photon fluence along the longitudinal direction in a ***convex*** geometry decays ***slower*** than the photon fluence along a straight-line in the semi-infinite geometry. However the decay-rate of photon fluence (comparing to k_0) along the azimuthal direction in a ***convex*** geometry described by Eq. (4.2.18) is inexplicit due to the two terms of opposite signs after k_0. It can be shown that the 3rd term at the right-hand-side of Eq. (4.2.18) is greater in magnitude than

the 2nd term for general diffusion regime, therefore Eq. (4.2.18) actually accounts for the greater decay-rate of photon fluence along the azimuthal direction in a ***convex*** geometry than that along a straight-line in the semi-infinite geometry.

From Eq. (4.2.16) it is straightforward to conclude that if the coordinates of the detector $(\alpha, d_\perp)$ with respect to the source satisfy the condition of

$$\cos\alpha = \frac{1}{k_0 d_\perp} \frac{R_0}{2R_0 + R_a - 2R_b} \tag{4.2.19}$$

then the decay-rate of photon fluence over line-of-sight source-detector distance *d* in the ***convex*** geometry is identical to that over the same *d* in the semi-infinite geometry. Equation (4.2.19) also implies that α changes as the detector is displaced azimuthally away from the source.

4.3 The spiral profile associated with small radius cylindrical applicator

The paths signified by Eqs. (4.2.10) and (4.2.19) for cylindrical geometries of large radius or more complex forms of such for cylindrical geometries of small radius are spirally-shaped and form a closed-loop. Figure 33 illustrates examples of those spiral paths for cylindrical geometries of small radius that are found numerically by a two-step procedure. In the calculation, the position of a detector or field point with respect to the source fixed at the origin is represented by a planar grid. The first step involves establishing a coarse grid consisting of identical rectangular elements of 0.05*cm* in length. As shown in Fig. 33(b), each grid represents three possible directions of moving a detector one step away from the source: 0.05*cm* along the longitudinal direction, 0.05*cm* in line-of-sight distance along the azimuth direction, or along a direction diagonal to the previous two. For each grid, the difference of photon fluences in the cylindrical geometry and the semi-infinite geometry is calculated, for the line-of-sight distance between the fixed source and each of the three possible positions of the detector. The detector is then moved

along the direction that has the least difference of the photon fluence from the semi-infinite geometry. The region containing the path for moving the detector, shown in Fig. 33(c), is then used as *a prior* in the second step to guide the calculation of a finer path as shown in Fig. 33(d), by using procedure similar to that in the first step but in a denser grid of 0.005*cm*, and only in the *prior* region. This two-step procedure is implemented for resolving a finer profile in an expedited computation workflow.

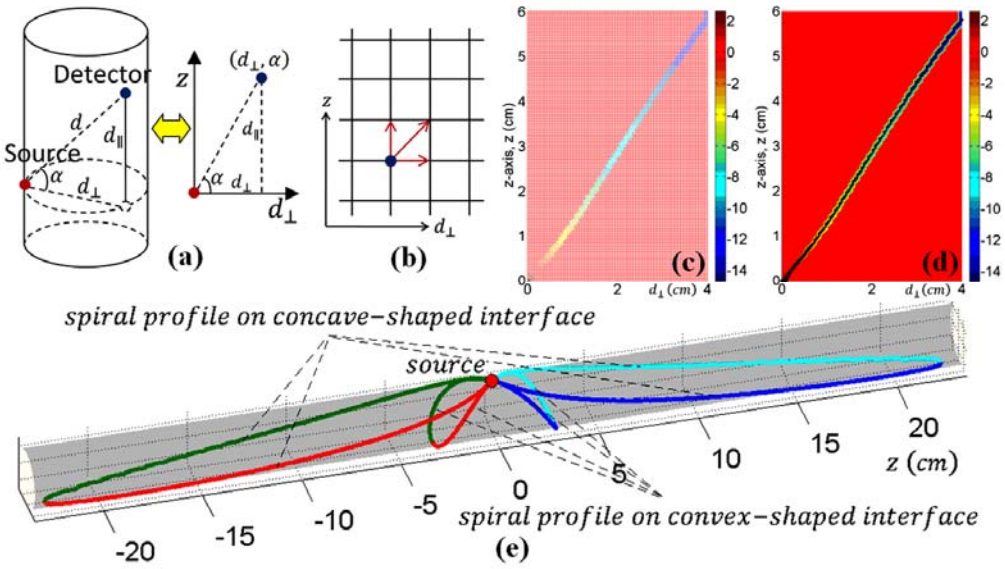

Fig. 33 (a) A source-detector pair on the cylindrical applicator's surface decomposes to a longitudinal distance and an azimuth distance. (b) The three options for moving the detector one step away from the source. (c) The region containing the path of moving the detector in a coarse grid. (d) The path of moving the detector in a dense grid using the region in (c) as a *prior*. (e) 3-D rendering of the spirally-shaped loops when the paths similar to that in (d) are mapped to the cylindrical interfaces of concave and convex geometries.

The nodes of the grid for positioning the detector following the steps described above, when mapped back onto the cylindrical interface, become the spirally-shaped loop presented in Fig. 33(e) for both concave and convex interfaces of the same radius. The complete profile of the butter-fly shaped spiral patterns has two lobes symmetric to the source point, and each lobe is symmetric with respect to the mid sagittal plane containing the source, due to the apparent spatial symmetry. Figure 33(e) corresponds to a cylinder radius of $R_0 = 1.5cm$ and optical properties of $\mu_a = 0.02cm^{-1}$, $\mu_s' = 5cm^{-1}$, and $A = 1.86$. Because on convex interface the spiral loop is much axially-tilted, the photon fluence at the tip of the lobe is difficult to calculate for stronger μ_a and μ_s' due to the limit in floating-point arithmetic as discussed in Chapter II.

4.4 FEM & Monte Carlo examinations

The spiral patterns found in Fig. 33 are examined against FEM solution of photon diffusion equation (Dehghani et al., 2009) and MC simulation (Yao et al., 2005) in the associated geometries. The FEM volumes and the highlighted spiral profile are illustrated in Fig. 34(a)-(c). Shown in Fig. 34(d) and (e) are photon fluences calculated by four methods: along a straight-line in a semi-infinite geometry using the semi-infinite analytic model, along the semi-infinite equivalent spiral profile using the analytic model of cylindrical geometry developed in Chapter II, and along the semi-infinite equivalent spiral profile using FEM solution of photon diffusion equation and MC simulation. The radius of the cylinder is $R_0 = 1.5cm$ and the optical properties are $\mu_a = 0.025cm^{-1}$, $\mu_s' = 10cm^{-1}$, and $A = 1.86$. For the convex geometry the largest line-of-sight distance examined is $15cm$, and since the MC results at source-detector separation longer than $11cm$ were too noisy, they were discarded. Despite that diffusion is not valid in near-source

region, the diffuse photon remission calculated along the displayed spiral directions agrees very well with that along a straight-line in a semi-infinite geometry.

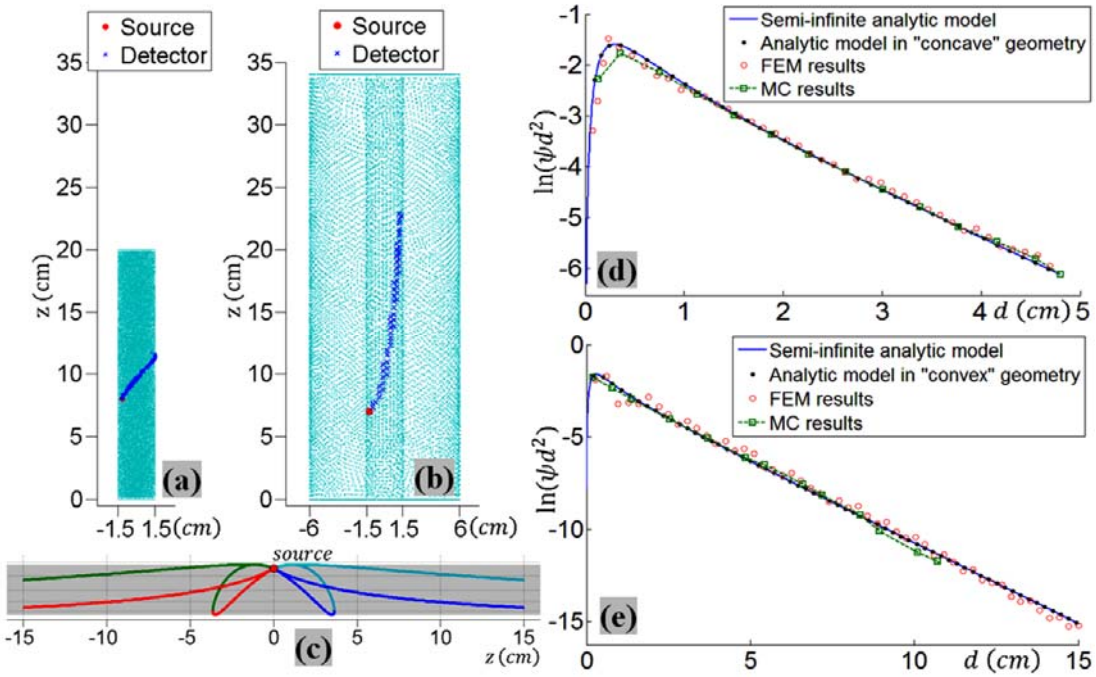

Fig. 34 Finite-element discretization of the medium that interfaces with a concave (a) or convex (b) cylindrical applicator. The indicated curve is one quarter of the 3-D spirally-shaped profiles shown in (c). Note that in (c) the spiral profile for convex-geometry is not in a closed-loop due to the limit of longitudinal dimensions. The photon remission along the indicated spiral directions are compared to the semi-infinite model, FEM and MC simulation for concave geometry in (d) and convex geometry in (e).

Note that the spiral path on a convex-shaped interface is tilted much more toward the longitudinal direction than on a concave-shaped interface, under otherwise identical conditions. It

is found that the spiral pattern is dependent upon the radius of the studied geometry, as indicated by Eqs. (4.2.10) and (4.2.19), and the optical properties of the medium as well, but is only weakly dependent upon the optical properties of the medium in convex geometry. We thereby anticipate that the much forward-tilted spiral direction in a convex geometry could be particularly useful for probing deep-tissue in endoscopic sensing applications. Among the potentials of taking advantage of this spiral profile, one configuration may be placing side-directed optodes parallel to the longitudinal axis and distantly along such spiral profiles on the imaging applicator within a body-cavity to interrogate deeper tissues, and to conveniently apply the semi-infinite model to quantify the photon remission measured in such configuration.

4.5 Perturbation to photon fluence rate in concave or convex geometries---Analytic treatment

The spiral-paths are demonstrated in ***concave*** and ***convex*** geometries for homogenous medium cases. However, it is questionable that the spiral-paths associated with homogenous-medium cases will hold for the medium containing heterogeneity. Practically, however, it may only be possible to examine the spiral-paths in limited cases of medium heterogeneity. To facilitate the examination by analytic means, this section employs perturbation-based analysis to derive the general form of photon fluence rate in ***concave*** or ***convex*** geometry that contains a single heterogeneity in otherwise homogenous medium.

We start with the equation of steady-state photon diffusion in an infinite medium as

$$\mu_a(\vec{r})\Psi(\vec{r}) - \nabla\cdot\left[D(\vec{r})\nabla\Psi(\vec{r})\right] = S(\vec{r}) \tag{4.5.1}$$

where $\Psi(\vec{r})$ is the photon fluence rate at position $\vec{r}$, and $S(\vec{r})$ is the source term. The optical heterogeneity to a homogenous medium of absorption coefficient μ_{a0} and diffusion coefficient D_0 may be represented by

$$\mu_a(\vec{r}) = \mu_{a0} + \delta\mu_a(\vec{r}) \tag{4.5.2}$$

$$D(\vec{r}) = D_0 + \delta D(\vec{r}) \tag{4.5.3}$$

and the resulted photon fluence rate is expressed by

$$\Psi(\vec{r}) = \Psi_0(\vec{r}) + \Psi_{SC}(\vec{r}) \tag{4.5.4}$$

where $\Psi_0(\vec{r})$ is photon fluence rate for homogeneous medium that satisfies the equation of

$$\mu_{a0}\Psi_0(\vec{r}) - D_0\nabla^2\Psi_0(\vec{r}) = S(\vec{r}) \tag{4.5.5}$$

and $\Psi_{SC}(\vec{r})$ represents a perturbation. By using Eqs. (4.5.2) - (4.5.4) we convert Eq. (4.5.1) to

$$\begin{aligned}\left[\mu_{a0} + \delta\mu_a(\vec{r})\right]\left[\Psi_0(\vec{r}) + \Psi_{SC}(\vec{r})\right] - D_0\nabla^2\left[\Psi_0(\vec{r}) + \Psi_{SC}(\vec{r})\right] \\ - \nabla\cdot\left\{\delta D(\vec{r})\cdot\nabla\left[\Psi_0(\vec{r}) + \Psi_{SC}(\vec{r})\right]\right\} = S(\vec{r})\end{aligned} \tag{4.5.6}$$

Subtracting Eq. (4.5.5) from Eq. (4.5.6) leads to

$$D_0\nabla^2\Psi_{SC}(\vec{r}) - \mu_{a0}\Psi_{SC}(\vec{r}) = \delta\mu_a(\vec{r})\left[\Psi_0(\vec{r}) + \Psi_{SC}(\vec{r})\right] - \nabla\cdot\left\{\delta D(\vec{r})\nabla\left[\Psi_0(\vec{r}) + \Psi_{SC}(\vec{r})\right]\right\} \tag{4.5.7}$$

For a weak heterogeneity (Arridge et al., 1991; O'Leary et al., 1995), i.e.,

$$\Psi_{SC}(\vec{r}) << \Psi_0(\vec{r}) \tag{4.5.8}$$

Equation (4.5.7) becomes

$$\nabla^2\Psi_{SC}(\vec{r}) - \frac{\mu_{a0}}{D_0}\Psi_{SC}(\vec{r}) = \frac{\delta\mu_a(\vec{r})}{D_0}\Psi_0(\vec{r}) - \frac{1}{D_0}\nabla\cdot\left\{\delta D(\vec{r})\nabla\Psi_0(\vec{r})\right\} \tag{4.5.9}$$

The Green's function of Eq. (4.5.9) satisfies the equation of

$$\nabla^2 G(\vec{r},\vec{r}') - \frac{\mu_{a0}}{D_0}G(\vec{r},\vec{r}') = -\delta(\vec{r}-\vec{r}') \tag{4.5.10}$$

We denote the source location as $\vec{r}_s$, the heterogeneity location as $\vec{r}'$, and the detector location as $\vec{r}_d$. The photon fluence rate measured at $\vec{r}'$ associated with a source at $\vec{r}_s$ is denoted as $\Psi_0(\vec{r}',\vec{r}_s)$, and $G(\vec{r}_d,\vec{r}')$ in Eq. (4.5.10) represents the response at $\vec{r}_d$ due to an impulse at $\vec{r}'$.

We now consider a ***concave*** geometry of radius R_0 and the extrapolated boundary condition based on Chapter II. For a directional source at $\vec{r}_s(R_0,\varphi_s,z_s)$ thereby an equivalent isotropic source at $\vec{r}_s(R_0-R_a,\varphi_s,z_s)$, and a heterogeneity at $\vec{r}'(\rho',\varphi',z')$ assuming that the heterogeneity locates deeper than R_a from the interface-boundary, i.e. $\rho' < R_0 - R_a$, we have

$$\Psi_0(\vec{r}',\vec{r}_s)=\frac{S}{D}\frac{1}{2\pi^2}\int_0^\infty dk\Bigg\{\cos[k(z'-z_s)]\sum_{m=0}^{\infty}\varepsilon_m I_m(k_{eff}\rho')K_m[k_{eff}(R_0-R_a)]$$

$$\cdot\left\langle 1-\frac{I_m[k_{eff}(R_0-R_a)]}{K_m[k_{eff}(R_0-R_a)]}\frac{K_m[k_{eff}(R_0+R_b)]}{I_m[k_{eff}(R_0+R_b)]}\right\rangle\cos[m(\varphi'-\varphi_s)]\Bigg\} \quad (4.5.11\text{conC})$$

where I_m and K_m are the modified Bessel Functions of the first and second kinds, respectively, $k_{eff}=\sqrt{k^2+k_0^2}$, and

$$\varepsilon_m=\begin{cases}2 & m>0\\ 1 & m=0\end{cases} \quad (4.5.12)$$

For the heterogeneity at $\vec{r}'(\rho',\varphi',z')$ and a detector at $\vec{r}_d(R_0,\varphi_d,z_d)$, note $\rho' < R_0$, we have

$$G(\vec{r}_d,\vec{r}')=\frac{1}{2\pi^2}\int_0^\infty dk\Bigg\{\cos[k(z_d-z')]\sum_{m=0}^{\infty}\varepsilon_m I_m(k_{eff}\rho')K_m(k_{eff}R_0)$$

$$\cdot\left\langle 1-\frac{I_m(k_{eff}R_0)}{K_m(k_{eff}R_0)}\frac{K_m[k_{eff}(R_0+R_b)]}{I_m[k_{eff}(R_0+R_b)]}\right\rangle\cos[m(\varphi_d-\varphi')]\Bigg\} \quad (4.5.13\text{conC})$$

Similarly we consider a ***convex*** geometry of radius R_0 and the extrapolated boundary condition. For a directional source at $\vec{r}_s(R_0,\varphi_s,z_s)$ thereby an equivalent isotropic source at

$\vec{r}_s\left(R_0+R_a,\varphi_s,z_s\right)$, and a heterogeneity at $\vec{r}'\left(\rho',\varphi',z'\right)$ assuming that the heterogeneity locates deeper than R_a from the interface-boundary, i.e. $\rho'>R_0+R_a$, we have

$$\Psi_0\left(\vec{r}',\vec{r}_s\right)=\frac{S}{D}\frac{1}{2\pi^2}\int_0^\infty dk\left\{\cos\left[k\left(z'-z_s\right)\right]\sum_{m=0}^{\infty}\varepsilon_m I_m\left[k_{eff}\left(R_0+R_a\right)\right]K_m\left(k_{eff}\rho'\right)\right.$$

$$\left.\cdot\left\langle 1-\frac{I_m\left[k_{eff}\left(R_0-R_b\right)\right]}{K_m\left[k_{eff}\left(R_0-R_b\right)\right]}\frac{K_m\left[k_{eff}\left(R_0+R_a\right)\right]}{I_m\left[k_{eff}\left(R_0+R_a\right)\right]}\right\rangle\cos\left[m\left(\varphi'-\varphi_s\right)\right]\right\} \quad (4.5.11\text{conV})$$

For the heterogeneity at $\vec{r}'\left(\rho',\varphi',z'\right)$ and a detector at $\vec{r}_d\left(R_0,\varphi_d,z_d\right)$, note $\rho'>R_0$, we have

$$G\left(\vec{r}_d,\vec{r}'\right)=\frac{1}{2\pi^2}\int_0^\infty dk\left\{\cos\left[k\left(z_d-z'\right)\right]\sum_{m=0}^{\infty}\varepsilon_m I_m\left(k_{eff}R_0\right)K_m\left(k_{eff}\rho'\right)\right.$$

$$\left.\cdot\left\langle 1-\frac{I_m\left[k_{eff}\left(R_0-R_b\right)\right]}{K_m\left[k_{eff}\left(R_0-R_b\right)\right]}\frac{K_m\left(k_{eff}R_0\right)}{I_m\left(k_{eff}R_0\right)}\right\rangle\cos\left[m\left(\varphi_d-\varphi'\right)\right]\right\} \quad (4.5.13\text{conV})$$

The solution to Eq. (4.5.9), representing the change to the photon fluence rate measured at $\vec{r}_d$ associated with a source at $\vec{r}_s$ by the heterogeneity at $\vec{r}'$ is then

$$\Psi_{SC}\left(\vec{r}_d,\vec{r}_s\right)=-\frac{1}{D_0}\iiint_V G\left(\vec{r}_d,\vec{r}'\right)\delta\mu_a\left(\vec{r}'\right)\Psi_0\left(\vec{r}',\vec{r}_s\right)d^3r'$$

$$+\frac{1}{D_0}\iiint_V G\left(\vec{r}_d,\vec{r}'\right)\nabla\cdot\left\{\delta D\left(\vec{r}'\right)\nabla\Psi_0\left(\vec{r}',\vec{r}_s\right)\right\}d^3r' \quad (4.5.14)$$

In Eq. (4.5.14), the first term of integration is associated with the absorption heterogeneity, and the second term of integration is associated with the diffusion heterogeneity. Appendix D shows that the second term can be transformed, and by that transformation Eq. (4.5.14) changes to

$$\Psi_{SC}\left(\vec{r}_d,\vec{r}_s\right)=-\frac{1}{D_0}\iiint_V G\left(\vec{r}_d,\vec{r}'\right)\delta\mu_a\left(\vec{r}'\right)\Psi_0\left(\vec{r}',\vec{r}_s\right)d^3r'$$

$$-\frac{1}{D_0}\iiint_V \delta D\left(\vec{r}'\right)\nabla G\left(\vec{r}_d,\vec{r}'\right)\cdot\nabla\Psi_0\left(\vec{r}',\vec{r}_s\right)d^3r' \quad (4.5.15)$$

It is worthy to notice that there is a mistake seen in analytic descriptions of some previous works similar in form to Eq. (4.5.15), such as Eq. (2) in (O'Leary et al., 1995) and Eq. (11.63) in (Wang et al., 2007), regarding the sign associated with the second term of integration. The detailed accounting in Appendix D shall clarify the "-" sign, rather than a "+" sign, associated with the second term of integration related to the diffusion heterogeneity.

For an inclusion of volume V and a uniform contrast over the background medium, we define the absorption strength of the inclusion with respect to the background medium as

$$\delta P_{\mu_a} = \frac{\left\| \delta\mu_a \bullet V \right\|}{\mu_{a0}} \tag{4.5.16}$$

and the scattering strength of the inclusion with respect to the background medium as

$$\delta P_D = \frac{\left\| \delta D \bullet V \right\|}{D_0} \tag{4.5.17}$$

Equation (4.5.16) implies that the same level of absorption perturbation to the photon fluence rate could be caused by either a smaller anomaly with stronger absorption contrast or a larger anomaly with weaker absorption contrast. Equation (4.5.17) implies that the same level of scattering perturbation to the photon fluence rate could be caused by either a smaller anomaly with stronger scattering contrast or a larger anomaly with weaker scattering contrast. Then Eq. (4.5.15) becomes

$$\Psi_{SC}\left(\vec{r}_d, \vec{r}_s\right) = -\delta P_{\mu_a} \frac{\mu_{a0}}{D_0} G\left(\vec{r}_d, \vec{r}'\right) \Psi_0\left(\vec{r}', \vec{r}_s\right) - \delta P_D \, \nabla G\left(\vec{r}_d, \vec{r}'\right) \cdot \nabla \Psi_0\left(\vec{r}', \vec{r}_s\right) \tag{4.5.18}$$

The gradient operator in Eq. (4.5.18) can be expanded in cylindrical coordinates as:

$$\begin{aligned} \nabla G\left(\vec{r}_d, \vec{r}'\right) \cdot \nabla \Psi_0\left(\vec{r}', \vec{r}_s\right) = & \left\{ \left[\frac{\partial G\left(\vec{r}_d, \vec{r}'\right)}{\partial \rho'} \right] \left[\frac{\partial \Psi_0\left(\vec{r}', \vec{r}_s\right)}{\partial \rho'} \right] \right. \\ & \left. + \left[\frac{1}{\rho'} \frac{\partial G\left(\vec{r}_d, \vec{r}'\right)}{\partial \varphi'} \right] \left[\frac{1}{\rho'} \frac{\partial \Psi_0\left(\vec{r}', \vec{r}_s\right)}{\partial \varphi'} \right] + \left[\frac{\partial G\left(\vec{r}_d, \vec{r}'\right)}{\partial z'} \right] \left[\frac{\partial \Psi_0\left(\vec{r}', \vec{r}_s\right)}{\partial z'} \right] \right\} \end{aligned} \tag{4.5.19}$$

4.6 Perturbation to photon fluence rate by a weak target aligned azimuthally with the spiral paths----numerical evaluation based on analytic treatment

This section aims to evaluate the photon fluence rate along the spiral-paths identified for homogenous medium cases, when the medium contains a weak heterogeneous inclusion whose center is aligned azimuthally with one location on the spiral-paths. The perturbation analysis discussed in the previous section will be numerically implemented for the weak inclusion. For ***concave*** and ***convex*** geometries, the partial derivatives in Eq. (4.5.19) can be numerically approximated using central difference scheme, after $\Psi_0(\vec{r}', \vec{r}_s)$ and $G(\vec{r}_d, \vec{r}')$ are quantified based on the numerical methods demonstrated in Chapter II and Chapter III. As the evaluation of spiral-paths with inclusion in ***concave*** or ***convex*** geometry has to involve evaluating photon fluence rate along a straight-line in a semi-infinite geometry with identical inclusion, the gradient operator in Eq. (4.5.18) will be expanded in Cartesian coordinates for the semi-infinite geometry and the resulted partial derivatives will be found similarly by central difference scheme.

We consider a spherical anomaly of 0.15cm in radius and 0.25cm in depth that is aligned with one quadrant of the spiral-paths, as shown in Fig. 35. The position of the anomaly is chosen so that in the ***concave*** geometry (Fig. 35.A) the azimuthal angle between the anomaly center and the source is $\pi/2$. In the semi-infinite geometry (Fig. 35.B) and the ***convex*** geometry (Fig. 35.C), the position of the anomaly is chosen such that the line-of-sight distance between the source and the projection of the anomaly center onto the straight-line or spiral-path (hence the physical boundary) is kept the same as that in the ***concave*** geometry. Table 3 lists the four sets of optical parameters assigned to the single anomaly, which include positive μ_a, positive μ_s', negative μ_a, and negative μ_s' contrasts with respect to those of the background medium that is not necessarily identical in the four cases. The radii of both ***concave*** and ***convex*** applicators are set as 1.5cm and A = 1.86 is chosen.

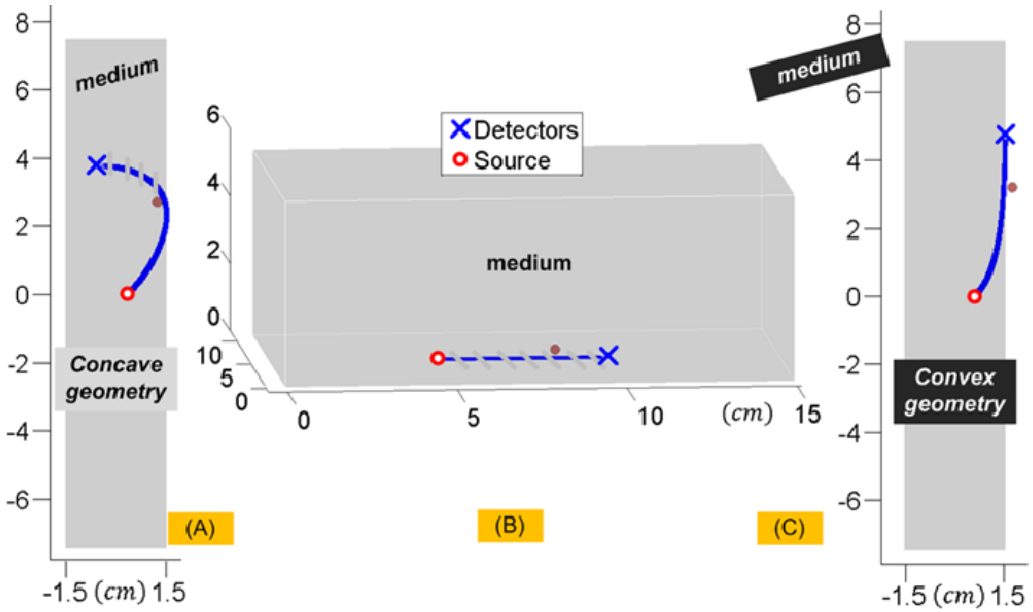

Fig. 35 Position of the anomaly of weak perturbation strength in the otherwise homogeneous background medium. (A) Concave geometry, (B) semi-infinite geometry, (C) convex geometry.

Table 3. The four sets of optical parameters for evaluating the change to photon fluence rate by an anomaly of weak contrast to the background medium.

		Background μ_a (cm^{-1})	Background μ_s' (cm^{-1})	Anomaly μ_a (cm^{-1})	Anomaly μ_s' (cm^{-1})
Set 1	positive μ_a contrast	0.025	10.0	**0.05**	10.0
Set 2	positive μ_s' contrast	0.025	10.0	0.025	**12.0**
Set 3	negative μ_a contrast	**0.05**	10.0	0.025	10.0
Set 4	negative μ_s' contrast	0.025	**12.0**	0.025	10.0

The results of numerical evaluation based on the four cases of contrasts specified in Table 3 are given in Fig. 36. In each of the sub figures from (A) to (D), the photon fluence rates are

compared among four configurations: (1) along a straight line in the semi-infinite geometry for homogeneous medium, which is used as the reference and colored by green; (2) along a straight-line in semi-infinite geometry with the anomaly; (3) along the spiral profile in the ***concave*** geometry with the anomaly; (4) along the spiral profile in the ***convex*** geometry with the anomaly. The photon fluence curves for the four configurations are shown indistinguishable at the macroscopic scale of near-5cm range for d. To examine the microscopic differences of the photon fluence curves, the curves corresponding to a 0.1 cm range of d and centering at the azimuthal coordinate of the anomaly are magnified as the inset in each sub figure. Under the magnification, it is found that (1) the photon fluence curves associated with the anomaly are clearly distinguished from the green reference; (2) the photon fluence curves associated with the anomaly of absorption contrast are still indistinguishable among the three geometries; and (3) the photon fluence curves associated with the anomaly of scattering contrast are distinguishable among the three geometries, with the curves of ***concave*** and ***convex*** geometries locating very close to and at the opposite sides of the curve of semi-infinite geometry.

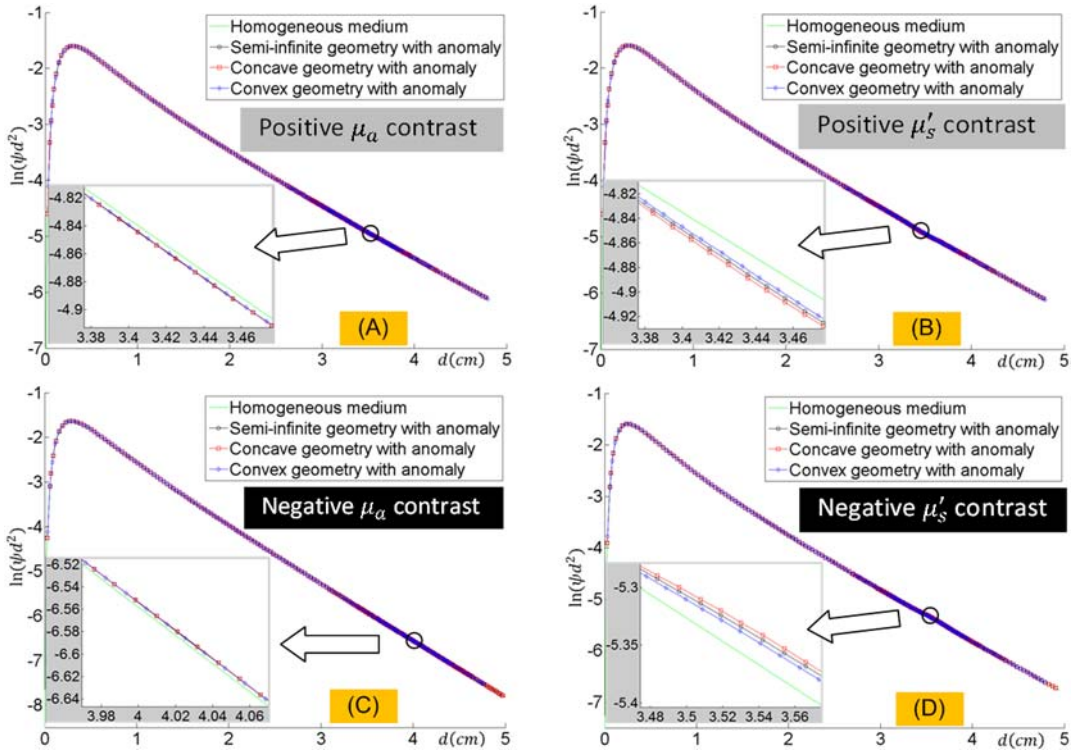

Fig. 36 Photon fluence rate when one weak anomaly resides in the otherwise homogeneous background medium. The anomaly possesses (A) positive μ_a contrast, (B) positive μ_s' contrast, (C) negative μ_a contrast, and (D) negative μ_s' contrast over the background. The shown curves of photon fluence are plotted for (1) along a straight line in semi-infinite geometry of homogenous medium, (2) along a straight line in semi-infinite geometry having the anomaly aligned with the straight line, (3) along the spiral profile in concave geometry having the anomaly aligned with the spiral profile, and (4) along the spiral profile in convex geometry having the anomaly aligned with the spiral profile.

4.7 Perturbation to photon fluence rate by a strong target aligned azimuthally with the spiral paths ----numerical evaluation based on finite element method

As the perturbation analysis becomes increasingly inaccurate for increasing contrast-strength of the anomaly, FEM computation based on NIRFAST (Dehghani et al., 2009) is implemented to evaluate the photon fluence rate along the spiral-paths when a strong anomaly resides in the medium.

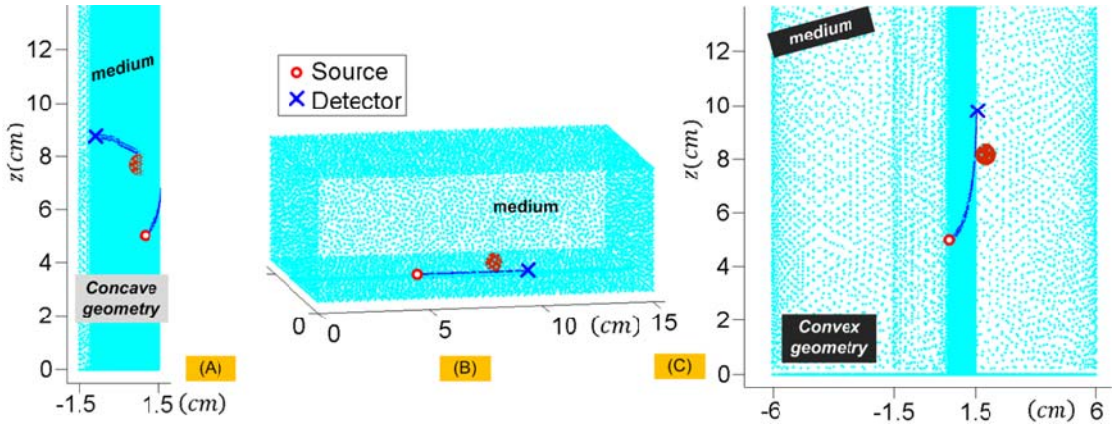

Fig. 37 Finite-element discretization of the imaging domain and the position of the anomaly with strong perturbation strength. (A) concave geometry, (B) semi-fininte geometry, and (C) convex geometry.

The FEM meshing domain is illustrated in Fig. 37 (A), (B), and (C) for ***concave***, semi-infinite, and ***convex*** geometries, respectively. In the ***concave*** geometry, the meshing volume is a cylinder of 14cm in height and 1.5cm in radius, which is discretized into 76,620 nodes and 349,697 tetrahedral elements. The surface containing the spiral profile is set with higher node density. In the semi-infinite geometry, the meshing volume is a rectangle of $15\times11\times5.5\text{cm}^3$, which is discretized into 88,941 nodes and 496,211 elements. The straight line for evaluating the

photon fluence rate is set with higher node density. In the ***convex*** geometry, the meshing domain is the volume between two concentric cylinders of 15cm in height, with 1.5cm inner radius and 6cm outer radius. The meshing volume is discretized into 83,312 nodes and 437,039 tetrahedral elements. The surface containing the spiral profile is set with denser nodes.

We consider a spherical anomaly of 0.4cm in radius and 0.5cm in depth that is aligned azimuthally with one quadrant of the spiral-paths. The positions of the anomaly in ***concave***, semi-infinite and ***convex*** geometries are chosen following the same rules as in Section 4.6. Table 4 lists the four sets of optical parameters assigned to the single anomaly, which include positive μ_a, positive μ_s', negative μ_a, and negative μ_s' contrasts with respect to those of the background medium that is not necessarily identical in the four cases. The four sets of anomaly defined in Table 4 has approximately 57 times of positive absorption strength, 57 times of positive scattering strength, 28 times of negative absorption strength and 95 times of negative scattering strength, respectively, of the ones defined in Table 3, when counting the difference in volume.

Table 4. The four sets of optical parameters used for evaluating the change to photon fluence rate by an anomaly of strong contrast to the background medium

		Background μ_a (cm^{-1})	Background μ_s' (cm^{-1})	Anomaly μ_a (cm^{-1})	Anomaly μ_s' (cm^{-1})
Set 1	positive μ_a contrast	0.025	10.0	**0.1**	10.0
Set 2	positive μ_s' contrast	0.025	10.0	0.025	**20.0**
Set 3	negative μ_a contrast	**0.1**	10.0	0.025	10.0
Set 4	negative μ_s' contrast	0.025	**20.0**	0.025	10.0

The results of FEM simulation based on the four cases of contrasts as specified in Table 4 are given in Fig. 38. In each of the sub figures from (A) to (D), the photon fluence rates are

compared among four configurations as did with Fig. 36. At the macroscopic scale of near-5cm range for *d*, the photon fluence curves for the three geometries with the anomaly are distinguished from the green reference except for negative μ_a contrast; however the photon fluence curves for the three geometries with the anomaly are nearly indistinguishable. At the microscopic level similar to that in Fig. 36, the photon fluence curves of the ***concave*** and ***convex*** geometries are very close to and at the opposite sides of the curve of semi-infinite geometry, for anomaly of either absorption or scattering contrast.

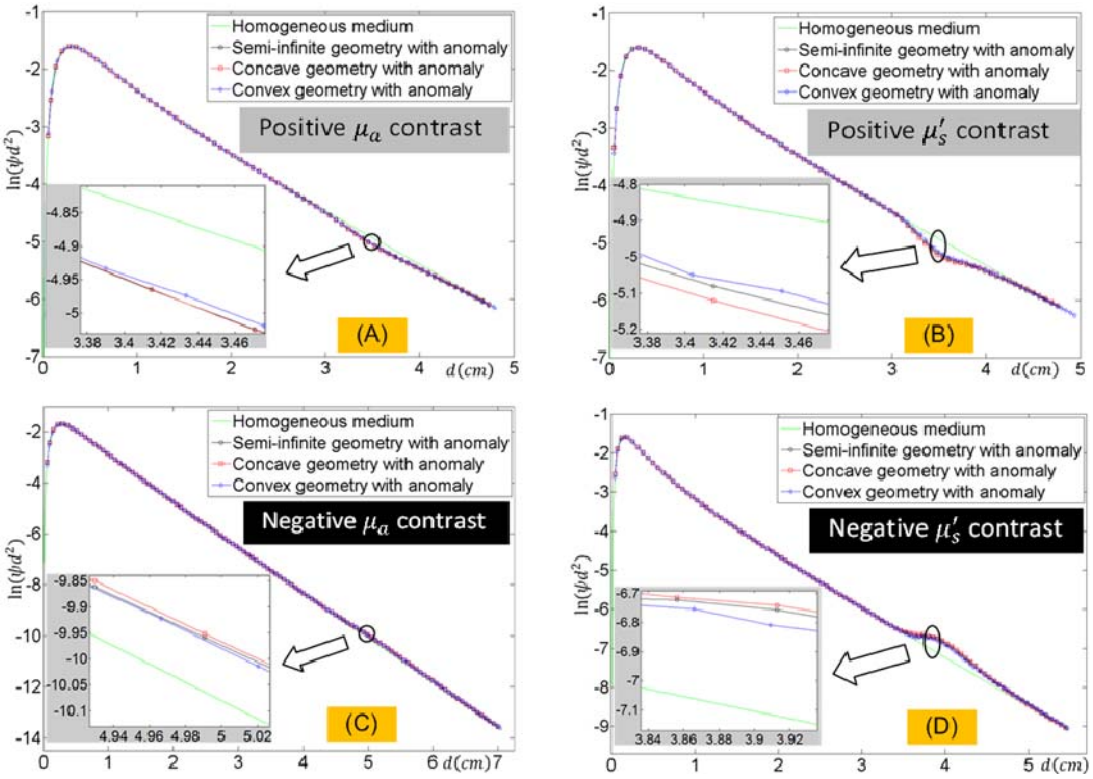

Fig. 38 Finite-element discretization of the imaging domain and the position of the anomaly with strong perturbation strength. (A) concave geometry, (B) semi-fininte geometry, and (C) convex geometry.

4.8 Discussion

Our previous studies have suggested and demonstrated the existence of spiral-paths in the ***concave*** and ***convex*** geometries for homogenous medium conditions. As stated earlier, the spiral-paths refers to the equivalence of a unique set of directions in the ***concave*** and ***convex*** geometries to a straight-line in a semi-infinite geometry, in terms of the decay-rate of photon fluence with respect to the line-of-sight distance between a source and a detector positioned for probing a homogenous medium. Such equivalence of the spiral-directions in ***concave*** or ***convex*** geometries to a straight-line in a semi-infinite geometry may very well be limited to only the specific set of parameters. For ***concave*** and ***convex*** geometries of large radii, Eq. (4.2.10) and (4.2.19) represent the spiral-paths by means of the angle α. It is unmistakable that α is a function of R_0, and α should also be affected by R_a and R_b which collectively are determined by the optical properties of medium and tissue-applicator interface. It is therefore imperative to examine the actual profile of spiral-paths associated with different geometric and optical parameters.

Figure 39 investigates the spiral-paths associated with different sets of geometric and optical parameters. Since the four limbs of the spiral-paths in both ***concave*** and ***convex*** geometries are symmetric with regard to the mid-sagittal plane containing the source, only one quadrant of the spiral-paths is to be investigated. The spiral-paths found for ***concave*** geometry are grouped in the left column, and for ***convex*** geometry in the right column. The set of base-line parameters are $R_0 = 1.5cm$, $A = 1.86$, $\mu_a = 0.025cm^{-1}$, and $\mu_s' = 10cm^{-1}$, and each of the plots from (A) to (F) has one parameter differing from the base-line parameters. Specifically, (A) and (B) correspond to changing radius from 1, 1.5, to 2 cm; (C) and (D) correspond to changing A value from 1, 1.86, to 2.82; (E) and (F) correspond to changing μ_a from 0.025, 0.05, to 0.1 cm^{-1}; and (G) and (H) corresponds to changing μ_s' from 5, 10, to 20 cm^{-1}. The most salient feature observed from Fig. 39 is that the spiral profile develops much deeper into the *z* direction in the

convex geometry than in the ***concave*** geometry, for the otherwise identical set of parameters. The value of A seems to have little effect on the profile of spiral paths in both geometries. The spiral profile is shown to relate to other parameters, however, it is affected considerably less in ***convex*** geometry than in ***concave*** geometry.

As this study has also investigated whether the spiral-paths found for homogenous medium specific to a given set of optical parameters would be valid for the same geometry if the medium contains heterogeneity, two observations are noted. At the macroscopic scale, the photon fluence curves for the three geometries associated with the anomaly are nearly indistinguishable from each other even for the strong anomaly considered, indicating that the spiral-paths is a good approximation macroscopically. At sufficiently-detailed microscopic scale, the photon fluence curves for the three geometries associated with the anomaly do become apart; however, the photon fluence curves of the concave and convex geometries seem to locate at the opposite sides of the curve of semi-infinite geometry. As the numerical evaluation based on the analytic treatment involves summing modified Bessel functions of finite orders, and the FEM is implemented at finite resolution of the elements, limited precision is expected for the shown numerical results, as expressed by the slight oscillatory behavior of the curves associated with concave or convex geometries visible at microscopic scales. The deviation of the photon fluence curve of concave or convex geometry from that of semi-infinite geometry may be due to the slight variance of the spiral-paths with respect to the actual optical properties, indicating that the spiral-paths could be considered a good approximation to a straight-line, but it is not identical to a straight-line in semi-infinite geometry. Apparently the deviation of the photon fluence curve of concave or convex geometry from that of semi-infinite geometry is to become smaller as the radial dimension of concave or convex applicator is to be increased.

This study examined the change to photon fluence rate along the spiral-paths of concave and convex geometries identified for homogeneous medium cases when only one anomaly is introduced into the medium. The perturbation analysis, being linear in its nature, can in principle

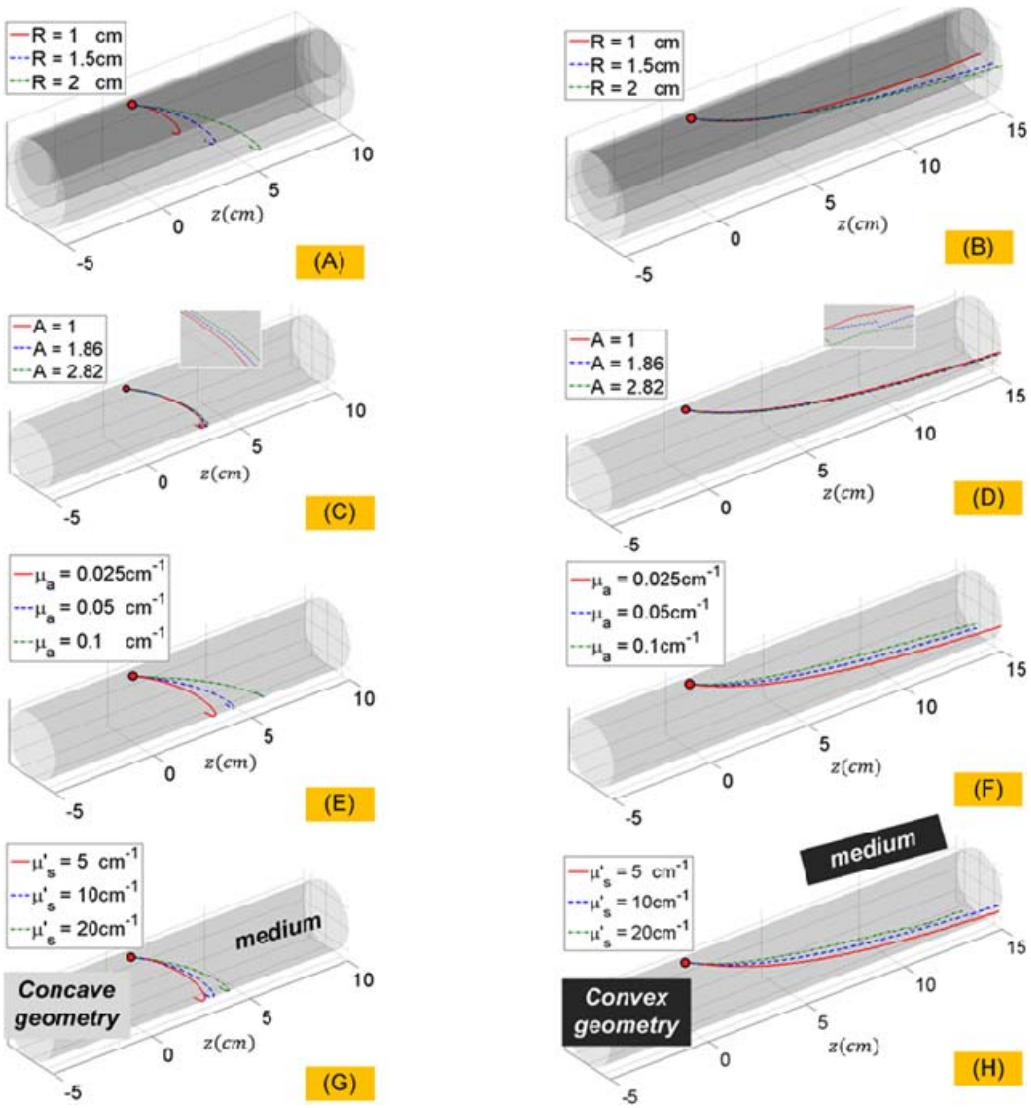

Fig. 39 The spiral profiles of ***concave*** geometry (left column) and ***convex*** geometry (right column) found for different geometric parameters and optical properties. Each subplot illustrates the spiral profiles associated with the change of only parameter with respect to a set of base-line parameters. The parameter to be changed in (A) and (B) is the radius of the cylindrical applicator. The parameter to be changed in (C) and (D) is the A value. The parameter to be changed in (E) and (F) is μ_a. The parameter to be changed in (G) and (H) is μ_s'.

be applied to multiple anomalies. However the results based on numerical implementation of the perturbation-based analytic approach will become increasingly inaccurate if anomalies with large volume or strong contrast are included due to the non-linearity between the photon fluence and μ_a or μ_s'. Certainly FEM would facilitate more accurate evaluation for multiple anomalies of various contrasts. This study is also specific to the case of having the only anomaly aligned azimuthally with the spiral-paths. If the same anomaly is placed off from the position aligning with the spiral-paths, the change to the photon fluence rate measured along the spiral-paths by the anomaly is expected to be less than that shown in Fig. 36 and Fig. 38. In that case the photon fluence curves associated with the three geometries with the anomaly as studied in Fig. 35 and Fig. 37 will become less distinguishable. Therefore the approximation by spiral-paths is more accurate for an inclusion not aligned with the spiral-paths than one aligned with the spiral-paths.

4.9 Conclusions

This study continued the work of examining steady-state photon diffusion in a ***concave*** or ***convex*** geometry. The analysis in either of these two geometries has implications to diffuse optical sensing of externally-applicable or internally-applicable tissue medium. The study specifically complemented our previous prediction that, on the tissue-applicator interface of either ***concave*** or ***convex*** geometry there exists a unique set of spiral-paths, along which the steady-state photon fluence rate decays at a rate equal to that along a straight-line in a planar semi-infinite geometry, for the same line-of-sight source–detector distance. This phenomenon, referred to as "spiral-paths", is demonstrated analytically for ***concave*** or ***convex*** geometry of large radial dimension, and numerically for ***concave*** or ***convex*** geometry of small radial dimension. This study also examined the spiral-paths when the medium contained heterogeneity. Although the heterogeneity being investigated is limited to an anomaly with either positive or negative contrast of absorption

or scattering coefficient over the background medium, by aligning the anomaly azimuthally with the spiral-paths the anomaly has the maximum sensitivity to the change to photon fluence rate. For an anomaly of weak contrast-strength the effect of it to the photon fluence rate along the spiral-paths is calculated by a well-established perturbation analysis. Our revisiting of the perturbation analysis for numerical implementation in cylindrical coordinates helped identify a mistake appearing in similar analyses in some previous works. As the perturbation analysis is limited to weak-target cases, the change by an anomaly of strong-contrast to the photon fluence rate along the spiral-paths is instead computed by using FEM. For all investigated heterogeneous medium cases the photon fluence rate along the homogenous-medium associated spiral-paths is macroscopically indistinguishable from that along a straight line in a semi-infinite geometry, though microscopically the discrepancy is observed.

CHAPTER V

TRANS-LUMINAL PHOTON DIFFUSION: FREQUENCY-DOMAIN ANALYSIS

5.1 Introduction (Zhang A, Piao D et al., 2012)

Modeling optical imaging of biological tissue located centimeters deep involves diffusion approximation to the radiative transport (Ishimaru et al., 1989). Although the semi-infinite geometry specific to placing the optodes on a planar medium-applicator interface is most widely studied, other geometries with the optodes on curved medium-applicator interface could be more relevant to imaging applications (Hielscher et al., 2002). A "***concave***" geometry may resemble probing the diffusive medium at the "recessing" side of the cylindrical applicator, and a "***convex***" imaging geometry may represent probing the diffusive medium at the "bulging" side of the cylindrical applicator (Piao et al., 2006). For the semi-infinite geometry with a homogeneous medium, the analytic solution to the photon diffusion is well-studied (Fantini et al., 1994) and has been applied widely to analyzing raw data measured from surface tissue applicators and for image reconstruction. For "concave" medium-applicator geometry there are a noticeable amount of studies of diffuse photon propagation within the geometry. Arguably all these approaches were based on the same methodology, i.e., the analytical Green's function is derived in the form of a sum of two terms that contain the analytical solution in the infinite medium plus a particular solution, specifically the one corresponding to an "image" source, allowing the global solution to satisfy the boundary condition. In terms of frequency-domain (FD) modeling, Arridge et al. (Arridge et al., 1992) applied zero fluence boundary condition to derive the solutions for finite-length and infinite-length "concave" cylinder geometries, using Green's functions as well as their Laplace transforms similar to those demonstrated by Carslaw and Jaeger on heat conduction (Carslaw et al., 1986). Pogue and Patterson (Pogue et al., 1994) used the extrapolated boundary

condition, which is considered more accurate than zero-boundary condition for tissue-applicator interface (Haskell et al., 1994; Contini et al., 1997), to derive the solutions for a finite-length "concave" cylinder geometry. Da Silva et al. (Silva et al., 2009) also employed extrapolated boundary condition to study photon diffusion in finite-length "concave" cylindrical geometries. Recently Liemert and Kienle (Liemert et al., 2010; Liemert et al., 2, 2010) employed finite Hankel and cosine transforms to reach a solution of FD photon diffusion in the medium bounded by single or multi-layered infinitely long "concave" cylinder. However, there is lack of understanding regarding FD photon diffusion associated with "convex" medium-applicator geometry.

In Chapter II, we developed a theoretical framework to unify the treatment of continuous-wave (CW) photon remission on the medium-applicator interface of both "concave" and "convex" geometries with infinite longitudinal dimension. Solutions to the CW photon diffusion in the two geometries were derived based on the extrapolated boundary condition and expressed in terms of the first and second kinds of the modified Bessel functions. In Chapter III, the validity of the analytic treatment of Chapter II in the diffusion regime was examined by means including finite-element-method (FEM), Monte Carlo modeling, and experiments. It was found that in both "concave" and "convex" geometries the changes of CW photon fluence along the azimuthal and longitudinal directions showed opposite trends, in terms of the decay rate versus the line-of-sight source-detector distance with respect to that along a straight line on a semi-infinite medium-applicator interface for the same line-of-sight source-detector distance. Futher, it was predicted in Chapter III and subsequently outlined and detailed in Chapter IV that there was a unique set of spiral paths on the medium-applicator interface in both concave and convex geometries of infinite longitudinal dimension, along which the decay-rate of CW photon fluence could be identical to that along a straight line on the semi-infinite medium-applicator interface, given the same line-of-sight source-detector distance and the same set of optical properties.

In this Chapter, the methodology introduced in Chapter II for analysis of CW photon diffusion is extended to formulate a unified analysis of FD photon diffusion in both concave and convex geometries of infinite longitudinal dimension. Section 5.2 reviews the FD photon diffusion for infinite and semi-infinite geometries expressed in both spherical and cylindrical coordinates. Section 5.3 develops the cylindrical-coordinate solutions to FD photon diffusion in both "concave" and "convex" geometries, respectively. Section 5.4 generalizes the characteristics of FD photon diffusion along the azimuthal and longitudinal directions in concave and convex geometries, by assuming a large radius of the cylinder geometry that renders analytical approximations to be made. Section 5.5 presents numerical evaluations of FD photon fluence along the azimuthal and longitudinal directions with respect to the source-detector distance for concave and convex geometries of practical centimeter-order radius, based on FEM and analytical results. We demonstrate in this chapter that the aforementioned spiral-paths exist for the amplitude of AC fluence rate as well; however, they do not coincide with those for DC fluence rate. As long as the modulation depth and phase are concerned, no such spiral-paths can be inferred.

5.2 Frequency-domain Analysis for Infinite and Semi-Infinite Geometries---Recounting

We consider a scattering dominant medium with a diffusion coefficient $D=\left[3\left(\mu_a+\mu_s'\right)\right]^{-1}$, where μ_a is the absorption coefficient and μ_s' is the reduced scattering coefficient. The locations of a detector $\vec{r}$ and a source $\vec{r}'$ are represented in cylindrical-coordinates by (ρ,φ,z) and (ρ',φ',z'), respectively, for all medium geometries investigated in this study. A medium of

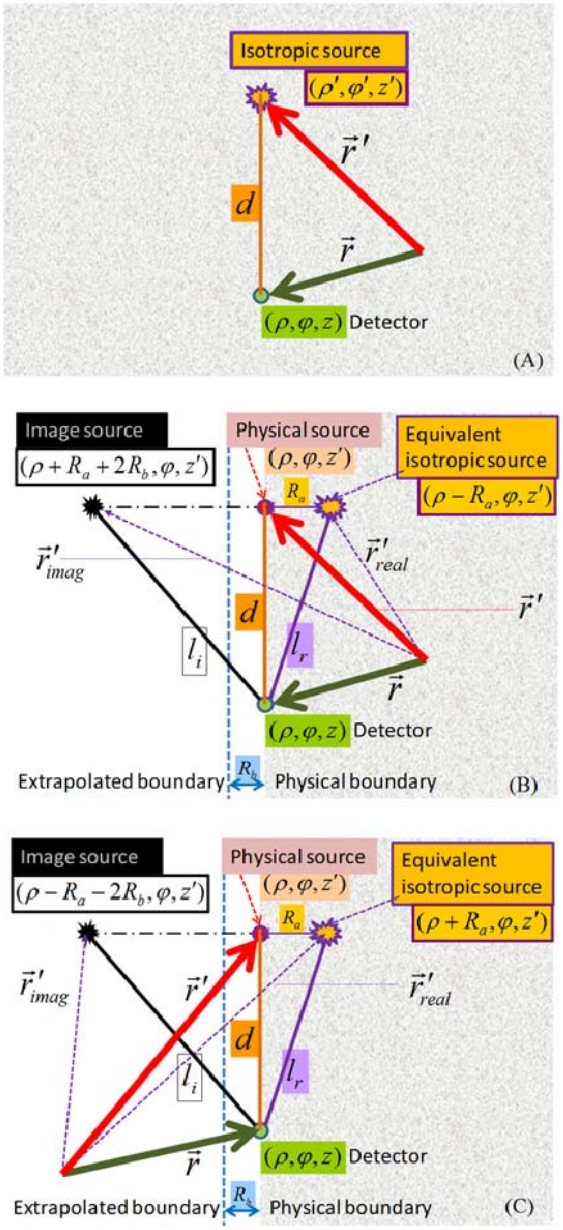

Fig. 40 Illustrations of a medium of infinite geometry in (A) and a medium of semi-infinite geometry in (B) and (C). In the semi-infinite geometry the source and detector are positioned on the physical boundary of the medium, and it becomes convenient to assign the same radial and azimuthal coordinates to the source and detector.

infinite geometry is illustrated in Fig. 40(A), wherein the source is regarded as isotropic. A medium of semi-infinite geometry with the source and the detector located on the medium boundary is depicted in Fig. 40(B) for the coordinate-origin located at the medium side or in Fig. 40(C) for the coordinate-origin located at the opposite to the medium side. In the semi-infinite geometry, the source $\vec{r}'\ (\rho', \varphi', z')$ launches photon into the medium at an initial direction orthogonal to the medium-applicator interface, and is represented by an equivalent "real" isotropic source at $\vec{r}'_{real}\ (\rho - R_a, \varphi, z')$ in Fig. 40(B) or $\vec{r}'_{real}\ (\rho + R_a, \varphi, z')$ in Fig. 40(C), where $R_a = 1/\mu_s'$ is the step-size of transport-scattering. The effect of medium-applicator interface on photon diffusion may be modeled by setting zero the photon fluence rate on an extrapolated boundary located $R_b = 2AD$ away from the physical boundary, where $A = (1 + R_{eff})/(1 - R_{eff})$, and R_{eff} is a coefficient (Haskell et al., 1994; Contini et al., 1997) determined by the refractive index differences across the physical boundary. This boundary condition is accommodated by setting a negative "image" source of the "real" isotropic source, with respect to the extrapolated boundary, at $\vec{r}'_{imag}\ (\rho + R_a + 2R_b, \varphi, z')$ in Fig. 40(B) or $\vec{r}'_{imag}\ (\rho - R_a - 2R_b, \varphi, z')$ in Fig. 40(C). The distances from the detector to the "real" isotropic source $\vec{r}'_{real}$ and the "image" source $\vec{r}'_{imag}$ are denoted by l_r and l_i, respectively. The notations of l_r and l_i also apply to other studied medium geometries involving a boundary. In all studied geometries, the straight distance between the source and the detector, i.e. $d = |\vec{r} - \vec{r}'|$, is referred to as the "line-of-sight" source-detector distance, with respect to which the changing characteristics of photo fluence rate Ψ are to be evaluated among different geometries. Hereafter the "source-detector distance" stands for line-of-sight source-detector distance.

A FD source at $\vec{r}'$ is expressed as $S(\vec{r}', t) = \bar{S}(\vec{r}') + \tilde{S}(\vec{r}')\exp(i\omega t)$, where the overhead notations "–" and "~" represent DC and AC components, respectively, and ω is the

angular frequency. Then the FD photon fluence rate at $\vec{r}$ is expressed by $\Psi(\vec{r},t) = \overline{\Psi}(\vec{r}) + \widetilde{\Psi}(\vec{r})\exp(i\omega t)$. For a homogeneous medium, we have the following photon diffusion equations (Ishimaru et al, 1989; Hielscher et al., 2002; Fantini et al., 1994; Arridge et al., 1992; Carslaw et al., 1986; Pogue et al., 1994; Haskell et al., 1994; Contini et al., 1997)

$$\nabla^2\overline{\Psi}(\vec{r}) - \bar{k}_0\ \overline{\Psi}(\vec{r}) = -\frac{\overline{S}(\vec{r})}{D}; \qquad \nabla^2\widetilde{\Psi}(\vec{r}) - \widetilde{k}_0\ \widetilde{\Psi}(\vec{r}) = -\frac{\widetilde{S}(\vec{r})}{D} \tag{5.2.1}$$

where $\bar{k}_0$ and $\widetilde{k}_0$ are the effective attenuation coefficients of the medium to the DC and AC components, respectively, of photon fluence rate as

$$\bar{k}_0 = \sqrt{\frac{\mu_a}{D}}; \qquad \widetilde{k}_0 = \widetilde{k}_{amp} + j\widetilde{k}_{phi} = \sqrt{\frac{\mu_a}{D} + \frac{i\omega}{Dc}} \tag{5.2.2}$$

with c being the speed of light in the medium, and

$$\widetilde{k}_{amp} = \bar{k}_0\sqrt{\frac{1}{2}\left(\sqrt{1+\left(\frac{\omega}{c\mu_a}\right)^2}+1\right)}; \qquad \widetilde{k}_{phi} = \bar{k}_0\sqrt{\frac{1}{2}\left(\sqrt{1+\left(\frac{\omega}{c\mu_a}\right)^2}-1\right)} \tag{5.2.3}$$

5.2.1 Solutions in spherical-coordinates to FD photon diffusion

5.2.1.A Source and detector in an infinite medium geometry

For a source and a detector in a homogeneous medium of infinite geometry, the solutions to Eqs. (5.2.1) in spherical-coordinates are well-known to be

$$\overline{\Psi}_{\inf}(\vec{r},\vec{r}') = \frac{\overline{S}}{4\pi D}\frac{1}{|\vec{r}-\vec{r}'|}\exp\left(-\bar{k}_0|\vec{r}-\vec{r}'|\right) \tag{5.2.4.DC}$$

$$\widetilde{\Psi}_{\inf}(\vec{r},\vec{r}') = \frac{\widetilde{S}}{4\pi D}\frac{1}{|\vec{r}-\vec{r}'|}\exp\left(-\widetilde{k}_{amp}|\vec{r}-\vec{r}'|\right)\exp\left(-i\widetilde{k}_{phi}|\vec{r}-\vec{r}'|\right) \tag{5.2.4.AC}$$

5.2.1.B Source and detector on a semi-infinite medium-applicator interface

For a source and a detector located on a semi-infinite boundary to a homogeneous medium, the solutions to Eqs. (5.2.1) in spherical-coordinates may be derived based on the aforementioned extrapolated boundary condition as

$$\overline{\Psi}_{semi} = \overline{\Psi}_{real}(\vec{r}, \vec{r}'_{real}) + \overline{\Psi}_{imag}(\vec{r}, \vec{r}'_{imag}) = \frac{\overline{S}}{4\pi D l_r}\exp\left(-\bar{k}_0 l_r\right) - \frac{\overline{S}}{4\pi D l_i}\exp\left(-\bar{k}_0 l_i\right) \quad (5.2.5.\text{DC})$$

$$\widetilde{\Psi}_{semi} = \widetilde{\Psi}_{real}(\vec{r}, \vec{r}'_{real}) + \widetilde{\Psi}_{imag}(\vec{r}, \vec{r}'_{imag}) = \frac{\widetilde{S}}{4\pi D l_r}\exp\left(-\widetilde{k}_0 l_r\right) - \frac{\widetilde{S}}{4\pi D l_i}\exp\left(-\widetilde{k}_0 l_i\right) \quad (5.2.5.\text{AC})$$

where we have

$$l_r = \sqrt{d^2 + R_a^2}\,; \qquad l_i = \sqrt{d^2 + (R_a + 2R_b)^2}\,, \quad (5.2.6)$$

as shown in Fig. 40(B) and (C). For the condition of $d >> R_a, R_b$, Eqs. (5.2.5) are approximated to

$$\overline{\Psi}_{semi} = \frac{\overline{S}}{2\pi D}\left[\frac{1}{d^2}\exp\left(-\bar{k}_0 d\right)\right]\bar{k}_0 R_b (R_a + R_b) \quad (5.2.7.\text{DC})$$

$$\widetilde{\Psi}_{semi} = \frac{\widetilde{S}}{2\pi D}\left[\frac{1}{d^2}\exp\left(-\widetilde{k}_{amp} d\right)\right]\left[\widetilde{k}_{amp} R_b (R_a + R_b)\right]\sqrt{1 + \left(\frac{\widetilde{k}_{phi}}{\widetilde{k}_{amp}}\right)^2}\,\exp\left\{-i\left[\widetilde{k}_{phi} d - \tan^{-1}\left(\frac{\widetilde{k}_{phi}}{\widetilde{k}_{amp}}\right)\right]\right\} \quad (5.2.7.\text{AC})$$

5.2.2 Solutions in cylindrical-coordinates to FD photon diffusion

5.2.2.A Source and detector in an infinite medium geometry

The cylindrical-coordinate solution to the DC photon fluence rate associated with a source-detector pair in a homogeneous medium of infinite geometry has been solved in Chapter II as

$$\overline{\Psi}_{\inf}(\vec{r}, \vec{r}') = \frac{\overline{S}}{4\pi^2 D}\int_{-\infty}^{\infty} dk\, e^{ik(z-z')} \sum_{m=-\infty}^{\infty} I_m\left(\bar{k}_{eff}\rho_<\right) K_m\left(\bar{k}_{eff}\rho_>\right) e^{im(\varphi-\varphi')} \quad (5.2.8.\text{DC})$$

where I_m and K_m are the modified Bessel functions of the 1st and the 2nd kinds, respectively,

$$\bar{k}_{eff} = \sqrt{k^2 + \bar{k}_0^2}\,, \quad (5.2.9.\text{DC})$$

and $\rho_<$ and $\rho_>$ indicate the smaller and larger radial coordinates of the source and the detector, respectively. Note that the format of $\overline{\Psi}_{\text{inf}}(\vec{r},\vec{r}')$ in Eq. (5.2.8.DC) is slightly different from the corresponding one in Eq. (2.1.13) in Chapter II, in terms of the lower limits of the integration and the summation as well as the number in the denominator to the source term $\overline{S}$, as a result of using exponential terms with complex arguments versus using cosine terms only.

Based on the similarity between the DC and AC counterparts in Eqs. (5.2.1) one would appreciate that the cylindrical-coordinate solution to AC photon fluence rate in a homogeneous medium of infinite geometry must have a form similar to that of Eq. (5.2.8.DC) as

$$\widetilde{\Psi}_{\text{inf}}(\vec{r},\vec{r}') = \frac{\widetilde{S}}{4\pi^2 D}\int_{-\infty}^{\infty} dk\, e^{ik(z-z')} \sum_{m=-\infty}^{\infty} I_m\left(\widetilde{k}_{eff}\rho_<\right) K_m\left(\widetilde{k}_{eff}\rho_>\right) e^{im(\varphi-\varphi')} \quad \text{(5.2.8.AC)}$$

where $$\widetilde{k}_{eff} = \sqrt{k^2 + \widetilde{k}_0^2} \quad \text{(5.2.9.AC)}$$

According to Chapter II and Jackson (Jackson et al., 1998) the cylindrical-coordinates representation of $\overline{\Psi}_{\text{inf}}(\vec{r},\vec{r}')$ in Eq. (5.2.8.DC) and the spherical-coordinates representation of $\overline{\Psi}_{\text{inf}}(\vec{r},\vec{r}')$ in Eq. (5.2.4.DC) are analytically identical. The said identity was also tested numerically in Chapter II. Similarly, we maintain that the cylindrical-coordinates representation of $\widetilde{\Psi}_{\text{inf}}(\vec{r},\vec{r}')$ in Eq. (5.2.8.AC) and the spherical-coordinates representation of $\widetilde{\Psi}_{\text{inf}}(\vec{r},\vec{r}')$ in Eq. (5.2.4.AC) are analytically identical and thereby interchangeable.

5.2.2.B Source and detector on a semi-infinite medium-applicator interface

For completeness, we consider the cylindrical-coordinate solutions to photon diffusion in a homogeneous medium of semi-infinite geometry as that illustrated in Fig. 40(B). Between the radial coordinates of the detector $\vec{r}$ and the "real" isotropic source $\vec{r}'_{real}$ we have $\rho_< = \rho - R_a$ and $\rho_> = \rho$. Between the radial coordinates of the detector $\vec{r}$ and the "image" source $\vec{r}'_{imag}$ we

have $\rho_< = \rho$ and $\rho_> = \rho + R_a + 2R_b$. Based on Eqs. (5.2.5) and the interchangeability of Eqs. (5.2.8) and (5.2.4), the DC photon fluence rate at $\vec{r}$ due to $\vec{r}'_{real}$ and $\vec{r}'_{imag}$ may be expressed by

$$\overline{\Psi}_{semi} = \overline{\Psi}_{real}(\vec{r}, \vec{r}'_{real}) + \overline{\Psi}_{imag}(\vec{r}, \vec{r}'_{imag})$$

$$= \frac{\overline{S}}{4\pi^2 D}\left\{ \int_{-\infty}^{\infty} dk\, e^{ik(z-z'_{real})} \sum_{m=-\infty}^{\infty} I_m\left[\overline{k}_{eff}(\rho - R_a)\right] K_m\left(\overline{k}_{eff}\rho\right) e^{im(\varphi-\varphi'_{real})} \right.$$

$$\left. - \int_{-\infty}^{\infty} dk\, e^{ik(z-z'_{imag})} \sum_{m=-\infty}^{\infty} I_m\left(\overline{k}_{eff}\rho\right) K_m\left[\overline{k}_{eff}(\rho + R_a + 2R_b)\right] e^{im(\varphi-\varphi'_{imag})} \right\} \qquad (5.2.10.DC)$$

and accordingly the AC photon fluence rate by

$$\widetilde{\Psi}_{semi} = \widetilde{\Psi}_{real}(\vec{r}, \vec{r}'_{real}) + \widetilde{\Psi}_{imag}(\vec{r}, \vec{r}'_{imag})$$

$$= \frac{\widetilde{S}}{4\pi^2 D}\left\{ \int_{-\infty}^{\infty} dk\, e^{ik(z-z'_{real})} \sum_{m=-\infty}^{\infty} I_m\left[\widetilde{k}_{eff}(\rho - R_a)\right] K_m\left(\widetilde{k}_{eff}\rho\right) e^{im(\varphi-\varphi'_{real})} \right.$$

$$\left. - \int_{-\infty}^{\infty} dk\, e^{ik(z-z'_{imag})} \sum_{m=-\infty}^{\infty} I_m\left(\widetilde{k}_{eff}\rho\right) K_m\left[\widetilde{k}_{eff}(\rho + R_a + 2R_b)\right] e^{im(\varphi-\varphi'_{imag})} \right\} \qquad (5.2.10.AC)$$

Alternatively, if the semi-infinite geometry is coordinated as the one in Fig. 40(C), we have

$$\overline{\Psi}_{semi} = \frac{\overline{S}}{4\pi^2 D}\left\{ \int_{-\infty}^{\infty} dk\, e^{ik(z-z'_{real})} \sum_{m=-\infty}^{\infty} I_m\left(\overline{k}_{eff}\rho\right) K_m\left[\overline{k}_{eff}(\rho + R_a)\right] e^{im(\varphi-\varphi'_{real})} \right.$$

$$\left. - \int_{-\infty}^{\infty} dk\, e^{ik(z-z'_{imag})} \sum_{m=-\infty}^{\infty} I_m\left[\overline{k}_{eff}(\rho - R_a - 2R_b)\right] K_m\left(\overline{k}_{eff}\rho\right) e^{im(\varphi-\varphi'_{imag})} \right\} \qquad (5.2.10.DC^*)$$

$$\widetilde{\Psi}_{semi} = \frac{\widetilde{S}}{4\pi^2 D}\left\{ \int_{-\infty}^{\infty} dk\, e^{ik(z-z'_{real})} \sum_{m=-\infty}^{\infty} I_m\left(\widetilde{k}_{eff}\rho\right) K_m\left[\widetilde{k}_{eff}(\rho + R_a)\right] e^{im(\varphi-\varphi'_{real})} \right.$$

$$\left. - \int_{-\infty}^{\infty} dk\, e^{ik(z-z'_{imag})} \sum_{m=-\infty}^{\infty} I_m\left[\widetilde{k}_{eff}(\rho - R_a - 2R_b)\right] K_m\left(\widetilde{k}_{eff}\rho\right) e^{im(\varphi-\varphi'_{imag})} \right\} \qquad (5.2.10.AC^*)$$

5.3. Frequency-domain Analysis of Photon Diffusion Associated with "Concave" and "Convex" Geometries of Infinite Longitudinal Dimension

5.3.1 Concave geometry

The "concave" geometry as shown in Fig. 41(A) refers to a diffusive medium ***enclosed*** by an infinitely long cylindrical medium-applicator interface. Given the radius of the cylinder as R_0, a detector $\vec{r}$ on the medium-applicator interface locates at (R_0, φ, z), and a directional source $\vec{r}'$ on the medium-applicator interface locates at (R_0, φ', z'). Based on the symmetry of the concave geometry, the directional source $\vec{r}'$ is to be modeled by a "real" isotropic source $\vec{r}'_{real}$ located along the radial direction of the physical source and inwardly at a distance of $R_a = 1/\mu_s'$, i.e. at $(R_0 - R_a, \varphi', z')$. The extrapolated boundary is concentric with and at a radial distance of $R_b = 2AD$ away from the physical boundary. Apparently as the radius R_0 reaches infinity the photon fluence rate associated with a source-detector pair on the medium-applicator interface of the concave geometry approaches that on the associated semi-infinite interface that is tangential to the concave interface at the source position, for the same source-detector distance. This characteristic serves as both the qualitative and quantitative calibers of the analytic solutions derived for the concave geometry.

Considering that Eqs. (5.2.8.DC) and (5.2.8.AC) are identical in their analytical forms except for the notations differentiating "DC" and "AC", the cylindrical-coordinates solutions to FD photon diffusion associated with optodes on the concave medium-applicator interface can be derived by following the approaches to the corresponding CW photon diffusion demonstrated in Chapter II. The resulted DC photon fluence rate sensed by the detector $\vec{r}$ on the physical boundary of the concave geometry due to the physical source $\vec{r}'$ is

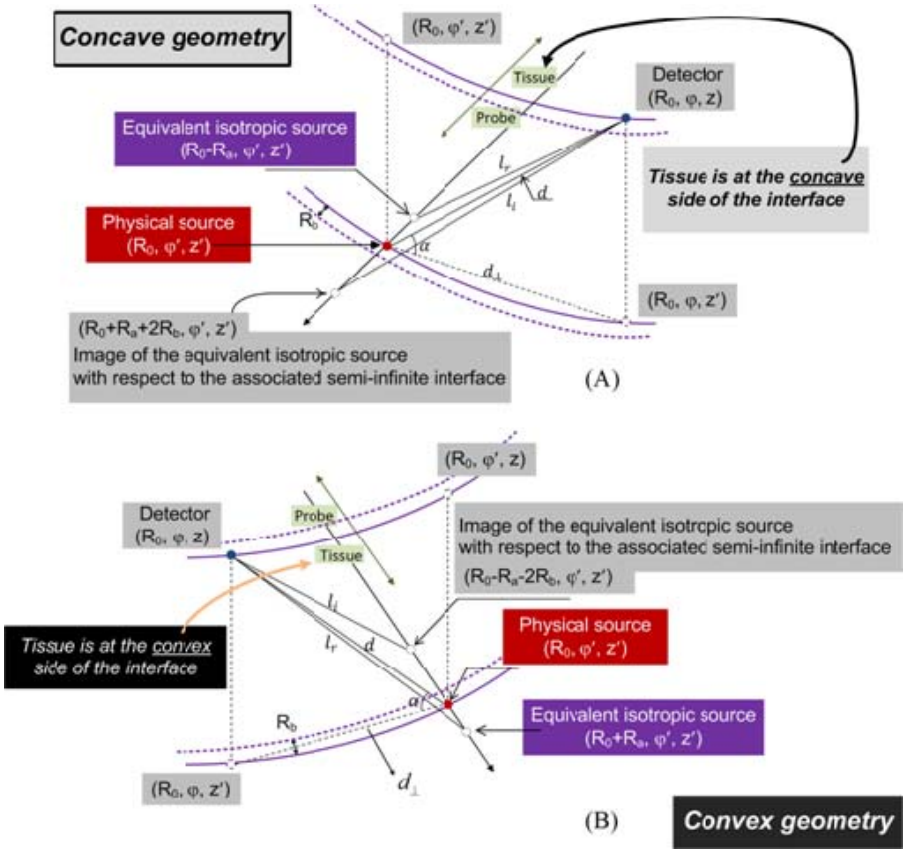

Fig. 41 The configurations of concave geometry (A) and convex geometry (B). The physical directional source and detector locate at the probe-tissue interface at (R_0, φ', z') and (R_0, φ, z) respectively. In concave geometry, the equivalent isotropic source locates inwardly at $(R_0 - R_a, \varphi', z')$. The image of the source with respect to the associated semi-infinite geometry locates at $(R_0 + R_a + 2R_b, \varphi', z')$. In convex geometry, the equivalent isotropic source locates inwardly at $(R_0 + R_a, \varphi', z')$. The image of the source with respect to the associated semi-infinite geometry locates at $(R_0 - R_a - 2R_b, \varphi', z')$.

$$\overline{\Psi}_{conC} = \frac{\overline{S}}{4\pi^2 D}\int_{-\infty}^{\infty} dk \left\{ \exp\left[ik(z-z')\right] \sum_{m=-\infty}^{\infty} I_m\left[\overline{k}_{eff}(R_0 - R_a)\right] K_m\left(\overline{k}_{eff} R_0\right)\right.$$

$$\left\langle 1-\frac{I_m\left(\bar{k}_{eff}R_0\right)}{K_m\left(\bar{k}_{eff}R_0\right)}\frac{K_m\left[\bar{k}_{eff}\left(R_0+R_b\right)\right]}{I_m\left[\bar{k}_{eff}\left(R_0+R_b\right)\right]}\right\rangle \exp\left[im\left(\varphi-\varphi'\right)\right]\Bigg\} \qquad (5.3.1.DC)$$

which has a slightly different format comparing to Eq. (2.2.5) in Chapter II, and its AC counterpart is

$$\tilde{\Psi}_{conC}=\frac{\tilde{S}}{4\pi^2 D}\int_{-\infty}^{\infty}dk\Bigg\{\exp\left[ik\left(z-z'\right)\right]\sum_{m=-\infty}^{\infty}I_m\left[\tilde{k}_{eff}\left(R_0-R_a\right)\right]K_m\left(\tilde{k}_{eff}R_0\right)$$

$$\left\langle 1-\frac{I_m\left(\tilde{k}_{eff}R_0\right)}{K_m\left(\tilde{k}_{eff}R_0\right)}\frac{K_m\left[\tilde{k}_{eff}\left(R_0+R_b\right)\right]}{I_m\left[\tilde{k}_{eff}\left(R_0+R_b\right)\right]}\right\rangle \exp\left[im\left(\varphi-\varphi'\right)\right]\Bigg\} \qquad (5.3.1.AC)$$

5.3.2 Convex geometry

The "convex" geometry as shown in Fig. 41(B) refers to a diffusive medium ***enclosing*** an infinitely long cylindrical medium-applicator interface. Given the radius of the cylinder as R_0, a detector $\vec{r}$ on the medium-applicator interface locates at (R_0,φ,z), and a directional source $\vec{r}\,'$ on the medium-applicator interface locates at (R_0,φ',z'). Based on the symmetry of the convex geometry, the directional source $\vec{r}$ is to be modeled by a "real" isotropic source $\vec{r}\,'_{real}$ located along the radial direction of the physical source and outwardly at a distance of $R_a=1/\mu_s'$, i.e. at (R_0+R_a,φ',z'). The extrapolated boundary is concentric with and at a radial distance of $R_b=2AD$ inward from the physical boundary. Apparently as the radius R_0 reaches infinity the photon fluence rate associated with a source-detector pair on the medium-applicator interface of the convex geometry approaches that on the associated semi-infinite geometry interface that is tangential to the convex interface at the source position, for the same source-detector distance. This characteristic serves as both the qualitative and quantitative calibers of the analytic solutions derived for the concave geometry.

Considering again that Eqs. (5.2.8.DC) and (5.2.8.AC) are identical in their analytical forms except for the notations differentiating "DC" and "AC", the cylindrical-coordinates solutions to FD photon diffusion associated with optodes on the convex medium-applicator interface can be derived by following the approaches to the corresponding CW photon diffusion demonstrated in Chapter II. The resulted DC photon fluence rate sensed by the detector $\vec{r}$ on the physical boundary of the convex geometry due to the physical source $\vec{r}'$ is

$$\overline{\Psi}_{conV} = \overline{\Psi}_{real}\Big|_{phys} + \overline{\Psi}_{imag}\Big|_{phys} = \frac{\overline{S}}{4\pi^2 D}\int_{-\infty}^{\infty} dk \Bigg\{ \exp\left[ik\left(z-z'\right)\right] \sum_{m=-\infty}^{\infty} I_m\left(\overline{k}_{eff} R_0\right) K_m\left[\overline{k}_{eff}\left(R_0 + R_a\right)\right] \Bigg\langle 1 - \frac{K_m\left(\overline{k}_{eff} R_0\right)}{I_m\left(\overline{k}_{eff} R_0\right)} \frac{I_m\left[\overline{k}_{eff}\left(R_0 - R_b\right)\right]}{K_m\left[\overline{k}_{eff}\left(R_0 - R_b\right)\right]} \Bigg\rangle \exp\left[im\left(\varphi - \varphi'\right)\right] \Bigg\} \quad (5.3.2.DC)$$

which has a slightly different format comparing to Eq. (2.2.17) in Chapter II, and its AC counterpart is

$$\widetilde{\Psi}_{conV} = \widetilde{\Psi}_{real}\Big|_{phys} + \widetilde{\Psi}_{imag}\Big|_{phys} = \frac{\widetilde{S}}{4\pi^2 D}\int_{-\infty}^{\infty} dk \Bigg\{ \exp\left[ik\left(z-z'\right)\right] \sum_{m=-\infty}^{\infty} I_m\left(\widetilde{k}_{eff} R_0\right) K_m\left[\widetilde{k}_{eff}\left(R_0 + R_a\right)\right] \Bigg\langle 1 - \frac{K_m\left(\widetilde{k}_{eff} R_0\right)}{I_m\left(\widetilde{k}_{eff} R_0\right)} \frac{I_m\left[\widetilde{k}_{eff}\left(R_0 - R_b\right)\right]}{K_m\left[\widetilde{k}_{eff}\left(R_0 - R_b\right)\right]} \Bigg\rangle \exp\left[im\left(\varphi - \varphi'\right)\right] \Bigg\} \quad (5.3.2.AC)$$

5.4 Analytical Prediction of the Characteristics of Frequency-domain Photon Diffusion versus Source-detector Distance in Concave and Convex Geometries of Large Radius

To understand the generalized behavior of the FD photon diffusion versus source-detector distance in concave and convex geometries, we now consider that the radius of the concave or convex geometry is much greater than the source-detector distance that is also in the diffusion regime, i.e., we have assumed that $R_0 >> d >> R_a, R_b$. By using the spherical coordinate expression of the photon fluence rates given in Eqs. (5.2.5), we can rewrite Eqs. (5.3.1) for concave geometry (refer to Section 2.2.1 in Chapter II for the analytical means) as

$$\overline{\Psi}_{conC}=\left[\frac{\overline{S}}{4\pi Dl_r}\exp\left(-\bar{k}_0 l_r\right)\right]-\left[\frac{\overline{S}}{4\pi Dl_i}\exp\left(-\bar{k}_0 l_i\right)\right]\sqrt{\frac{R_0+R_a+2R_b}{R_0-R_a}} \tag{5.4.1.DC}$$

$$\widetilde{\Psi}_{conC}=\left[\frac{\widetilde{S}}{4\pi Dl_r}\exp\left(-\widetilde{k}_{amp}l_r\right)\right]\exp\left(-i\widetilde{k}_{phi}l_r\right)-\left[\frac{\widetilde{S}}{4\pi Dl_i}\exp\left(-\widetilde{k}_{amp}l_i\right)\right]\sqrt{\frac{R_0+R_a+2R_b}{R_0-R_a}}\exp\left(-i\widetilde{k}_{phi}l_i\right) \tag{5.4.1.AC}$$

The acute angle formed by $\left(\vec{r}-\vec{r}'\right)$ and the azimuthal plane is α as shown in Fig. 41(A), and

$$l_r=d\sqrt{\left[1+\frac{R_a^2}{d^2}-\frac{R_a}{R_0}\left(\cos\alpha\right)^2\right]};\qquad l_i=d\sqrt{\left[1+\frac{\left(R_a+2R_b\right)^2}{d^2}+\frac{R_a+2R_b}{R_0}\left(\cos\alpha\right)^2\right]} \tag{5.4.2}$$

then based on the approach demonstrated in Chapter IV, the DC and AC photon fluence rates expressed by Eqs. (5.4.1) can be simplified to

$$\overline{\Psi}_{conC}=\frac{\overline{S}}{2\pi D}\frac{1}{d^2}\exp\left\{-\left[\bar{k}_0 d+\frac{d}{2\bar{k}_0R_b\left(R_0-R_a\right)}-\frac{2R_0-R_a+2R_b}{4R_0R_b\left(R_0-R_a\right)}\left(\cos\alpha\right)^2d^2\right]\right\}\exp\left[\frac{\left(R_0+2R_b\right)^2}{4R_b\left(R_0-R_a\right)}\right]\left[\bar{k}_0R_b\left(R_a+R_b\right)\right] \tag{5.4.3.DC}$$

$$\widetilde{\Psi}_{conC}=\frac{\widetilde{S}}{2\pi D}\frac{1}{d^2}\exp\left\{-\left[\widetilde{k}_{amp}d+\frac{\widetilde{k}_{amp}d}{2\left(\widetilde{k}_{amp}^2+\widetilde{k}_{phi}^2\right)R_b\left(R_0-R_a\right)}-\frac{2R_0-R_a+2R_b}{4R_0R_b\left(R_0-R_a\right)}\left(\cos\alpha\right)^2d^2\right]\right\}\exp\left[\frac{\left(R_0+2R_b\right)^2}{4R_b\left(R_0-R_a\right)}\right]$$
$$\left[\sqrt{\widetilde{k}_{amp}^2+\widetilde{k}_{phi}^2}R_b\left(R_a+R_b\right)\right]\exp\left\{-i\left[\widetilde{k}_{phi}d-\frac{\widetilde{k}_{phi}d}{2\left(\widetilde{k}_{amp}^2+\widetilde{k}_{phi}^2\right)R_b\left(R_0-R_a\right)}-\tan^{-1}\left(\frac{\widetilde{k}_{phi}}{\widetilde{k}_{amp}}\right)\right]\right\} \tag{5.4.3.AC}$$

Similarly, we can rewrite Eqs. (5.3.2) for convex geometry (refer to Section 2.2.2 in Chapter II) as

$$\overline{\Psi}_{conV}=\left[\frac{\overline{S}}{4\pi Dl_r}\exp\left(-\bar{k}_0 l_r\right)\right]-\left[\frac{\overline{S}}{4\pi Dl_i}\exp\left(-\bar{k}_0 l_i\right)\right]\sqrt{\frac{R_0-R_a-2R_b}{R_0+R_a}} \tag{5.4.4.DC}$$

$$\widetilde{\Psi}_{conV}=\left[\frac{\widetilde{S}}{4\pi Dl_r}\exp\left(-\widetilde{k}_{amp}l_r\right)\right]\exp\left(-i\widetilde{k}_{phi}l_r\right)-\left[\frac{\widetilde{S}}{4\pi Dl_i}\exp\left(-\widetilde{k}_{amp}l_i\right)\right]\sqrt{\frac{R_0-R_a-2R_b}{R_0+R_a}}\exp\left(-i\widetilde{k}_{phi}l_i\right)$$
(5.4.4.AC)

Utilizing the acute angle α between $\left(\vec{r}-\vec{r}'\right)$ and the azimuthal plane as shown in Fig. 41(B), and

$$l_r=d\sqrt{\left[1+\frac{R_a^2}{d^2}+\frac{R_a}{R_0}\left(\cos\alpha\right)^2\right]};\ l_i=d\sqrt{\left[1+\frac{\left(R_a+2R_b\right)^2}{d^2}-\frac{R_a+2R_b}{R_0}\left(\cos\alpha\right)^2\right]} \tag{5.4.5}$$

the DC and AC photon fluence rates expressed by Eqs. (5.4.4) can be simplified to

$$\overline{\Psi}_{conV}=\frac{\bar{S}}{2\pi D}\frac{1}{d^2}\exp\left\{-\left[\bar{k}_0 d-\frac{d}{2\bar{k}_0 R_b\left(R_0+R_a\right)}+\frac{2R_0+R_a-2R_b}{4R_0R_b\left(R_0+R_a\right)}(\cos\alpha)^2 d^2\right]\right\}\exp\left[-\frac{\left(R_0+2R_b\right)^2}{4R_b\left(R_0+R_a\right)}\right]\left[\bar{k}_0 R_b(R_a+R_b)\right] \quad (5.4.6.DC)$$

$$\widetilde{\Psi}_{conV}=\frac{\widetilde{S}}{2\pi D}\frac{1}{d^2}\exp\left\{-\left[\widetilde{k}_{amp} d-\frac{\widetilde{k}_{amp} d}{2\left(\widetilde{k}_{amp}^2+\widetilde{k}_{phi}^2\right)R_b\left(R_0+R_a\right)}+\frac{2R_0+R_a-2R_b}{4R_0R_b\left(R_0+R_a\right)}(\cos\alpha)^2 d^2\right]\right\}\exp\left[-\frac{\left(R_0+2R_b\right)^2}{4R_b\left(R_0+R_a\right)}\right]$$
$$\left[\sqrt{\widetilde{k}_{amp}^2+\widetilde{k}_{phi}^2}R_b(R_a+R_b)\right]\exp\left\{-i\left[\widetilde{k}_{phi} d+\frac{\widetilde{k}_{phi} d}{2\left(\widetilde{k}_{amp}^2+\widetilde{k}_{phi}^2\right)R_b\left(R_0+R_a\right)}-\tan^{-1}\left(\frac{\widetilde{k}_{phi}}{\widetilde{k}_{amp}}\right)\right]\right\} \quad (5.4.6.AC)$$

Note that Eqs. (5.4.1)-(5.4.6) are formulated under the condition of $R_0 >> d >> R_a, R_b$, and with which we generalize the behavior of FD photon diffusion, in terms of the changes of DC and AC photon fluence rates with respect to the source-detector distance $d=\left|\vec{r}-\vec{r}'\right|$, in a homogeneous medium of infinite geometry as well as on the semi-infinite, concave, and convex medium-applicator interfaces bounding a homogeneous medium. The characteristics given in below are derived from the base equations of Eqs. (5.2.4) for infinite geometry, Eqs. (5.2.7) for semi-infinite geometry, Eqs. (5.4.3) for concave geometry, and Eqs, (5.4.6) for convex geometry.

5.4.1 The change of DC photon fluence rate with respect to d (recounting)

5.4.1.A Source and detector in an infinite medium geometry

In an infinite medium geometry, we have $\ln\left(\overline{\Psi}_{\inf} d\right)$ reducing versus *d* at a rate of $\bar{k}_0$ as

$$\frac{\partial\ln\left(\overline{\Psi}_{\inf} d\right)}{\partial d}=-\bar{k}_0 \quad (5.4.7.DC.infi)$$

5.4.1.B Source and detector on a semi-infinite medium-applicator interface

On a semi-infinite interface, we have $\ln\left(\overline{\Psi}_{semi} d^2\right)$ reducing versus *d* at a rate of $\bar{k}_0$ as

$$\frac{\partial\ln\left(\overline{\Psi}_{semi} d^2\right)}{\partial d}=-\bar{k}_0 \quad (5.4.7.DC.semi)$$

5.4.1.C Source and detector on a concave medium-applicator interface with large radius

On a concave interface with larger radius, we have $\ln\left(\overline{\Psi}_{conC} d^2\right)$ reducing versus d as (presented in Chapter IV)

$$\frac{\partial \ln\left(\overline{\Psi}_{conC} d^2\right)}{\partial d} = -\left\{ \bar{k}_0 + \frac{1}{2\bar{k}_0 R_b \left(R_0 - R_a\right)} - \left[\frac{2R_0 - R_a + 2R_b}{2R_0 R_b \left(R_0 - R_a\right)} \right] \cos\alpha \, d_\perp \right\} \quad \text{(5.4.7.DC.conC)}$$

where $d_\perp = d\cos\alpha$ is the projection of d to the azimuthal plane. Along the longitudinal direction, termed *case-longi*, i.e., $\cos\alpha = 0$, we have

$$\left.\frac{\partial \ln\left(\overline{\Psi}_{conC} d^2\right)}{\partial d}\right|_{longi} = -\left[\bar{k}_0 + \frac{1}{2\bar{k}_0 R_b \left(R_0 - R_a\right)} \right] \quad \text{(5.4.7.DC.conC.longi)}$$

Equation (5.4.7.DC.conC.longi) indicates that when the source and detector are positioned only along the longitudinal direction, $\ln\left(\overline{\Psi}_{conC} d^2\right)$ reduces versus d at a rate greater than $\bar{k}_0$. Along the azimuthal direction, termed *case-azi*, i.e., $\cos\alpha = 1$, $d_\perp = d$, we have

$$\left.\frac{\partial \ln\left(\overline{\Psi}_{conC} d^2\right)}{\partial d}\right|_{azi} = -\left\{ \bar{k}_0 + \frac{1}{2\bar{k}_0 R_b \left(R_0 - R_a\right)} - \left[\frac{2R_0 - R_a + 2R_b}{2R_0 R_b \left(R_0 - R_a\right)} \right] d \right\} \quad \text{(5.4.7.DC.conC.azi)}$$

It can be demonstrated that the rate of the reduction of $\ln\left(\overline{\Psi}_{conC} d^2\right)$ in Eq. (5.4.7.DC.conC.azi) versus d is actually smaller than $\bar{k}_0$. We also have from Eq. (5.4.7.DC.conC) that when the source and detector are positioned along a set of spiral paths defined by the following relationship

$$\cos\bar{\alpha}_{conC} = \frac{1}{\bar{k}_0 d_\perp} \frac{R_0}{2R_0 - R_a + 2R_b} \quad \text{(5.4.7.DC.conC.spiral),}$$

$\ln\left(\overline{\Psi}_{conC} d^2\right)$ reduces versus d at a rate of $\bar{k}_0$, i.e., identical to the rate when evaluated along a straight-line on a semi-infinite medium-applicator interface.

5.4.1.D Source and detector on a convex medium-applicator interface with large radius

On a convex interface with large radius, we have $\ln\left(\overline{\Psi}_{conV} d^2\right)$ reducing versus d as (presented in Chapter IV)

$$\frac{\partial \ln\left(\overline{\Psi}_{conV} d^2\right)}{\partial d} = -\left\{ \bar{k}_0 - \frac{1}{2\bar{k}_0 R_b \left(R_0 + R_a\right)} + \left[\frac{2R_0 + R_a - 2R_b}{2R_0 R_b \left(R_0 + R_a\right)} \right] \cos\alpha \, d_\perp \right\} \quad \text{(5.4.7.DC.conV)}$$

Along the longitudinal direction as in *case-longi*, i.e., $\cos\alpha = 0$, we have

$$\left.\frac{\partial \ln\left(\overline{\Psi}_{conV} d^2\right)}{\partial d}\right|_{longi} = -\left[\bar{k}_0 - \frac{1}{2\bar{k}_0 R_b \left(R_0 + R_a\right)} \right] \quad \text{(5.4.7.DC.conV.longi)}$$

Equation (5.4.7.DC.conV.longi) indicates that when the source and detector are positioned only along the longitudinal direction, $\ln\left(\overline{\Psi}_{conV} d^2\right)$ reduces versus d at a rate smaller than $\bar{k}_0$. Along the azimuthal direction as in *case-azi*, i.e., $\cos\alpha = 1$, $d_\perp = d$, we have

$$\left.\frac{\partial \ln\left(\overline{\Psi}_{conV} d^2\right)}{\partial d}\right|_{azi} = -\left\{ \bar{k}_0 - \frac{1}{2\bar{k}_0 R_b \left(R_0 + R_a\right)} + \left[\frac{2R_0 + R_a - 2R_b}{2R_0 R_b \left(R_0 + R_a\right)} \right] d \right\} \quad \text{(5.4.7.DC.conV.azi)}$$

It can be demonstrated that the rate of the reduction of $\ln\left(\overline{\Psi}_{conV} d^2\right)$ in Eq. (5.4.7.DC.conV.azi) versus d is actually greater than $\bar{k}_0$. We also have from Eq. (5.4.7.DC.conV) that when the source and detector are positioned along a set of spiral paths defined by the following relationship

$$\cos\bar{\alpha}_{conV} = \frac{1}{\bar{k}_0 d_\perp} \frac{R_0}{2R_0 + R_a - 2R_b} \quad \text{(5.4.7.DC.conV.spiral),}$$

$\ln\left(\overline{\Psi}_{conV} d^2\right)$ reduces versus d at a rate of $\bar{k}_0$, i.e., identical to the rate when evaluated along a straight-line on a semi-infinite medium-applicator interface.

5.4.2 The change of the amplitude of AC photon fluence rate with respect to d

5.4.2.A Source and detector in an infinite medium geometry

In an infinite geometry, we have $\ln\left(\left|\widetilde{\Psi}_{\inf}\right| d\right)$ reducing versus d at a rate of $\widetilde{k}_{amp}$ as

$$\frac{\partial \ln\left(\left|\widetilde{\Psi}_{\inf}\right| d\right)}{\partial d} = -\widetilde{k}_{amp} \qquad \text{(5.4.7.AC.infi)}$$

5.4.2.B Source and detector on a semi-infinite medium-applicator interface

On a semi-infinite interface, we have $\ln\left(\left|\widetilde{\Psi}_{semi}\right| d^2\right)$ reducing versus d at a rate of $\widetilde{k}_{amp}$ as

$$\frac{\partial \ln\left(\left|\widetilde{\Psi}_{semi}\right| d^2\right)}{\partial d} = -\widetilde{k}_{amp} \qquad \text{(5.4.7.AC.semi)}$$

5.4.2.C Source and detector on a concave medium-applicator interface with large radius

On a concave interface with large radius, we have $\ln\left(\left|\widetilde{\Psi}_{conC}\right| d^2\right)$ reducing versus d as

$$\frac{\partial \ln\left(\left|\widetilde{\Psi}_{conC}\right| d^2\right)}{\partial d} = -\left\{\widetilde{k}_{amp} + \frac{\widetilde{k}_{amp}}{2\left(\widetilde{k}_{amp}^2 + \widetilde{k}_{phi}^2\right) R_b\left(R_0 - R_a\right)} - \left[\frac{2R_0 - R_a + 2R_b}{2R_0 R_b\left(R_0 - R_a\right)}\right] \cos\alpha \, d_\perp \right\} \qquad \text{(5.4.7.AC.conC)}$$

Along the longitudinal direction as in *case-longi*, i.e., $\cos\alpha = 0$, we have

$$\left.\frac{\partial \ln\left(\left|\widetilde{\Psi}_{conC}\right| d^2\right)}{\partial d}\right|_{longi} = -\left[\widetilde{k}_{amp} + \frac{\widetilde{k}_{amp}}{2\left(\widetilde{k}_{amp}^2 + \widetilde{k}_{phi}^2\right) R_b\left(R_0 - R_a\right)}\right] \qquad \text{(5.4.7.AC.conC.longi)}$$

Equation (5.4.7.AC.conC.longi) indicates that when the source and detector are positioned only along the longitudinal direction, $\ln\left(\left|\widetilde{\Psi}_{conC}\right| d^2\right)$ reduces versus d at a rate greater than $\widetilde{k}_{amp}$. Along the azimuthal direction as in *case-azi*, i.e., $\cos\alpha = 1$, $d_\perp = d$, we have

$$\left.\frac{\partial \ln\left(\left|\widetilde{\Psi}_{conC}\right| d^2\right)}{\partial d}\right|_{azi} = -\left\{\widetilde{k}_{amp} + \frac{\widetilde{k}_{amp}}{2\left(\widetilde{k}_{amp}^2 + \widetilde{k}_{phi}^2\right) R_b\left(R_0 - R_a\right)} - \left[\frac{2R_0 - R_a + 2R_b}{2R_0 R_b\left(R_0 - R_a\right)}\right] d \right\} \qquad \text{(5.4.7.AC.conC.azi)}$$

It can be demonstrated that the rate of the reduction of $\ln\left(\left|\widetilde{\Psi}_{conC}\right|d^2\right)$ in Eq. (4.AC.conC.azi) versus *d* is actually smaller than $\widetilde{k}_{amp}$. We also have from Eq. (4.AC.conC) that when the source and detector are positioned along a set of spiral paths defined by the following relationship

$$\cos\widetilde{\alpha}_{conC}=\frac{\widetilde{k}_{amp}}{\left(\widetilde{k}_{amp}^2+\widetilde{k}_{phi}^2\right)d_\perp}\frac{R_0}{2R_0-R_a+2R_b} \qquad \text{(5.4.7.AC.conC.spiral)},$$

$\ln\left(\left|\widetilde{\Psi}_{conC}\right|d^2\right)$ reduces versus *d* at a rate of $\widetilde{k}_{amp}$, i.e., identical to the rate when evaluated along a straight-line on a semi-infinite medium-applicator interface. Comparison of Eq. (5.4.7.AC.conC.spiral) with Eq. (4.DC.conC.spiral), however, reveals that the spiral paths associated with the amplitude of AC photon fluence rate should differ from that associated with DC photon fluence rate, and the difference should decrease as the modulation frequency decreases.

5.4.2.D. Source and detector on a convex medium-applicator interface with large radius

On a convex interface with large radius, we have $\ln\left(\left|\widetilde{\Psi}_{conV}\right|d^2\right)$ reducing versus *d* as

$$\frac{\partial\ln\left(\left|\widetilde{\Psi}_{conV}\right|d^2\right)}{\partial d}=-\left\{\widetilde{k}_{amp}-\frac{\widetilde{k}_{amp}}{2\left(\widetilde{k}_{amp}^2+\widetilde{k}_{phi}^2\right)R_b\left(R_0+R_a\right)}+\left[\frac{2R_0+R_a-2R_b}{2R_0R_b\left(R_0+R_a\right)}\right]\cos\alpha\, d_\perp\right\} \quad \text{(5.4.7.AC.conV)}$$

Along the longitudinal direction as in *case-longi*, i.e., $\cos\alpha=0$, we have

$$\left.\frac{\partial\ln\left(\left|\widetilde{\Psi}_{conV}\right|d^2\right)}{\partial d}\right|_{longi}=-\left[\widetilde{k}_{amp}-\frac{\widetilde{k}_{amp}}{2\left(\widetilde{k}_{amp}^2+\widetilde{k}_{phi}^2\right)R_b\left(R_0+R_a\right)}\right] \qquad \text{(5.4.7.AC.conV.longi)}$$

Equation (5.4.7.AC.conV.longi) indicates that when the source and detector are positioned only along the longitudinal direction, $\ln\left(\left|\widetilde{\Psi}_{conV}\right|d^2\right)$ reduces versus *d* at a rate smaller than $\widetilde{k}_{amp}$. Along the azimuthal direction as in *case-azi*, i.e., $\cos\alpha=1$, $d_\perp=d$, we have

$$\left.\frac{\partial \ln\left(\left|\tilde{\Psi}_{conV}\right| d^2\right)}{\partial d}\right|_{azi} = -\left\{\tilde{k}_{amp} - \frac{\tilde{k}_{amp}}{2\left(\tilde{k}_{amp}^2 + \tilde{k}_{phi}^2\right) R_b\left(R_0 + R_a\right)} + \left[\frac{2R_0 + R_a - 2R_b}{2R_0 R_b\left(R_0 + R_a\right)}\right] d\right\} \quad \text{(5.4.7.AC.conV.azi)}$$

It can be demonstrated that the rate of the reduction of $\ln\left(\left|\tilde{\Psi}_{conV}\right| d^2\right)$ in Eq. (5.4.7.AC.conV.azi) versus *d* is actually greater than $\tilde{k}_{amp}$. We also have from Eq. (5.4.7.AC.conV) that when the source and detector are positioned along a set of spiral paths defined by the following relationship

$$\cos\tilde{\alpha}_{conV} = \frac{\tilde{k}_{amp}}{\left(\tilde{k}_{amp}^2 + \tilde{k}_{phi}^2\right) d_\perp} \frac{R_0}{2R_0 + R_a - 2R_b} \quad \text{(5.4.7.AC.conV.spiral),}$$

$\ln\left(\left|\tilde{\Psi}_{conV}\right| d^2\right)$ reduces versus *d* at a rate of $\tilde{k}_{amp}$, i.e., identical to the rate when evaluated along a straight-line on a semi-infinite medium-applicator interface. Comparison of Eq. (5.4.7.AC.conV.spiral) with Eq. (5.4.7.DC.conV.spiral) also reveals that the spiral paths associated with the amplitude of AC photon fluence rate should differ from that associated with DC photon fluence rate, and the difference should decrease as the modulation frequency decreases.

5.4.3 The change of modulation-depth of photon fluence rate with respect to d

We evaluate the modulation-depth $Mod = \left|\tilde{\Psi}\right| / \overline{\Psi}$, which is the ratio of the amplitude of AC photon fluence rate to the DC photon fluence rate.

5.4.3.A Source and detector in an infinite medium geometry

In an infinite geometry, we have $\ln\left(Mod_{\inf}\right)$ reducing versus *d* at a rate of $\left(\tilde{k}_{amp} - \bar{k}_0\right)$ as

$$\frac{\partial\left[\ln\left(Mod_{\inf}\right)\right]}{\partial d} = -\left(\tilde{k}_{amp} - \bar{k}_0\right) \quad \text{(5.4.7.Mod.infi)}$$

5.4.3.B Source and detector on a semi-infinite medium-applicator interface

On a semi-infinite interface, we have $\ln(Mod_{semi})$ reducing versus *d* at a rate of $(\tilde{k}_{amp} - \bar{k}_0)$ as

$$\frac{\partial[\ln(Mod_{semi})]}{\partial d} = -(\tilde{k}_{amp} - \bar{k}_0) \qquad \text{(5.4.7.Mod.semi)}$$

5.4.3.C Source and detector on a concave medium-applicator interface with large radius

On a concave interface with large radius, we have $\ln(Mod_{conC})$ reducing versus *d* as

$$\frac{\partial[\ln(Mod_{conC})]}{\partial d} = -\left\{(\tilde{k}_{amp} - \bar{k}_0) - \frac{1}{2R_b(R_0 - R_a)}\left[\frac{1}{\bar{k}_0} - \frac{\tilde{k}_{amp}}{\tilde{k}_{amp}^2 + \tilde{k}_{phi}^2}\right]\right\}$$

(5.4.7.Mod.conC)

for both case-longi and case-azi. Since $\tilde{k}_{amp} > \bar{k}_0 > 0$, $\ln(Mod_{conC})$ reduces versus *d* at a rate smaller than $(\tilde{k}_{amp} - \bar{k}_0)$, and the higher the modulation frequency is, the bigger the difference becomes with respect to $(\tilde{k}_{amp} - \bar{k}_0)$. Thus on the concave medium-applicator interface there isn't any spiral-paths inferred for the decay rate of modulation frequency.

5.4.3.D Source and detector on a convex medium-applicator interface with large radius

On a convex interface with large radius, we have $\ln(Mod_{conV})$ reducing versus *d* as

$$\frac{\partial[\ln(Mod_{conV})]}{\partial d} = -\left\{(\tilde{k}_{amp} - \bar{k}_0) + \frac{1}{2R_b(R_0 + R_a)}\left[\frac{1}{\bar{k}_0} - \frac{\tilde{k}_{amp}}{\tilde{k}_{amp}^2 + \tilde{k}_{phi}^2}\right]\right\} \text{(5.4.7.Mod.conV)}$$

for both case-longi and case-azi. Since $\tilde{k}_{amp} > \bar{k}_0 > 0$, the $\ln(Mod_{conV})$ recues versus *d* at a rate greater than $(\tilde{k}_{amp} - \bar{k}_0)$, and the higher the modulation frequency is, the bigger the difference becomes with respect to $(\tilde{k}_{amp} - \bar{k}_0)$. Thus on the convex medium-applicator interface there isn't any spiral-paths inferred for the decay rate of modulation frequency.

5.4.4 The change of phase of AC photon fluence rate with respect to d

5.4.4.A Source and detector in an infinite medium geometry

In an infinite geometry, the phase value $\left|\angle\tilde{\Psi}_{\inf}\right|$ increases versus *d* at a rate of $\tilde{k}_{phi}$ as

$$\frac{\partial\left|\angle\tilde{\Psi}_{\inf}\right|}{\partial d}=\tilde{k}_{phi} \tag{5.4.7.Phi.infi}$$

5.4.4.B. Source and detector on a semi-infinite medium-applicator interface

On a semi-infinite interface, the phase value $\left|\angle\tilde{\Psi}_{semi}\right|$ increases versus *d* as

$$\frac{\partial\left|\angle\tilde{\Psi}_{semi}\right|}{\partial d}=\tilde{k}_{phi} \tag{5.4.7.Phi.semi}$$

5.4.4.C. Source and detector on a concave medium-applicator interface with large radius

On a concave interface with large radius, the phase value $\left|\angle\tilde{\Psi}_{conC}\right|$ increases versus *d* as

$$\frac{\partial\left|\angle\Psi_{conC}\right|}{\partial d}=\tilde{k}_{phi}-\frac{\tilde{k}_{phi}}{2\left(\tilde{k}_{amp}^2+\tilde{k}_{phi}^2\right)R_b\left(R_0-R_a\right)} \tag{5.4.7.Phi.conC}$$

for both case-longi and case-azi. From Eq. (5.4.7.Phi.conC), $\left|\angle\tilde{\Psi}_{conC}\right|$ increases versus *d* at a rate smaller than $\tilde{k}_{phi}$, and the greater the modulation frequency is, the bigger the difference becomes with respect to $\tilde{k}_{phi}$. Thus on the concave medium-applicator interface there is no spiral-paths inferred for the phase changing rate of the AC photon fluence rate.

5.4.4.D. Source and detector on a convex medium-applicator interface with large radius

On a concave interface with large radius, the phase value $\left|\angle\tilde{\Psi}_{conV}\right|$ increases versus *d* as

$$\frac{\partial\left|\angle\Psi_{conV}\right|}{\partial d}=\widetilde{k}_{phi}+\frac{\widetilde{k}_{phi}}{2\left(\widetilde{k}_{amp}^{2}+\widetilde{k}_{phi}^{2}\right)R_b\left(R_0+R_a\right)} \qquad \text{(5.4.7.Phi.conV)}$$

for both case-longi and case-azi. From Eq. (5.4.7.Phi.conV), $\left|\angle\widetilde{\Psi}_{conV}\right|$ increases versus *d* at a rate greater than $\widetilde{k}_{phi}$, and the greater the modulation frequency is, the bigger the difference becomes with respect to $\widetilde{k}_{phi}$. Thus on the convex medium-applicator interface there is no spiral-paths inferred for the phase changing rate of the AC photon fluence rate.

The above predictions based on analytical approximations are tabulated in table 5. The influence of the shape of the medium-applicator interface on FD photon diffusion when compared with semi-infinite geometry is explicitly shown.

5.5 Numerical Evaluation of the Characteristics of Frequency-domain Photon Diffusion versus Source-detector Distance in Concave and Convex Geometries of Small Radius

The previous section has indicated the general behaviors of FD photon diffusion between a source and a detector aligned azimuthally or longitudinally on a concave or convex medium-applicator interface. Although the predictions are made for concave or convex geometry of very large radius, the qualitative patterns of FD photon diffusion, namely the rate of change of photon fluence versus the source-detector distance in comparison to that along a straight-line on a semi-infinite medium-applicator interface, are expected to hold for concave or convex geometry of smaller radius. This section conducts numerical evaluations based on general analytical results given in Eqs. (5.3.1.AC) and (5.3.2.AC), and FEM, to examine the qualitative patterns of FD photon diffusion for concave or convex geometry of smaller radius.

Table 5. Summary of the Analytical Expressions Presented in Section 5.4

	Concave geometry		Semi-infinite geometry	**Convex geometry**	
	Case-longi	***Case-azi***		***Case-longi***	***Case-azi***
$\frac{\partial \ln\left(\overline{\Psi}\cdot d^2\right)}{\partial d}$ **Decay rate of DC amplitude**	$-\left[\bar{k}_0+\frac{1}{2\bar{k}_0 R_b\left(R_0-R_a\right)}\right]$	$-\left\{\bar{k}_0+\frac{1}{2\bar{k}_0 R_b\left(R_0-R_a\right)}-\left[\frac{2R_0-R_a+2R_b}{2R_0R_b\left(R_0-R_a\right)}\right]d\right\}$	$-\bar{k}_0$	$-\left[\bar{k}_0-\frac{1}{2\bar{k}_0 R_b\left(R_0+R_a\right)}\right]$	$-\left\{\bar{k}_0-\frac{1}{2\bar{k}_0 R_b\left(R_0+R_a\right)}+\left[\frac{2R_0+R_a-2R_b}{2R_0R_b\left(R_0+R_a\right)}\right]d\right\}$
$\frac{\partial \ln\left(\lvert\widetilde{\Psi}\rvert\cdot d^2\right)}{\partial d}$ **Decay rate of AC amplitude**	$-\left[\tilde{k}_{amp}+\frac{\tilde{k}_{amp}}{2\left(\tilde{k}_{amp}^2+\tilde{k}_{phi}^2\right)R_b\left(R_0-R_a\right)}\right]$	$-\left\{\tilde{k}_{amp}+\frac{\tilde{k}_{amp}}{2\left(\tilde{k}_{amp}^2+\tilde{k}_{phi}^2\right)R_b\left(R_0-R_a\right)}-\left[\frac{2R_0-R_a+2R_b}{2R_0R_b\left(R_0-R_a\right)}\right]d\right\}$	$-\tilde{k}_{amp}$	$-\left[\tilde{k}_{amp}-\frac{\tilde{k}_{amp}}{2\left(\tilde{k}_{amp}^2+\tilde{k}_{phi}^2\right)R_b\left(R_0+R_a\right)}\right]$	$-\left\{\tilde{k}_{amp}-\frac{\tilde{k}_{amp}}{2\left(\tilde{k}_{amp}^2+\tilde{k}_{phi}^2\right)R_b\left(R_0+R_a\right)}+\left[\frac{2R_0+R_a-2R_b}{2R_0R_b\left(R_0+R_a\right)}\right]d\right\}$
$\frac{\partial\left[\ln(Mod)\right]}{\partial d}$ **Change rate of modulation -depth**	$-\left\{\left(\tilde{k}_{amp}-\bar{k}_0\right)-\frac{1}{2R_b\left(R_0-R_a\right)}\left[\frac{1}{\bar{k}_0}-\frac{\tilde{k}_{amp}}{\tilde{k}_{amp}^2+\tilde{k}_{phi}^2}\right]\right\}$		$-\left(\tilde{k}_{amp}-\bar{k}_0\right)$	$-\left\{\left(\tilde{k}_{amp}-\bar{k}_0\right)+\frac{1}{2R_b\left(R_0+R_a\right)}\left[\frac{1}{\bar{k}_0}-\frac{\tilde{k}_{amp}}{\tilde{k}_{amp}^2+\tilde{k}_{phi}^2}\right]\right\}$	
$\frac{\partial\left\lvert\angle\widetilde{\Psi}\right\rvert}{\partial d}$ **Change rate of phase**	$\tilde{k}_{phi}-\frac{\tilde{k}_{phi}}{2\left(\tilde{k}_{amp}^2+\tilde{k}_{phi}^2\right)R_b\left(R_0-R_a\right)}$		$\tilde{k}_{phi}$	$\tilde{k}_{phi}+\frac{\tilde{k}_{phi}}{2\left(\tilde{k}_{amp}^2+\tilde{k}_{phi}^2\right)R_b\left(R_0+R_a\right)}$	

In sections 5.5.1 to 5.5.3, two specific cases, namely *case-azi* and *case-longi*, in concave or convex geometry are examined. In *case-azi* the source and detector are azimuthally aligned, thus $z = z'$ is applied to both Eq. (5.3.1.AC) and Eq. (5.3.2.AC). In *case-longi* the source and detector are longitudinally aligned, thus $\varphi = \varphi'$ is applied to both Eq. (5.3.1.AC) and Eq. (5.3.2.AC). In either Eq. (5.3.1.AC) or Eq. (5.3.2.AC) the limits of m in the summation and k in the integration are chosen following the criteria adopted in Chapter II for numerical evaluation of

the analytic results for CW photon diffusion. The limits of *m* and *k* are evaluated individually for each set of computations conducted in this study. Each plot of the numerical implementation of the analytical results to FD photon diffusion is also accompanied by FEM simulation using a package of near-infrared fluorescence and spectroscopy tomography (NIRFAST) (Dehghani et al., 2009). For both concave and convex geometries, the FEM meshing volume is a cylinder of 40cm in height and 10cm in radial thickness. Denser meshes are placed along the mid azimuth plane on the medium-applicator interface for *case-azi*, and along the longitudinal direction for *case-longi*. The meshing volume for the semi-infinite geometry is a 16cm×8cm×8cm rectangle, and denser meshes are generated along the straight line whereupon the optodes are placed. In each set of computation for concave, convex and semi-infinite geometries, the meshing volume is discretized into at least 50000 tetrahedral elements with more than 10000 nodes. Unless otherwise specified, the radius of the cylindrical applicator is 10mm, the optical parameters are $\mu_a = 0.0025mm^{-1}$, $\mu_s' = 1mm^{-1}$, $A = 1.86$, and the modulation frequency is 100MHz.

Section 5.5.4 is used to illustrate the set of spiral-paths associated with the amplitude of AC photon fluence rate and the set corresponding to DC photon fluence rate, on both concave and convex medium-applicator interfaces. The profiling of the spiral-paths for the amplitude of AC photon fluence rate is methodologically similar to that for DC photon fluence rate, based on a two-step procedure detailed in Chapter IV. Briefly, a coarse rectangular grid with 0.1mm length is firstly generated in the interested area along the concave or convex medium-applicator interface, by numerically evaluating Eq. (5.3.1.AC) or Eq. (5.3.2.AC) respectively for concave or convex medium-applicator interface. The area of interest is determined by comparing the numerical evaluations of Eq. (5.3.1.AC) or Eq. (5.3.2.AC) with the semi-infinite analytic results of Eq. (5.2.5.AC). In the second step, a denser rectangular grid with 0.04mm length is interpolated within the coarse grid. For the source located on the origin, the field point has three directions to move on the denser grid in each step: along the azimuthal direction, along the

longitudinal direction, and along the diagonal of the previous two directions. For each direction, the difference of the amplitude of AC photon fluence rate originating from the source with respect to that detected along a straight line on a semi-infinite medium-applicator interface is calculated. The direction with the least difference is the direction to move the field point one step, which becomes the starting point for the next step. The trace of the moving field point forms the spiral profile.

5.5.1 The change of AC-amplitude with respect to d

Figure 42 (A) and (B) illustrate the changes of AC-amplitude of photon fluence rate versus the source-detector distance in both concave and convex geometries. A vertical shift is incurred to the FEM results due to the difference of the source term from the one for numerical evaluation of the analytic results. As illustrated in Fig. 42 (A) for concave geometry, the decay rate of AC amplitude is smaller in *case-azi* while greater in *case-longi* than that along a straight line on the semi-infinite interface for the same source-detector distance. Conversely for convex geometry, as illustrated in Fig. 42 (B), the decay rate of AC amplitude is greater in *case-azi* while smaller in *case-longi* than that along a straight line on the semi-infinite interface for the same source-detector distance. These salient features indicate that there exists a unique set of spiral profiles on the medium-applicator interface in both concave and convex geometries, as in the case of CW photon diffusion presented in Chapter II, along which the decay rate of AC amplitude could be modeled by that along a straight line on a semi-infinite medium-applicator interface.

It is observed from both Fig. 42 (A) and (B) that the analytic results and FEM simulations agree well in the diffusion regime, i.e. the source-detector distance is greater than several times of the transport scattering length. However within the sub-diffusion regime, as also observed for DC-amplitude in Chapter III, the two approaches deviate, mainly due to the different implements of the source definition. In the analytic treatments the source is defined as a spatial impulse while

in FEM the source is implemented as a spatially Gaussian shaped source. This difference has minimal effects upon photon fluence rate in the diffusion regime while noticeably affect the photon fluence rate in the sub-diffusion regime. The deviation is also related to the boundary

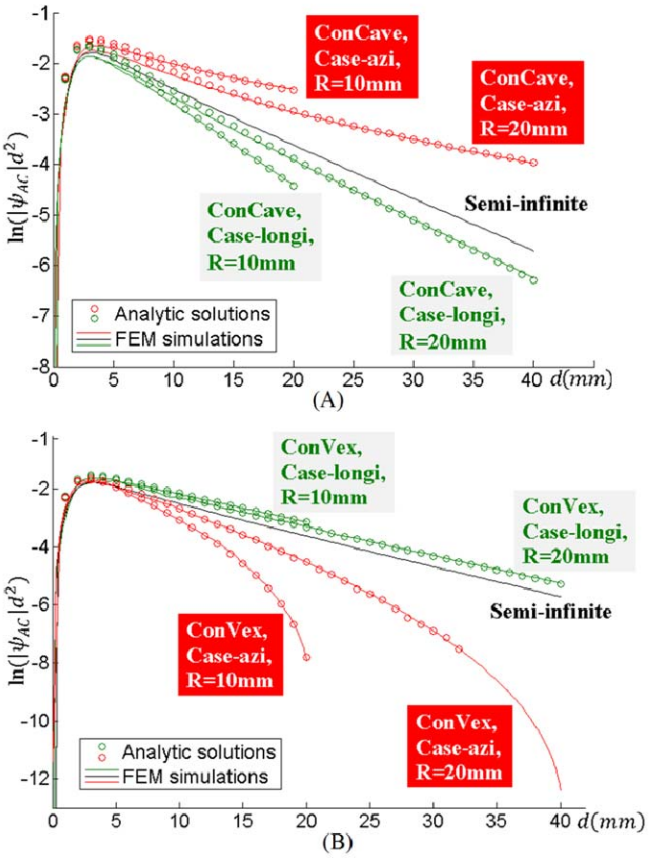

Fig. 42 The changes of AC-amplitude versus source-detector distance in both *case-azi* and *case-longi* configurations. (A) In concave geometry, the decay rate of AC amplitude is smaller in *case-azi* while greater in *case-longi* than that along a straight line on the semi-infinite interface. (B) In convex geometry, the decay rate of AC amplitude is greater in *case-azi* while smaller *in case-longi* than that along a straight line on the semi-infinite interface.

conditions, as in the analytic treatments the extrapolated boundary is assumed while in FEM the Robin-type boundary condition is employed. In Fig. 42 (B), the amplitude of photon fluence rate

in convex geometry in *case-azi* is only plotted for source-detector distance less than 32mm, as for larger source-detector distance the modified Bessel functions in Eq. (5.3.1.AC) and Eq. (5.3.2.AC) is beyond the smallest or the greatest number that can be accommodated by IEEE standard for floating-point arithmetic (IEEE 754-2008 Standard for Floating-Point Arithmetic (IEEE, 2008)).

5.5.2 Changes of modulation-depth versus source-detector distance and modulation frequency

The changes of modulation-depth at 100MHz versus source-detector distance in concave and convex geometries are shown in Fig. 43(A). The changes of modulation-depth at a fixed source-detector distance $d = 15mm$ versus modulation frequency in concave and convex geometries are depicted in Fig. 43(B). Figure 43 indicates that the reduction of modulation-depth is smaller in concave geometry while greater in convex geometry than that along a straight line on the semi-infinite medium-applicator interface for the same modulation frequency. Therefore no spiral-paths occurring to DC or the amplitude of AC fluence rate is inferred for the modulation-depth. The modulation depth evaluated along the longitudinal direction, however, is always closer to that along a straight-line on the semi-infinite interface than the one evaluated along the azimuthal direction is.

5.5.3 Changes of phase versus source-detector distance and modulation frequency

The changes of phase at 100MHz versus source-detector distance in concave and convex geometries are shown in Fig. 44(A). The changes of phase at a fixed source-detector distance $d = 15mm$ versus modulation frequency in concave and convex geometries are depicted in Fig. 44(B). Figure 44 indicates that the phase increases slower in concave geometry while greater in convex geometry than that along a straight line on the semi-infinite medium-applicator interface for the same modulation frequency.

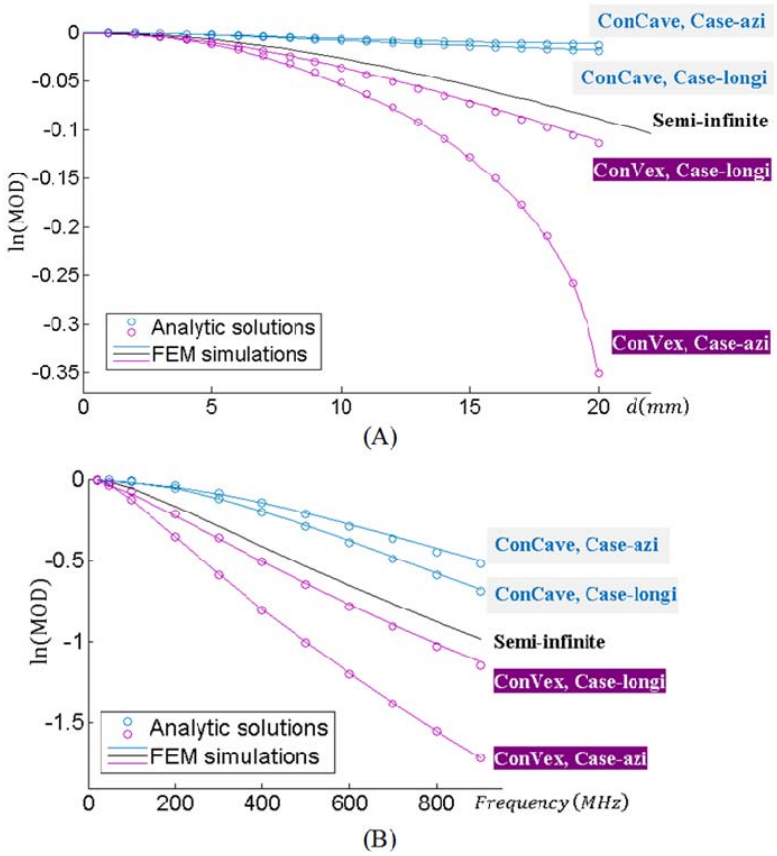

Fig. 43 (A) The changes of modulation-depth versus source-detector distance in the concave geometry and convex geometry at 100MHz modulation frequency. (B). The changes of modulation-depth versus modulation frequency in the concave geometry and convex geometry at a source-detector distance of $d = 15mm$. In both (A) and (B), the reduction of the modulation-depth is smaller in both case-azi and case-longi of concave geometry and greater in both case-azi and case-longi of convex geometry than that along a straight line on the semi-infinite interface, for the same source-detector distance.

Therefore no spiral-paths occurring to DC or the amplitude of AC fluence rate is inferred for the phase change of AC photon fluence rate. The phase evaluated along the longitudinal direction, however, is always closer to that along a straight-line on the semi-infinite interface than the one evaluated along the azimuthal direction is.

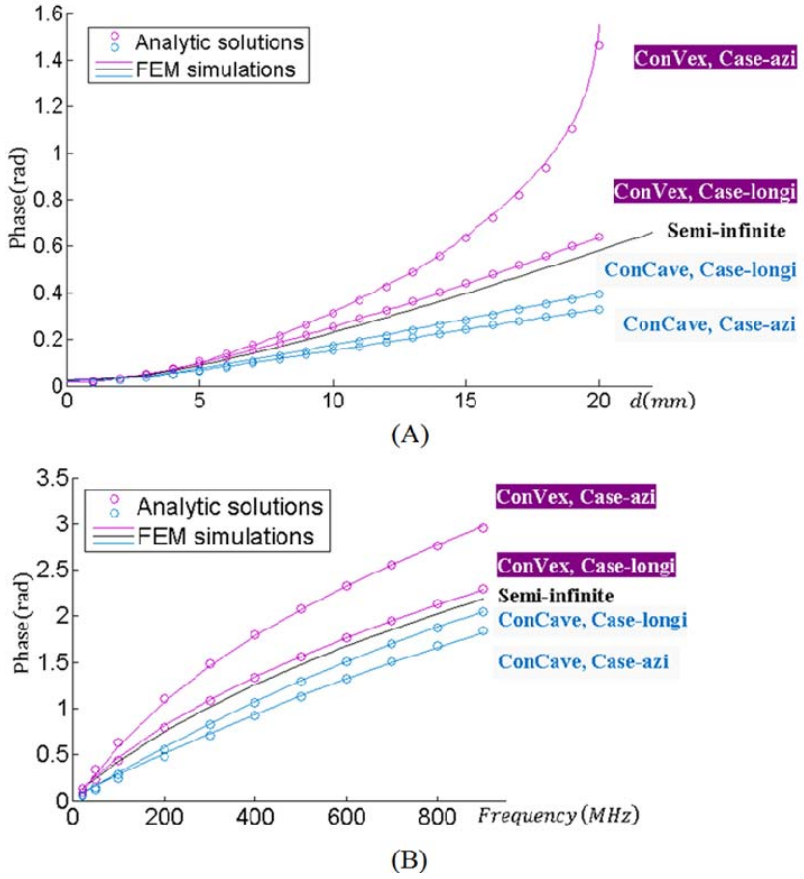

Fig. 44 (A) The changes of phase versus source-detector distance in the concave geometry and convex geometry at 100MHz modulation frequency. (B). The changes of phase versus modulation frequency in the concave geometry and convex geometry at a source-detector distance of $d = 15mm$. In both (A) and (B), the increase of the phase is smaller in both case-azi and case-longi of concave geometry and greater in both case-azi and case-longi of convex geometry than that along a straight line on the semi-infinite interface, for the same source-detector distance.

5.5.4 Spiral-paths for DC and the amplitude of AC photon fluence rates

The different spiral-paths associated with DC and the amplitude of AC photon fluence rates are illustrated in Fig. 45 (A) for concave medium-applicator interface and Fig. 45 (B) for convex medium-applicator interface respectively. The spiral-paths are computed for only a specific set of parameters, including a cylinder radius of 10mm, optical properties of $\mu_a = 0.002mm^{-1}$, $\mu_s' = 0.5mm^{-1}$, $A = 1.86$, and a modulation frequency of 100MHz. It is shown that the spiral-paths for AC-amplitude are tilted more axially than that for DC photon fluence rate. The difference between these two sets of spiral-paths seems to be greater on the convex medium-applicator interface than that on the concave medium-applicator interface.

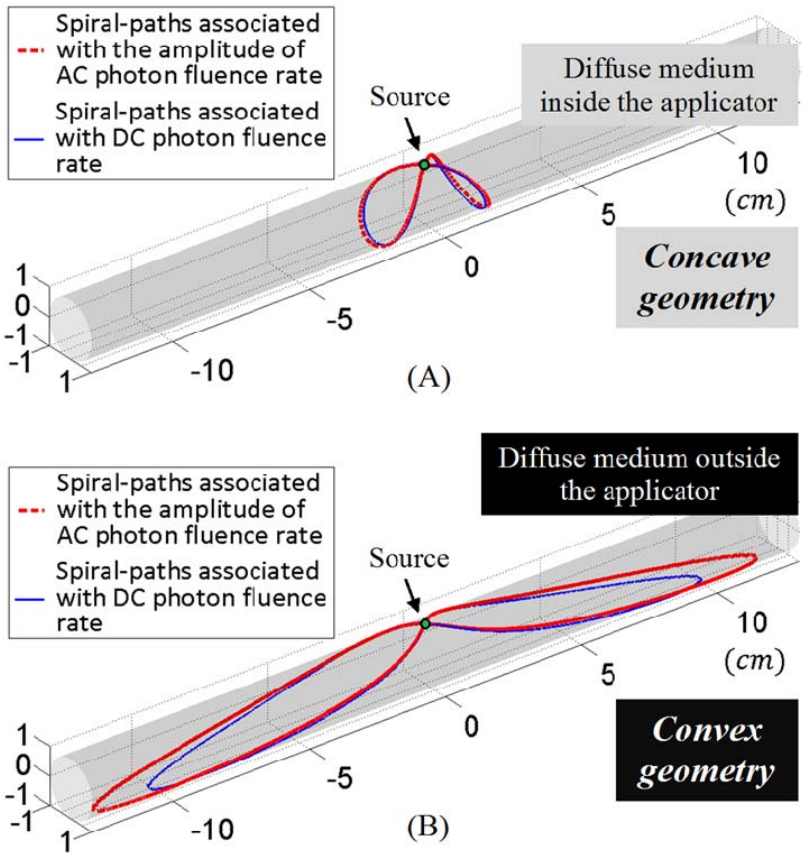

Fig. 45 (A) The spiral-paths associated with the amplitude of AC and DC photon fluence rate on the concave medium-applicator interface. (B) The spiral-paths associated with the amplitude of AC and DC photon fluence rate on the convex medium-applicator interface. In both (A) and (B), the spiral-paths for the amplitude of AC photon fluence rate tilt more axially than that for DC photon fluence rate. The difference between these two sets of spiral-paths is more pronounced on the convex medium-applicator interface.

5.6 Discussions

The existence of a phase offset at $d = 0mm$ is easily observed for all the investigated geometries in Fig. 44(A). This offset can be related directly to the term $\tan^{-1}\left(\widetilde{k}_{phi} \big/ \widetilde{k}_{amp}\right)$ appearing in the phase part of the FD photon fluence, as appearing in Eqs. (5.2.7.AC), (5.4.3.AC), and (5.4.6.AC). The existence of this phase offset can also be interpreted through the diffusion process, as a directional physical source is replaced by an isotropic source placed one transport scattering length inwards to the diffuse medium, and the approximation is valid only for source-detector distance greater than 3-5 times of transport scattering length. It is also observed that regardless of the geometry, the phase of photon fluence appears to be nearly linear to the modulation frequency below 200MHz. As the modulation frequency goes higher beyond 200MHz, the phase becomes smaller compared to the one projected linearly from sub-200MHz ranges. These appearances of the phase are in agreement with the simulation (Arridge et al., 1992) and experimental results of earlier studies (Tromberg et al., 1993; Yaroslavsky et al., 1997) performed on semi-infinite medium-applicator interface.

The simplified analytic results presented in section 5.4 for cylindrical applicators with large radius provide direct analytic representations of the effect of applicator's curvature when compared with semi-infinite geometry. The sets of Eqs. (5.4.7.DC.conC) and (5.4.7.AC.conC) for concave geometry and Eqs. (5.4.7.DC.conV) and (5.4.7.AC.conV) for convex geometry show that as $R_0 \to \infty$, the decay rates of both DC and AC amplitude of photon fluence reach those in semi-infinite geometry. The set of Eqs. (5.4.7.Mod.conC) and (5.4.7.Mod.conV) shows that as $R_0 \to \infty$, the changing rates of the modulation-depth versus the source-detector distance in both concave and convex geometries reach those in semi-infinite geometry. The set of Eqs. (5.4.7.Phi.conC) and (5.4.7.Phi.conV) shows that as $R_0 \to \infty$, the changing rates of the phase of AC photon fluence versus the source-detector distance in both concave and convex geometries

reach those in semi-infinite geometry. Since these qualitative features of FD photon diffusion were derived for cylindrical applicators with very large radius, they do not necessarily represent the exact quantitative features of FD photon diffusion for cylindrical applicator with small, such as at centimeter-order, radius. For instance, for cylindrical applicator with small radius Fig. 43 indicates different rates of modulation-depth change versus the source-detector distance for *case-azi* and *case-longi* in both concave and convex geometries, while the rate-difference between *case-azi* and *case-longi* certainly would diminish as the radius of the cylindrical applicator becomes increasingly large. Similarly Fig. 44 indicates different rates of phase change versus the source-detector distance for *case-azi* and *case-longi* in both concave and convex geometries for cylindrical applicator with small radius, while the rate-difference between *case-azi* and *case-longi* certainly would also diminish as the radius of the cylindrical applicator becomes increasingly large. It is worth to note that numerical evaluation of the general analytical results of Eqs. (5.3.1) or (5.3.2) for FD photon diffusion in concave or convex geometry of large radius is arithmetically challenging.

The numerical evaluations of the analytic results presented in section 5.5 explicitly visualize perhaps some less appreciated aspects of the photon diffusion in both concave and convex geometries. The decay rate of AC amplitude of photon fluence rate and DC photon fluence with respect to source-detector distance could be either greater in *case-azi* and smaller in *case-longi* or smaller in *case-azi* and greater in *case-longi* than that in the semi-infinite geometry. However, the change of modulation-depth and phase with respect to source-detector distance uniquely reflect the applicator curvature when compared with that in the semi-infinite geometry. As indicated in Fig. 43, the changes of modulation-depth with respect to source-detector distance are smaller in concave geometry and larger in convex geometry than that in the semi-infinite geometry, and the changes of phase with respect to source-detector distance show similar opposite trend as indicated in Fig. 44. As the photon fluence reaching the detector is an ensemble of many trajectories, it seems that the ensembled photon-pathlength is shorter in concave

geometry whereas longer in convex geometry than that in semi-infinite geometry for the same source-detector distance. This also agrees with the observation in Fig. 44 regarding the phase changes of AC photon fluence rate versus the source-detector distance in the concave and convex geometries. Subsequently one may expect that, although the measurement in the convex geometry is subjected to smaller signal-to-noise ratio than in concave geometry (the signal-noise-ratio in a quasi-concave geometry analyzed by the more accurate radiative transfer approach is seen in (Kim et al., 2008)) as the modulation-depth drops faster, it may render greater phase sensitivity than the measurement in the concave geometry.

The spiral-paths, which renders the convenience of treating photon fluence rate in either concave or convex geometry as if it is along a straight line on a semi-infinite medium-applicator interface, was proposed and demonstrated for CW photon diffusion. This current study has shown that the spiral-paths do exist to the amplitude of AC photon fluence rate, however they do not coincide with those occurring to DC photon fluence rate. Therefore no single spiral-path can be found for FD photon diffusion that allows treating both the amplitude of AC and DC photon fluence rate as if they are along a straight line on a semi-infinite medium-applicator interface. On the other hand, when both AC amplitude and DC fluence rate are combined, the resulted modulation depth shows smaller changes in concave geometry and greater changes in convex geometry, when comparing with that evaluated along a straight line on a semi-infinite medium-applicator interface. This single-sided response of the modulation depth to the concave or convex curvature of the geometry, which is similar to that of phase, may support the notation that the DC information is indeed supplementary to the AC information for FD measurement (Xu et al., 2010).

5.7 Conclusions

This Chapter studies the frequency domain photon diffusion between a source and a detector on an infinitely long circular cylindrical applicator bounding internally or externally a homogeneous medium. The general analytic results for both concave and convex geometry cases are simplified at large radius to evaluate qualitatively the characteristics of FD photon diffusion, including the AC amplitude, modulation-depth, and phase, with respect to source-detector distance or/and modulation frequency. The discoveries, substantiated by numerical evaluations based on analytical results and FEM at smaller centimeter-order radius, are: 1) the decay rate of the AC amplitude of photon fluence versus the source-detector distance is greater in *case-azi* and smaller in *case-longi* on the concave medium-applicator interface, and conversely smaller in *case-azi* and greater in *case-longi* on the convex medium-applicator interface, than that along a straight-line on the semi-infinite medium-applicator interface; 2) the reduction of modulation-depth versus the source-detector distance is slower on the concave medium-applicator interface and faster on the convex medium-applicator interface than that along a straight-line on the semi-infinite medium-applicator interface; 3) the increase of the phase of AC photon fluence versus the source-detector distance is slower on the concave medium-applicator interface and faster on the convex medium-applicator interface than that along a straight-line on the semi-infinite medium-applicator interface.

CHAPTER VI

FINAL REMARKS

Diffusion process is used to describe many types of particles or energy transfer in scattering media, including photon propagation in biological tissue (Ishimaru et al, 1989), charge-carrier conveyance in semiconducting material (Jost et al., 1933), and neutron navigation in a nuclear reactor (Weinberg et al., 1958). The diffusion-model also applies to observances such as harmonic mass-transport (Cummings et al., 1984), modulated eddy current (Felsen et al., 1973), thermal waves (Mason et al., 1966), and the still-controversial viscosity waves (Hocking et al., 1991), etc. Accurate and accessible quantitation of diffusion is fundamental to probing the properties of associated media and predicting processes (Mandelis et al., 2001).

Modeling optical imaging of biological tissue located centimeters deep involves diffusion approximation to the radiative transport. Although the semi-infinite geometry specific to placing the optodes on a planar medium-applicator interface is most widely studied, other geometries with the optodes on curved medium-applicator interface could be more relevant to imaging applications. A "***concave***" geometry may resemble probing the diffusive medium at the "recessing" side of the cylindrical applicator, and a "***convex***" imaging geometry may represent probing the diffusive medium at the "bulging" side of the cylindrical applicator. For the semi-infinite geometry with a homogeneous medium, the analytic solution to the photon diffusion is well-studied and has been applied widely to analyzing raw data measured from surface tissue applicators and for image reconstruction. For "concave" medium-applicator geometry there are a noticeable amount of studies of diffuse photon propagation within the geometry. Arguably all these approaches were based on the same methodology, i.e., the analytical Green's function is derived in the form of a sum of two terms that contain the analytical solution in the infinite

medium plus a particular solution, specifically the one corresponding to an “image” source, allowing the global solution to satisfy the boundary condition. However, there is lack of understanding regarding FD photon diffusion associated with “convex” medium-applicator geometry.

This thesis developed a theoretical framework to unify the treatments of photon remission on the medium-applicator interface of both “concave” and “convex” geometries with infinite longitudinal dimension, in both continuous-wave (CW) and frequcency domain. Solutions to the photon diffusion in the two geometries were derived based on the extrapolated boundary condition and expressed in terms of the first and second kinds of the modified Bessel functions. Future work may involve studying the fluorescent and time-domain photon diffusion in the trans-luminal geometry.

REFERENCES

1. Arfken G. B. and Weber H. J., Mathematical Methods for Physicists, 6th ed. (Harcourt, 2005).
2. Arridge S. R., Zee P. van der, Cope M. and Delpy D. T., "Reconstruction methods for infra-red absorption imaging," Proc. SPIE 1431, 204-215 (1991).
3. Arridge S. R., Cope M., Delpy D. T., "The theoretical basis for the determination of optical pathlengths in tissue: temporal and frequency analysis," Phys. Med. Biol. **37**, 1531-1560 (1992).
4. Arridge S. R., and Lionheart W. R. B., "Nonuniqueness in diffusion-based optical tomography," Opt. Lett. **23**, 882-884 (1998).
5. Arridge S. R., Schweiger M., Hiraoka M., and Delpy D. T., "A finite element approach for modeling photon transport in tissue," Med. Phys. **20**, 299-309 (1993).
6. Brendel B., and Tim N., "Selection of optimal wavelengths for spectral reconstruction in diffuse optical tomography," J. Biomed. Opt. **14**, 034041 (2009).
7. Boutet J., Herve L., Debourdeau M., Guyon L., Peltie P., Dinten J.-M., Saroul L., Duboeuf F., and Vray D., "Bimodal ultrasound and fluorescence approach for prostate cancer diagnosis," J. Biomed. Opt. **14**, 064001 (2009).
8. Carslaw H. S. and Jaeger J. C., Conduction of Heat in Solids, 2nd ed. (Oxford, 1986).
9. Contini D., Martelli F., and Zaccanti G., "Photon migration through a turbid slab described by a model based on diffusion approximation. I. Theory," Appl. Opt. **36**, 4587–4599 (1997).

10. Corlu A., Choe R., Durduran T., Lee K., Schweiger M., Arridge S. R., Hillman E. M. C., and Yodh A. G., "Diffuse optical tomography with spectral constraints and wavelength optimization," Appl. Opt. **44**, 2082-2093 (2005).
11. Corlu A., Durduran T., Choe R., Schweiger M., Hillman E. M. C., Arridge S. R. and Yodh A. G., "Uniqueness and wavelength optimization in continuous-wave multispectral diffuse optical tomography," Opt. Lett. **28**, 2339-2341 (2003).
12. Correia T., Gibson A., and Hebden J., "Identification of the optimal wavelengths for optical topography: a photon measurement density function analysis," J. Biomed. Opt. **15**, 056002 (2010).
13. Cui S. T., "Electrostatic potential in cylindrical dielectric media using the image charge method," Molecular Phys. **104**, 2993-3001 (2006).
14. Cummings D. L., Reuben R. L., and Blackburn D. A., "The effect of pressure modulation on the flow of gas through a solid membrane: permeation and diffusion of hydrogen through nickel," Metall. Trans. A, **15**, 639-648 (1984).
15. Dehghani H., Eames M. E., Yalavarthy P. K., Davis S. C., Srinivasan S., Carpenter C. M., Pogue B. W., Paulsen K. D., "Near infrared optical tomography using NIRFAST: Algorithm for numerical model and image reconstruction," Commun. Numer. Methods Eng. **25**, 711-732 (2009).
16. Driver I., Feather J. W., King P. R., Dawson J. B., "The optical properties of aqueous suspensions of Intralipid, a fat emulsion," Physics in Medicine and Biology, **34**, 1927–1930 (1989).
17. Fantini S., Franceschini M. A., and Gratton E., "Semi-infinite-geometry boundary problem for light migration in highly scattering media: a frequency-domain study in the diffusion approximation," J. Opt. Soc. Am. B, **11**, 2128–2138 (1994).

18. Farrell T. J., Patterson M. S., Wilson B. C., “A diffusion theory model of spatially resolved, steady-state diffuse reflectance for the noninvasive determination of tissue optical properties,” Med. Phys. **19**, 879–888 (1992).
19. Felsen L. B. and Marcuvitz N., Radiation and Scattering of Waves (Prentice Hall, Englewood Cliffs, N.J., 1973).
20. Fine K. S. and Driscoll C. F., “The finite length diocotron mode,” Phys. Plasmas **5**, 601-607 (1998).
21. Haskell R. C., Svaasand L. O., Tsay T., Feng T., McAdams M. S., and Tromberg B. J., “Boundary conditions for the diffusion equation in radiative transfer,” J. Opt. Soc. Am. A, **11**, 2727–2741 (1994).
22. Hielscher A. H., Bluestone A. Y., Abdoulaev G. S., Klose A. D., Lasker J., Stewart M., Netz U., and Beuthan J., “Near-infrared diffuse optical tomography,” Dis Markers., **18**(5-6), 313-337 (2002).
23. Hocking W.K., Fukao S., Yamamoto M., Tsuda T., and Kato S., “Viscosity waves and thermal-conduction waves as a cause of “specular” reflectors in radar studies of the atmosphere,” Radio Sci. **26**, 1281- 1303 (1991).
24. Huang M., Xie T., Chen N., and Zhu Q., “Simultaneous reconstruction of absorption andscattering maps with ultrasound localization: feasibility study using transmission geometry,” Appl. Opt. **42**, 4102-4114 (2003).
25. IEEE 754-2008 Standard for Floating-Point Arithmetic (IEEE, 2008)
26. Ishimaru A., “Diffusion of light in turbid material,” Appl. Opt. **28**, 2210-2215 (1989).
27. Jackson J. D., “Expansion of Green functions in cylindrical coordinates,” in *Classical Electrodynamics*, 3rd ed. (Wiley, 1998), pp. 125-126.
28. Jacques S. L. and Pogue B. W., “Tutorial on diffuse light transport,” J. Biomed. Opt. **13**, 041302 (2008)

29. Jiang Z., Piao D., Xu G., Ritchey J. W., Holyoak G. R., Bartels K. E., Bunting C. F., Slobodov G., Krasinski J. S., "Trans-rectal ultrasound-coupled near-infrared optical tomography of the prostate Part II: Experimental demonstration," Opt. Express **16**, 17505–17520 (2008).
30. Jiang Z., Holyoak G. R., Bartels K. E., Ritchey J. W., Xu G., Bunting C. F., Slobodov G., Piao D., "In vivo trans-rectal ultrasound coupled near-infrared optical tomography of a transmissible venereal tumor model in the canine pelvic canal," J. Biomed. Opt. Lett. **14**, 030506 (2009).
31. Jiang Z., Piao D., Bartels K. E., Holyoak G. R., Ritchey J. W., Ownby C. L., Rock K., Slobodov G., "Transrectal ultrasound-integrated spectral optical tomography of hypoxic progression of a regressing tumor in a canine prostate," Technology in Cancer Research and Treatment, **10**, 519-531 (2011).
32. Jiang Z., Ph.D. Dissertation, "Study of trans-rectal near-infrared diffuse optical tomography concurrent with trans-rectal ultrasound for prostate imaging", July, 2011.
33. Jost W., "Diffusion and electrolytic conduction in crystals (ionic semiconductors)," J. Chem. Phys. **1**, 466-475 (1933).
34. Kim H. K., Netz U. J., Beuthan J., and Hielscher A. H., "Optimal source-modulation frequencies for transport-theory-based optical tomography of small-tissue volumes," Optics Express, **16,** 18082-18101 (2008).
35. Li C., Liengsawangwong R., Choi H., Cheung R., "Using a priori structural information from magnetic resonance imaging to investigate the feasibility of prostate diffuse optical tomography and spectroscopy: a simulation study," Med. Phys. **34**, 266-74 (2007).
36. Liemert A. and Kienle A., "Light diffusion in a turbid cylinder. I. Homogeneous Case," Opt. Express **18**, 9456-9473 (2010).
37. Liemert A. and Kienle A., "Light diffusion in a turbid cylinder. II. Layered case," Opt. Express **18**, 9266-9279 (2010).

38. Mandelis A., *Diffusion-wave Fields: Mathematical Methods and Green Functions* (Springer-Verlag, 2001).
39. Marquez G., Wang V. L., Lin S., Schwartz J. A., and Thomsen S. L., "Anisotropy in the absorption and scattering spectra of chicken breast tissue," Appl. Opt. **37**, 798-804 (1998).
40. Mason E. A., Munn R. J., and Smith F. J., "Thermal Diffuison in Gases," in *Advances in Atomic and Molecular Physics*, (Academic, 1966), pp. 33-91.
41. Michels R., Foschum F., and Kienle A., "Optical properties of fat emulsions," Opt. Express **16**, 5907-5925 (2008).
42. Miki S., Tanaka S., Shimomura Y., "Determination of Optical Properties of Chicken Breast Tissue Using a Three-Fiber Based Diffuse Reflectance Method," in Biomedical Optics, Technical Digest (CD) (Optical Society of America, 2006), paper TuI9.
43. Moler C., "Floating points: IEEE Standard unifies arithmetic model." Cleve's Corner, The MathWorks, Inc., 1996.
44. Musgrove C., Bunting C. F., Dehghani H., Pogue B. W., and Piao D., "Computational aspects of endoscopic near-infrared optical tomography: initial investigations," Proc. SPIE **6434**, 643409 (2007).
45. Ntziachristos V., "Concurrent diffuse optical tomography, spectroscopy and magnetic resonance imaging of breast cancer," Ph.D. dissertation, (University of Pennsylvania, Philadelphia, 2000).
46. O'Leary M. A., Boas D. A., Chance B. and Yodh A. G., "Experimental images of heterogeneous turbid media by frequency-domain diffusing-photon tomography," Opt. Lett. **20**, 426-428 (1995) .
47. Paulsen K. D. and Jiang, H. "Spatially varying optical property reconstruction using a finite element diffusion equation approximation," Am. Assoc. Phys. Med. **22**, 691-701 (1995).

48. Piao D., Jiang Z., Bartels K. E., Holyoak G. R., Ritchey J. W., Xu G., Bunting C. F., Slobodov G., “In vivo trans-rectal ultrasound-coupled near-infrared optical tomography of intact normal canine prostate,” J. Innov. Opt. Health. Sci. **2**, 215-225 (2009).
49. Piao D., Xie H., Zhang W., Kransinski J. S., Zhang G., Dehghani H., and Pogue B. W., “Endoscopic, rapid near-infrared optical tomography,” Opt. Lett. **31**, 2876-2878 (2006).
50. Pogue B. W., and Patterson M. S., “Frequency-domain optical absorption spectroscopy of finite tissue volumes using diffusion theory,” Phys Med Biol. **39**, 1157-80 (1994).
51. Pogue B. W., Poplack S. P., McBride T. O., Wells W. A., Osterman K. S., Osterberg U. L. and Paulsen K. D., “Quantitative hemoglobin tomography with diffuse near-infrared spectroscopy: Pilot results in the breast,” Radiology **218**, 261–266 (2001).
52. Polishchuk A. Ya., Dolne J., Liu F., and Alfano R. R., “Average and most-probable photon paths in random media, ” Opt. Lett. **22**, 430-432 (1997).
53. Poplack S. P., Paulsen K. D., Hartov A., Meaney P. M., Pogue B. W., Tosteson T. D., Soho S. K., and Wells W. A., “Electromagnetic breast imaging - Pilot results in women with abnormal mammography,” Radiology **243**, 350–359 (2007).
54. Sabo K. and Bjornerud A., “Accurate de-oxygenation of ex vivo whole blood using sodium dithionite,” Proc. Intl. Soc. Mag. Reson. Med. **8** (2000).
55. Sassaroli A., Martelli F., Zaccanti G., and Yamada Y., "Performance of fitting procedures in curved geometry for retrieval of the optical properties of tissue from time-resolved measurements," Appl. Opt. **40**, 185-197 (2001).
56. Silva A. Da, Leabad M., Driol C., Bordy T., Debourdeau M., Dinten J., Peltié P., and Rizo P., “Optical calibration protocol for an x-ray and optical multimodality tomography system dedicated to small-animal examination,” Appl. Opt. **48**, D151-D162 (2009).
57. Srinivasan S., Pogue B. W., Carpenter C., Jiang S., Wells W. A., Poplack S. P., Kaufman P. A., Paulsen K. D., “Developments in quantitative oxygen-saturation imaging of breast tissue

in vivo using multispectral near-infrared tomography." Antioxid Redox Signal. **9**, 1143-56 (2007).

58. Srinivasan S., Pogue B. W., Jiang S., Dehghani H., Paulsen K. D., "Spectrally constrained chromophore and scattering NIR tomography provides quantitative and robust reconstruction," Appl. Opt. **44**, 1858-1869 (2005).
59. Tromberg B. J., Svaasand L. O., Tsay T., and Haskell R. C., "Properties of photon density waves in multiple-scattering media," Appl. Opt. **32**, 607-616 (1993).
60. Wang L. V. and Wu H., Biomedical Optics, Principles and Imaging, (John Wiley & Sons, Inc., 2007).
61. Weinberg A. M. and Wigner E. P., *The Physical Theory of Neutron Chain Reactors* (University of Chicago Press, 1958).
62. Xu G., Piao D., Bunting C. F., and Dehghani H., "Direct-current-based image reconstruction versus direct-current included or excluded frequency-domain reconstruction in diffuse optical tomography," Appl. Opt. **49**, 3059-3070 (2010).
63. Yao G. and Haidekker M. A., "Transillumination optical tomography of tissue engineered blood vessels: a Monte-Carlo simulation," Appl. Opt. **44**, 4265-4271(2005).
64. Yaroslavsky I. V., Yaroslavsky A. N., Tuchin V. V., and Schwarzmaier H. J., "Effect of the scattering delay on time-dependent photon migration in turbid media," Appl Opt. **36**, 6529-6538 (1997).
65. Zhang A, Piao D, Bunting CF, Pogue BW, "Photon diffusion in a homogeneous medium bounded externally or internally by an infinitely long circular cylindrical applicator. I. Steady-state theory," Journal of Optical Society of America, A, **27**, pp. 648-662 (2010).
66. Zhang A, Xu G, Yao G, Krasinski JS, Bunting CF, Pogue BW, Piao D, "Photon diffusion in a homogeneous medium bounded externally or internally by an infinitely long circular cylindrical applicator. II. Quantitative examinations of the steady-state theory," Journal of Optical Society of America, A, **28**, pp. 66-75 (2011).

67. Zhang A, Piao D, Yao G, Bunting CF, Jiang Y, "Diffuse photon remission along unique spiral paths on a cylindrical interface is modeled by photon remission along a straight line on a semi-infinite interface," Optics Letters, **36**, pp. 654-656 (2011).
68. Zhang A, Piao D, Bunting CF, "Photon diffusion in a homogeneous medium bounded externally or internally by an infinitely long circular cylindrical applicator. III. Synthetic study of continuous-wave photon fluence rate along unique spiral paths," Journal of Optical Society of America, A, **29**, pp.545-558 (2012).
69. Zhang A, Piao D, "Photon diffusion in a homogenous medium bounded externally or internally by an infinitely long circular cylindrical applicator. IV. Frequency-domain Analysis," Journal of Optical Society of America, A, **29**, pp.1445-1458 (2012).
70. Zhou X. and Zhu T. C., "Interstitial diffuse optical tomography using an adjoint model with linear sources," Proc. SPIE **6845**, 68450C (2008).

APPENDICES

Appendix A ----- The solution to Eq. (2.1.10) following Jackson's approach in (Jackson, 1998).

The Eq. (2.1.10) is re-written here

$$\frac{1}{\rho}\frac{\partial}{\partial\rho}\left(\rho\frac{\partial g_m(k,\rho,\rho')}{\partial\rho}\right)-\left(k_{eff}^2+\frac{m^2}{\rho^2}\right)g_m(k,\rho,\rho')=-\frac{1}{\rho}\delta(\rho-\rho') \quad \text{(A.1)}$$

For $\rho\neq\rho'$, Eq. (A.1) is the equation for the modified Bessel functions, $I_m(k_{eff}\rho)$ and $K_m(k_{eff}\rho)$. According to Jackson (Jackson, 1998), suppose that $\psi_1(k_{eff}\rho)$ is some linear combination of I_m and K_m satisfying the boundary conditions for $\rho<\rho'$, and $\psi_2(k_{eff}\rho)$ is a linearly independent combination of I_m and K_m satisfying the boundary conditions for $\rho>\rho'$, then the symmetry of the Green's function in ρ and ρ' requires that

$$g_m(k,\rho,\rho')=\psi_1(k_{eff}\rho_<)\psi_2(k_{eff}\rho_>) \quad \text{(A.2)}$$

where $\rho_<$ and $\rho_>$ indicate the smaller and larger radial coordinates of the source and the detector.

The normalization of the product $\psi_1(k_{eff}\rho_<)\cdot\psi_2(k_{eff}\rho_>)$ requires that $g_m(k,\rho,\rho')$ satisfies the discontinuity in slope implied by the Delta function in Eq. (A.1):

$$\left.\frac{dg_m}{d\rho}\right|_{+} - \left.\frac{dg_m}{d\rho}\right|_{-} = -\frac{1}{\rho'} \tag{A.3}$$

where $|_{\pm}$ means evaluated at $\rho = \rho' \pm \varepsilon$. Then we have

$$\left.\frac{dg_m}{d\rho}\right|_{+} - \left.\frac{dg_m}{d\rho}\right|_{-} = k_{eff}\left(\psi_1\psi_2' - \psi_2\psi_1'\right) = k_{eff}W\left[\psi_1, \psi_2\right] \tag{A.4}$$

where $W\left[\psi_1, \psi_2\right]$ is the Wronskian of ψ_1 and ψ_2. Equation (A.1) is of the Sturm-Liouville type

$$\frac{d}{dx}\left[p(x)\frac{dy}{dx}\right] + g(x)y = 0 \tag{A.5}$$

and it is known that the Wronskian of two linearly independent solutions of such an equation is proportional to $\left[1/p(x)\right]$. Hence the possibility of $g_m(k, \rho, \rho')$ satisfying Eq. (A.3) for all values of ρ' is assured, so it requires that the Wronskian has the value

$$W\left[\psi_1(x), \psi_2(x)\right] = -\frac{1}{x} \tag{A.6}$$

which normalizes $\psi_1\left(k_{eff}\rho_<\right)\cdot\psi_2\left(k_{eff}\rho_>\right)$. If there is no boundary surface, $g_m(k, \rho, \rho')$ must be finite at $\rho = 0$ and vanishes at $\rho \to \infty$. Consequently we can define

$$\psi_1\left(k_{eff}\rho_<\right) = \Omega\, I_m\left(k_{eff}\rho_<\right) \quad \text{and} \quad \psi_2\left(k_{eff}\rho_>\right) = K_m\left(k_{eff}\rho_>\right) \tag{A.7}$$

where the constant Ω is to be determined from the normalization requirement of Eq. (A.6). Substituting Eq. (A.7) into Eq. (A.6) by changing the argument $k_{eff}\rho \to x$ we have

$$\Omega \cdot W\left[I_m(x), K_m(x)\right] = -\frac{1}{x} \tag{A.8}$$

which can be evaluated at any value of x. Based on the asymptotic expressions for the modified Bessel functions (Arfken et al., 2005), we have for either small x or large x

$$W\left[I_m(x), K_m(x)\right] = -\frac{1}{x} \tag{A.9}$$

that leads to $\Omega = 1$ in Eq. (A.8), thereby Eq. (A.2) changes to

$$g_m(k,\rho,\rho') = I_m(k_{eff}\rho_<)K_m(k_{eff}\rho_>) \tag{A.10}$$

Substituting Eq. (A.10) into Eq. (2.1.7) gives the Green's function of Eq. (2.1.3) in cylindrical coordinates as

$$G(\vec{r},\vec{r}') = \frac{1}{2\pi^2}\sum_{m=-\infty}^{\infty}\int_0^{\infty} dk\, e^{im(\varphi-\varphi')}\left[I_m(k_{eff}\rho_<)K_m(k_{eff}\rho_>)\right]\cdot\cos\left[k(z-z')\right] \tag{A.11}$$

Writing in terms of the real function:

$$G(\vec{r},\vec{r}') = \frac{1}{2\pi^2}\int_0^{\infty} dk\cdot\left\{\sum_{m=0}^{\infty}\varepsilon_m\, I_m(k_{eff}\rho_<)K_m(k_{eff}\rho_>)\cos\left[m(\varphi-\varphi')\right]\right\}\cdot\cos\left[k(z-z')\right] \tag{A.12}$$

where
$$\varepsilon_m = \begin{cases} 2, & m \neq 0 \\ 1, & m = 0 \end{cases} \tag{A.13}$$

Appendix B: Derivation of Eq. (4.2.7) from Eq. (4.2.6)

Equation (4.2.6) is rewritten here as:

$$\Psi = \frac{S}{4\pi D}\frac{e^{-k_0 d}}{d}\left\{\left[1-\frac{1}{2}k_0 d\left(\frac{R_a^2}{d^2}-\frac{R_a}{R_0}(\cos\alpha)^2\right)\right]\right.$$

$$\left.-\left[1-\frac{1}{2}k_0 d\left(\frac{(R_a+2R_b)^2}{d^2}+\frac{R_a+2R_b}{R_0}(\cos\alpha)^2\right)\right]\left(1+\frac{R_a+R_b}{R_0-R_a}\right)\right\} \quad \text{(B.1)}$$

Equation (B.1) can be further simplified as

$$\Psi = \frac{S}{4\pi D}\frac{e^{-k_0 d}}{d}\left[1-\frac{k_0 R_a^2}{2d}+\frac{k_0 R_a d}{2R_0}(\cos\alpha)^2-1+\frac{k_0(R_a+2R_b)^2}{2d}+\frac{k_0(R_a+2R_b)d}{2R_0}(\cos\alpha)^2\right.$$

$$\left.-\frac{R_a+R_b}{R_0-R_a}+\frac{k_0(R_a+2R_b)^2}{2d}\frac{R_a+R_b}{R_0-R_a}+\frac{k_0(R_a+2R_b)d}{2R_0}\frac{R_a+R_b}{R_0-R_a}(\cos\alpha)^2\right]$$

$$=\frac{S}{4\pi D}\frac{e^{-k_0 d}}{d}\left[\frac{2k_0 R_b(R_a+R_b)}{d}+\frac{k_0(R_a+R_b)d}{R_0}(\cos\alpha)^2-\frac{R_a+R_b}{R_0-R_a}\right.$$

$$\left.+\frac{k_0(R_a+2R_b)^2}{2d}\frac{R_a+R_b}{R_0-R_a}+\frac{k_0(R_a+2R_b)d}{2R_0}\frac{R_a+R_b}{R_0-R_a}(\cos\alpha)^2\right]$$

$$=\frac{S}{2\pi D}\frac{e^{-k_0 d}}{d}\frac{k_0 R_b(R_a+R_b)}{d}\left[1-\frac{d}{2k_0 R_b(R_0-R_a)}+\frac{d^2}{2R_b R_0}(\cos\alpha)^2\right.$$

$$\left.+\frac{(R_a+2R_b)d^2}{4R_b R_0(R_0-R_a)}(\cos\alpha)^2+\frac{(R_a+2R_b)^2}{4R_b(R_0-R_a)}\right] \quad \text{(B.2)}$$

Under the assumption that $R_0 >> R_a, R_b, d$, based on Taylor expansion, Equation (B.2) can be approximated as

$$\Psi = \frac{S}{2\pi D}\frac{e^{-k_0 d}}{d}\frac{k_0 R_b(R_a+R_b)}{d}\exp\left\{-\frac{d}{2k_0 R_b(R_0-R_a)}\right.$$

$$+\left[\frac{d^2}{2R_bR_0}+\frac{(R_a+2R_b)d^2}{4R_bR_0(R_0-R_a)}\right](\cos\alpha)^2+\frac{(R_a+2R_b)^2}{4R_b(R_0-R_a)}\Bigg\} \tag{B.3}$$

By multiplying both sides of Eq. (B.3) with d^2 we have

$$\Psi d^2=\frac{S}{2\pi D}k_0R_b(R_a+R_b)e^{\frac{(R_a+2R_b)^2}{4R_b(R_0-R_a)}}\exp\Bigg\{-k_0d-\frac{d}{2k_0R_b(R_0-R_a)}$$

$$+\left[\frac{1}{2R_bR_0}+\frac{R_a+2R_b}{4R_bR_0(R_0-R_a)}\right](\cos\alpha)^2d^2\Bigg\} \tag{B.4}$$

Taking the natural logarithm, Eq. (B.4) leads to

$$\ln(\Psi d^2)=-k_0d-\frac{d}{2k_0R_b(R_0-R_a)}+\left[\frac{1}{2R_bR_0}+\frac{R_a+2R_b}{4R_bR_0(R_0-R_a)}\right](\cos\alpha)^2d^2$$

$$+\ln\left[\frac{S}{2\pi D}k_0R_b(R_a+R_b)\right]+\frac{(R_a+2R_b)^2}{4R_b(R_0-R_a)} \tag{B.5}$$

Taking the derivative with respect to d and substituting $d_\perp=d\cdot\cos\alpha$, Eq. (B.5) leads to

$$\frac{\partial\ln(\Psi\cdot d^2)}{\partial d}=-\left\{k_0+\frac{1}{2k_0R_b(R_0-R_a)}-\left[\frac{2R_0-R_a+2R_b}{2R_0R_b(R_0-R_a)}\right]\cos\alpha\cdot d_\perp\right\} \tag{B.6}$$

Appendix C: Derivation of Eq. (4.2.16) from Eq. (4.2.15)

Equation (4.2.15) is rewritten here as:

$$\Psi = \frac{S}{4\pi D}\frac{e^{-k_0 d}}{d}\left\{\left[1-\frac{1}{2}k_0 d\left(\frac{R_a^2}{d^2}+\frac{R_a}{R_0}(\cos\alpha)^2\right)\right]\right.$$

$$\left.-\left[1-\frac{1}{2}k_0 d\left(\frac{(R_a+2R_b)^2}{d^2}-\frac{R_a+2R_b}{R_0}(\cos\alpha)^2\right)\right]\left(1-\frac{R_a+R_b}{R_0+R_a}\right)\right\} \quad \text{(C.1)}$$

Equation (C.1) can be further simplified as

$$\Psi = \frac{S}{4\pi D}\frac{e^{-k_0 d}}{d}\left[1-\frac{k_0 R_a^2}{2d}-\frac{k_0 R_a d}{2R_0}(\cos\alpha)^2-1+\frac{k_0(R_a+2R_b)^2}{2d}-\frac{k_0(R_a+2R_b)d}{2R_0}(\cos\alpha)^2\right.$$

$$\left.+\frac{R_a+R_b}{R_0+R_a}-\frac{k_0(R_a+2R_b)^2}{2d}\frac{R_a+R_b}{R_0+R_a}+\frac{k_0(R_a+2R_b)d}{2R_0}\frac{R_a+R_b}{R_0+R_a}(\cos\alpha)^2\right]$$

$$= \frac{S}{4\pi D}\frac{e^{-k_0 d}}{d}\left[\frac{2k_0 R_b(R_a+R_b)}{d}-\frac{k_0(R_a+R_b)d}{R_0}(\cos\alpha)^2\right.$$

$$\left.+\frac{R_a+R_b}{R_0+R_a}-\frac{k_0(R_a+2R_b)^2}{2d}\frac{R_a+R_b}{R_0+R_a}+\frac{k_0(R_a+2R_b)d}{2R_0}\frac{R_a+R_b}{R_0+R_a}(\cos\alpha)^2\right]$$

$$= \frac{S}{4\pi D}\frac{e^{-k_0 d}}{d}\frac{2k_0 R_b(R_a+R_b)}{d}\left[1+\frac{d}{2k_0 R_b(R_0+R_a)}-\frac{d^2}{2R_b R_0}(\cos\alpha)^2\right.$$

$$\left.+\frac{(R_a+2R_b)d^2}{4R_b R_0(R_0+R_a)}(\cos\alpha)^2-\frac{(R_a+2R_b)^2}{4R_b(R_0+R_a)}\right] \quad \text{(C.2)}$$

Under the assumption that $R_0 >> R_a, R_b, d$, based on Taylor expansion, Equation (C.2) can be approximated as

$$\Psi = \frac{S}{4\pi D}\frac{e^{-k_0 d}}{d}\frac{2k_0 R_b(R_a+R_b)}{d}\exp\left\{\frac{d}{2k_0 R_b(R_0+R_a)}\right.$$

$$+\left[-\frac{d^2}{2R_bR_0}+\frac{(R_a+2R_b)d^2}{4R_bR_0(R_0+R_a)}\right](\cos\alpha)^2-\frac{(R_a+2R_b)^2}{4R_b(R_0+R_a)}\Bigg\} \quad \text{(C.3)}$$

By multiplying both sides of Eq. (C.3) with d^2 we have

$$\Psi d^2=\frac{S}{2\pi D}k_0R_b(R_a+R_b)e^{-\frac{(R_a+2R_b)^2}{4R_b(R_0+R_a)}}\exp\Bigg\{-k_0d+\frac{d}{2k_0R_b(R_0+R_a)}$$

$$+\left[-\frac{d^2}{2R_bR_0}+\frac{(R_a+2R_b)d^2}{4R_bR_0(R_0+R_a)}\right](\cos\alpha)^2\Bigg\} \quad \text{(C.4)}$$

Taking the natural logarithm, Eq. (C.4) leads to

$$\ln(\Psi d^2)=-k_0d+\frac{d}{2k_0R_b(R_0+R_a)}+\left[-\frac{1}{2R_bR_0}+\frac{R_a+2R_b}{4R_bR_0(R_0+R_a)}\right](\cos\alpha)^2d^2$$

$$+\ln\left[\frac{S}{2\pi D}k_0R_b(R_a+R_b)\right]-\frac{(R_a+2R_b)^2}{4R_b(R_0+R_a)} \quad \text{(C.5)}$$

Taking the derivative with respect to d at and substituting $d_\perp=d\cdot\cos\alpha$, Eq. (C.5) leads to

$$\frac{\partial\ln(\Psi\cdot d^2)}{\partial d}=-\left\{k_0-\frac{1}{2k_0R_b(R_0+R_a)}+\left[\frac{2R_0+R_a-2R_b}{2R_0R_b(R_0+R_a)}\right]\cos\alpha\cdot d_\perp\right\} \quad \text{(C.6)}$$

Appendix D: The derivation of Eq. (4.5.15) by following the approach in (Arridge et al., 1991)

Equation (4.5.14) is rewritten here:

$$\Psi_{SC}(\vec{r}_d,\vec{r}_s) = -\frac{1}{D_0}\iiint_V G(\vec{r}_d,\vec{r}\,')\,\delta\mu_a(\vec{r}\,')\,\Psi_0(\vec{r}\,',\vec{r}_s)\,d^3r'$$

$$+\frac{1}{D_0}\iiint_V G(\vec{r}_d,\vec{r}\,')\nabla\cdot\{\delta D(\vec{r}\,')\nabla\Psi_0(\vec{r}\,',\vec{r}_s)\}\,d^3r' \qquad \text{(D.1)}$$

The second integration part can be expanded as

$$\iiint_V G(\vec{r},\vec{r}\,')\nabla\cdot\{\delta D(\vec{r})\nabla\Psi_0(\vec{r},\vec{r}_s)\}\,d^3r' =$$

$$\iiint_V G(\vec{r},\vec{r}\,')\nabla\delta D(\vec{r})\cdot\nabla\Psi_0(\vec{r},\vec{r}_s)\,d^3r' + \iiint_V G(\vec{r},\vec{r}\,')\,\delta D(\vec{r})\nabla^2\Psi_0(\vec{r},\vec{r}_s)\,d^3r' \quad \text{(D.2)}$$

Applying Green's first identity $\iiint_v(\phi\,\nabla^2\psi + \nabla\phi\cdot\nabla\psi)d^3x = \oiint_S(\phi\,\hat{n}\cdot\nabla\psi)d^2a$, it can be seen that

$$\iiint_V G(\vec{r},\vec{r}\,')\,\delta D(\vec{r})\nabla^2\Psi_0(\vec{r},\vec{r}_s)\,d^3r'$$

$$= \oiint_S\left(G(\vec{r},\vec{r}\,')\,\delta D(\vec{r})\,\hat{n}\cdot\nabla\Psi_0(\vec{r},\vec{r}_s)\right)d^2a - \iiint_V\nabla\left[G(\vec{r},\vec{r}\,')\,\delta D(\vec{r})\right]\cdot\nabla\Psi_0(\vec{r},\vec{r}_s)\,d^3r' \quad \text{(D.3)}$$

The surface integral in the above derivation eliminates since we have the freedom to choose the surface as infinity, where $G(\vec{r},\vec{r}\,')$ decays to zero. Hence,

$$\iiint_V G(\vec{r},\vec{r}\,')\,\delta D(\vec{r})\nabla^2\Psi_0(\vec{r},\vec{r}_s)\,d^3r' = -\iiint_V\nabla\left[G(\vec{r},\vec{r}\,')\,\delta D(\vec{r})\right]\cdot\nabla\Psi_0(\vec{r},\vec{r}_s)\,d^3r'$$

$$= -\iiint_V G(\vec{r},\vec{r}\,')\nabla\delta D(\vec{r})\cdot\nabla\Psi_0(\vec{r},\vec{r}_s)\,d^3r' - \iiint_V\delta D(\vec{r})\nabla G(\vec{r},\vec{r}\,')\cdot\nabla\Psi_0(\vec{r},\vec{r}_s)\,d^3r' \quad \text{(D.4)}$$

Substituting Eq. (D.4) into Eq. (D.2) leads to

$$\frac{1}{D_0}\iiint_V G(\vec{r},\vec{r}\,')\nabla\cdot\{\delta D(\vec{r})\nabla\Psi_0(\vec{r},\vec{r}_s)\}\,d^3r' = -\frac{1}{D_0}\iiint_V\delta D(\vec{r})\nabla G(\vec{r},\vec{r}\,')\cdot\nabla\Psi_0(\vec{r},\vec{r}_s)\,d^3r' \quad \text{(D.5)}$$

Substituting Eq. (D.5) into Eq. (D.1) leads to

$$\Psi_{SC}(\vec{r}_d,\vec{r}_s) = -\frac{1}{D_0}\iiint_V G(\vec{r}_d,\vec{r}\,')\,\delta\mu_a(\vec{r}\,')\,\Psi_0(\vec{r}\,',\vec{r}_s)\,d^3r'$$

$$-\frac{1}{D_0}\iiint_V \delta D(\vec{r}\,')\,\nabla G(\vec{r}_d,\vec{r}\,')\cdot\nabla\Psi_0(\vec{r}\,',\vec{r}_s)\,d^3r' \qquad \text{(D.6)}$$

Appendix E: Matlab program for calculating Eqs. (2.2.5) and (2.2.17)

Main excute function

```
clear; home;
%unit: cm

Ro = 1.27;  %1.27  2.41046  5.0711
                %0.953135  2.53492

dtemp = 0.1:.4:2.54;
%d = 0;
%Chebyshev nodes for Chebyshev interpolation for semi-empirical
expression
%a = 0.1;  % interval: [a,b]
%b = 2*Ro;
%dc = -cos(pi*[0:300]/300);s
%dtemp = (a+b)*0.5+(b-a)*dc*0.5;


%ztemp = 0:.1:4;
z = 0;

ustemp = 5;
%us = 2:4:40;
ua = .025;
%S = 1.253430283080477e+005;
S = 1;
A = 1.86;

cal =  400;      %500     %150
cutoff = 200;     %70     %200

%n = length(ztemp);
n = length(dtemp);
h = length(ustemp);
y = zeros(h,n);
ylin = zeros(h,n);
ylg = zeros(h,n);
pot = zeros(1,n);

temp = 0;temp2 = 0;
cont = 1;
for us = ustemp
    D = 1/3/(ustemp+ua);
    i = 1;
    for d = dtemp
    %for z = ztemp
        d
```

```
        %pot(i) =
S/pi^2/D*triplequad(@(k,phiprime,zprime)optconvex4(k,phiprime,zprime,z,
d,us,Ro,ua,D,A,cal),0,cutoff,-pi,pi,-5,5);
        pot(i) =
S/pi^2/D*quadgk(@(k)optconvex3(k,z,d,us,Ro,ua,D,A,cal),0,cutoff);
        %pot(i) =
S/pi^2/D*dblquad(@(phiprime,k)optconvex5(phiprime,k,z,d,us,Ro,ua,D,A,ca
l),-pi,pi,0,cutoff);
        i = i+1;
    end
    ylin(cont,:)=pot;
    ylg(cont,:)=log(pot);
    %y(cont,:)=log(ztemp.^2.*pot);
    y(cont,:)=log(dtemp.^2.*pot);

    %[b,q] = polyfit(dtemp,y(cont,:),1);
    %sl(cont) = b(1);
    %intc(cont) = b(2);
    cont = cont+1;
end
%plot(us,sl,'.')

%k = -sqrt(ua./(1/3./(ua+us)));
%axis([-pi/4 pi/4 0 .5]); %axis([xmin xmax ymin ymax]);
%grid minor
```

***Subfunction* "optconvex3"**

```
function pot = optconvex3(k,z,d,us,Ro,ua,D,A,cal)

k1 = sqrt(k.^2+ua/D);

magn = length(k1);

for i = 1:magn
    %function IK = bess(m_max,xi,xk)
    IK2(i,:) = bess(cal,k1(i)*Ro,k1(i)*(Ro+1/us));
    IK1(i,:) = bess(cal,k1(i)*Ro,k1(i)*(Ro-2*A*D));
    I1K(i,:) = bess(cal,k1(i)*(Ro-2*A*D),k1(i)*Ro);
%     d_source = 0.05;
%     d_detector = 0;
%     %For azimuthal & longitudinal
%     IK2(i,:) =
bess(cal,k1(i)*(Ro+d_detector),k1(i)*(Ro+1/us+d_source));
%     IK1(i,:) = bess(cal,k1(i)*(Ro+d_detector),k1(i)*(Ro-2*A*D));
%     I1K(i,:) = bess(cal,k1(i)*(Ro-2*A*D),k1(i)*(Ro+d_detector));

end
IK1 = IK1';
IK2 = IK2';
I1K = I1K';
```

```
y(1,:) = 1/2*IK2(1,:).*(1-I1K(1,:)./IK1(1,:));
m_term(1,:) = y(1,:);
for m = 1:cal
    m_term(m+1,:) = cos(2*m*asin(d/2/Ro)).*IK2(m+1,:).*(1-
I1K(m+1,:)./IK1(m+1,:));
    y(m+1,:) = y(m,:) + m_term(m+1,:);
end

y = y';
for n = 1:magn

    tempValue = y(n,find(diff(sign(diff(y(n,:))))==-2)+1);
    tempIndex =     find(diff(sign(diff(y(n,:))))==-2)+1;
    lenMax = length(tempValue);
    for count = 1:lenMax
        MaxValue(n,count) = tempValue(lenMax-count+1);
        MaxIndex(n,count) = tempIndex(lenMax-count+1);
    end

    tempValue = y(n,find(diff(sign(diff(y(n,:))))==+2)+1);
    tempIndex =     find(diff(sign(diff(y(n,:))))==+2)+1;
    lenMin = length(tempValue);
    for count = 1:lenMin
        MinValue(n,count) = tempValue(lenMin-count+1);
        MinIndex(n,count) = tempIndex(lenMin-count+1);
    end

    if lenMax>8&&lenMin>8
         if MaxIndex(n,1)> MinIndex(n,1)
             finalValue(n,1) =
repaverge7(MaxValue(n,1),MinValue(n,1),MaxValue(n,2),MinValue(n,2),MaxV
alue(n,3),MinValue(n,3),MaxValue(n,4));
         else
             finalValue(n,1) =
repaverge7(MinValue(n,1),MaxValue(n,1),MinValue(n,2),MaxValue(n,2),MinV
alue(n,3),MaxValue(n,3),MinValue(n,4));
         end
    elseif lenMax>4&&lenMin>4
         if MaxIndex(n,1)> MinIndex(n,1)
            finalValue(n,1) =
repaverge5(MaxValue(n,1),MinValue(n,1),MaxValue(n,2),MinValue(n,2),MaxV
alue(n,3));
         else
            finalValue(n,1) =
repaverge5(MinValue(n,1),MaxValue(n,1),MinValue(n,2),MaxValue(n,2),MinV
alue(n,3));
         end
    elseif lenMax>2&&lenMin>2
         if MaxIndex(n,1)> MinIndex(n,1)
            finalValue(n,1) =
repaverge3(MaxValue(n,1),MinValue(n,1),MaxValue(n,2));
         else
            finalValue(n,1) =
repaverge3(MinValue(n,1),MaxValue(n,1),MinValue(n,2));
```

```
        end
    else
        finalValue(n,1) = y(n,cal+1);
    end

    n = n+1;
end

finalValue = finalValue';
pot = cos(k.*z).*finalValue;
```

***Subfunction* "optconcave3"**

```
function pot = optconcave3(k,z,d,us,Ro,ua,D,A,cal)

k1 = sqrt(k.^2+ua/D);

magn = length(k1);

for i = 1:magn
    %function IK = bess(m_max,xi,xk)
    I3K1(i,:) = bess(cal,k1(i)*(Ro-1/us),k1(i)*Ro);
    I1K2(i,:) = bess(cal,k1(i)*Ro,k1(i)*(Ro+2*A*D));
    I2K1(i,:) = bess(cal,k1(i)*(Ro+2*A*D),k1(i)*Ro);
%     d_source = 0.05;
%     d_detector = 0;
%     %For azimuthal & longitudinal
%     I3K1(i,:) = bess(cal,k1(i)*(Ro-1/us-d_source),k1(i)*(Ro-
d_detector));
%     I1K2(i,:) = bess(cal,k1(i)*(Ro-d_detector),k1(i)*(Ro+2*A*D));
%     I2K1(i,:) = bess(cal,k1(i)*(Ro+2*A*D),k1(i)*(Ro-d_detector));


end
I3K1 = I3K1';
I1K2 = I1K2';
I2K1 = I2K1';


y(1,:) = 1/2*I3K1(1,:).*(1-I1K2(1,:)./I2K1(1,:));
m_term(1,:) = y(1,:);
for m = 1:cal
    m_term(m+1,:) = cos(2*m*asin(d/2/Ro)).*I3K1(m+1,:).*(1-
I1K2(m+1,:)./I2K1(m+1,:));
    y(m+1,:) = y(m,:) + m_term(m+1,:);
end

y = y';
for n = 1:magn
```

```
    tempValue = y(n,find(diff(sign(diff(y(n,:))))==-2)+1);
    tempIndex =     find(diff(sign(diff(y(n,:))))==-2)+1;
    lenMax = length(tempValue);
    for count = 1:lenMax
        MaxValue(n,count) = tempValue(lenMax-count+1);
        MaxIndex(n,count) = tempIndex(lenMax-count+1);
    end

    tempValue = y(n,find(diff(sign(diff(y(n,:))))==+2)+1);
    tempIndex =     find(diff(sign(diff(y(n,:))))==+2)+1;
    lenMin = length(tempValue);
    for count = 1:lenMin
        MinValue(n,count) = tempValue(lenMin-count+1);
        MinIndex(n,count) = tempIndex(lenMin-count+1);
    end

    if lenMax>8&&lenMin>8
         if MaxIndex(n,1)> MinIndex(n,1)
             finalValue(n,1) =
repaverge7(MaxValue(n,1),MinValue(n,1),MaxValue(n,2),MinValue(n,2),MaxV
alue(n,3),MinValue(n,3),MaxValue(n,4));
         else
             finalValue(n,1) =
repaverge7(MinValue(n,1),MaxValue(n,1),MinValue(n,2),MaxValue(n,2),MinV
alue(n,3),MaxValue(n,3),MinValue(n,4));
         end
    elseif lenMax>4&&lenMin>4
         if MaxIndex(n,1)> MinIndex(n,1)
            finalValue(n,1) =
repaverge5(MaxValue(n,1),MinValue(n,1),MaxValue(n,2),MinValue(n,2),MaxV
alue(n,3));
         else
            finalValue(n,1) =
repaverge5(MinValue(n,1),MaxValue(n,1),MinValue(n,2),MaxValue(n,2),MinV
alue(n,3));
         end
    elseif lenMax>2&&lenMin>2
         if MaxIndex(n,1)> MinIndex(n,1)
            finalValue(n,1) =
repaverge3(MaxValue(n,1),MinValue(n,1),MaxValue(n,2));
         else
            finalValue(n,1) =
repaverge3(MinValue(n,1),MaxValue(n,1),MinValue(n,2));
         end
    else
         finalValue(n,1) = y(n,cal+1);
    end

    n = n+1;
end

finalValue = finalValue';
pot = cos(k.*z).*finalValue;
```

***Subfunction* "bess"**

```
function IK = bess(m_max,xi,xk)
%clear all
%m_max = 400;
%xi = 20;
%xk = 20;

%m_top = max(m_max,x)+10;
m_top = m_max+10;
%m_top = 2*ceil(m_top/2);
Ii(m_top+1) = 0.5*1e-300;
Ii(m_top) = 1*1e-300;

index = 0;  %restore the index of Ii which needs to be reduced by 1e-
500
i = 1;
for m = m_top-1:-1:1
    Ii(m) = 2*(m)./(xi+eps).*Ii(m+1)+Ii(m+2);
    if Ii(m)>1
        Ii(m)=Ii(m)*1e-250;
        %Ii(m)=Ii(m)*1e-250;
        Ii(m+1)=Ii(m+1)*1e-250;
        %Ii(m+1)=Ii(m+1)*1e-250;
        index(i) = m+1;
        i = i+1;
    end
end

if index(1)~=0   %out of the limit of calculation
    fld = length(index);
    for n = 1:fld/2   %reverse the element in index
        temp = index(n);
        index(n) = index(fld-n+1);
        index(fld-n+1) = temp;
    end
    index(fld+1) = m_top+1;
    fld = fld+1;

    norm = zeros(1,fld);
    norm(1) = Ii(1);
    for m = 2:1:index(1)
        norm(1) = norm(1)+2*Ii(m);
    end
    for i = 2:fld
        for m = index(i-1)+1:index(i)
            norm(i) = norm(i)+2*Ii(m);
        end
    end

    norm = norm/exp(xi);
    I = Ii/(norm(1)+norm(2)*1e-250);  %first part, data no change;
backward one part, enlarged by 1e250
```

```
                    %ignore the norm(2)... 1/norm(1) over 1/norm(2)
e250
    K(1) = besselk(0,xk);
    K(2) = besselk(1,xk);
    for cont = 3:index(1)+2  %%%%What happend if index(1)<4
        K(cont) = 2*(cont-2)./(xk).*K(cont-1)+K(cont-2);
    end
    for i = 2:fld
        K(index(i-1)+1) = K(index(i-1)+1)*1e-250;
        K(index(i-1)+2) = K(index(i-1)+2)*1e-250;
        for cont = index(i-1)+3:index(i)
            K(cont) = 2*(cont-2)./(xk).*K(cont-1)+K(cont-2);
        end
        if i~=fld
            K(cont+1) = 2*(cont-1)./(xk).*K(cont)+K(cont-1);
            K(cont+2) = 2*(cont)./(xk).*K(cont+1)+K(cont);
        end
    end

else
    I = besseli(0:m_top,xi);
    K = besselk(0:m_top,xk);
end
IK = I.*K;

%correcti = besseli(0:m_max,xi);
%correctk = besselk(0:m_max,xk);
%correctik = correcti.*correctk;
```

Appendix F: Matlab program for finding the spiral profile associated with CW domain

```
% Find the Plane-Spiral equvalence along the convex
% unit: cm

clear; home;

Ro = 1;    %1.27  2.41046  5.0711
             %0.953135  2.53492
ua = 0.02;
us = 5;
A = 1.86;

D = 1/3/(us+ua);
S = 1;


%% Direct cal the value coarsely and search the spiral pattern
cal_direct = 500;
cutoff_direct = 500;

mystepX = .01;  %.05; %step size
mystepY = .01;  %.05;

z = 0; d = 0; % cal first the origin, and start search from the (0,0)
point
ylg(1,1) =
log(S/pi^2/D*quadgk(@(k)optconvex3(k,z,d,us,Ro,ua,D,A,...      %%%%%%%%%
%%%%%%%%%
    cal_direct),0,cutoff_direct));

currentX = 0;  % current coordinates
currentY = 0;
i = 2;  % start to cal errorF from errorF(2)
mystop = 0;
stpM = 1;
endmark = 0; % endmark when currentX*mystepX = 2Ro;
iter = 0; % record the calculation # in z direction when d = 2*Ro
while mystop~=1
    tempX = currentX+stpM; % move in x axis
    tempY = currentY;
    d = tempX*mystepX;
    z = tempY*mystepY;
    d_semi1 = sqrt(z^2+d^2);
    y_semi1 = log(semiFun(us,ua,D,S,A,d_semi1));
    ylg(tempY+1,tempX+1) =
log(S/pi^2/D*quadgk(@(k)optconvex3(k,z,d,...  %%%%%%%%%%%%%%%%%%
        us,Ro,ua,D,A,cal_direct),0,cutoff_direct));
    error1 = (ylg(tempY+1,tempX+1)-y_semi1)^2;

    tempX = currentX;
    tempY = currentY+1; % move in z axis
    d = tempX*mystepX;
```

```
    z = tempY*mystepY;
    d_semi2 = sqrt(z^2+d^2);
    y_semi2 = log(semiFun(us,ua,D,S,A,d_semi2));
    ylg(tempY+1,tempX+1) =
log(S/pi^2/D*quadgk(@(k)optconvex3(k,z,d,...  %%%%%%%%%%%%%%%%%%%
        us,Ro,ua,D,A,cal_direct),0,cutoff_direct));
    error2 = (ylg(tempY+1,tempX+1)-y_semi2)^2;

    [a,b] = min([error1,error2]);
    if b == 1
        currentX = currentX+stpM
        if endmark==1
            break
        end
        errorF(i) = error1;
    else
        if iter>=25  % quit if cal 25 steps in z at d=2Ro
            break
        end
        currentY = currentY+1
        errorF(i) = error2;
    end
    i = i+1;

    if currentX*mystepX==2*Ro
        % currentX is the coordinate, currentX+1 is the index
        stpM = -1;
        endmark = 1;
        iter = iter+1;
%         ylg(currentY+2,currentX+1) =
log(S/pi^2/D*quadgk(@(k)optconvex3(k,...  %%%%%%%%%%%%%%%%%
%
(currentY+1)*mystepY,2*Ro,us,Ro,ua,D,A,cal_direct),0,cutoff_direct));
        %mystop = 1;
    end
end


%% eliminate the image part in ylg
mag = size(ylg);
ylg_r = zeros(mag(1),mag(2));
for n = 1:mag(1)
    for m = 1:mag(2)
        tempReal = real(ylg(n,m));
        signFlag = sign(tempReal);
        ylg_r(n,m) = signFlag*abs(ylg(n,m));
    end
end

figure; hold on % plot the interpolaton results
dtemp = (0:1:(mag(2)-1))*mystepX;
ztemp = (0:1:(mag(1)-1))*mystepY;
mesh(dtemp,ztemp,ylg_r)
stepsizeIx
= .003; %.005;                    %%%%%%%%%%%%%%%%%%%%%%%%%%%%%%%%%%
stepsizeIy = stepsizeIx;
```

```
% Use the fixed point if the choice of stepsizeI can give a complete
% extrapolation in either ztemp direction or dtemp direction
% stepsizeIx = ((mag(2)-1)*mystepX)/30;
% stepsizeIy = ((mag(1)-1)*mystepY)/29;

[xI,yI] = meshgrid(0:stepsizeIx:((mag(2)-
1)*mystepX),0:stepsizeIy:((mag(1)-1)*mystepY));
ylg_I = interp2(dtemp,ztemp,ylg_r,xI,yI);
dtempI = xI(1,:);
ztempI = yI(:,1)';
% mesh(dtempI,ztempI,ylg_I+5)
xlabel('x-axis,d')
ylabel('z-axis,z')
zlabel('photon fluence rate')
axis equal


%% Search the spiral pattern
xlengthI = length(dtempI);
ylengthI = length(ztempI);

currentX = 0;  % current coordinates
currentY = 0;
%spiralX = zeros(1,ylengthI); % x coordinate of the spiral
%spiralY = zeros(1,ylengthI); % y coordinate of the spiral

mystop = 0;
i = 2;  % first point for spiralX and spiralY is (0,0)
while mystop~=1
    tempX = currentX+1;
    tempY = currentY;
    d_semi1 = sqrt((tempX*stepsizeIx)^2+(tempY*stepsizeIy)^2);
    y_semi1 = semiFun(us,ua,D,S,A,d_semi1);
    y_semi1 = log(y_semi1);
    ylg_conc1 = ylg_I(tempY+1,tempX+1);
    error1 = (ylg_conc1-y_semi1)^2;

    tempX = currentX;
    tempY = currentY+1;
    d_semi2 = sqrt((tempX*stepsizeIx)^2+(tempY*stepsizeIy)^2);
    y_semi2 = semiFun(us,ua,D,S,A,d_semi2);
    y_semi2 = log(y_semi2);
    ylg_conc2 = ylg_I(tempY+1,tempX+1);
    error2 = (ylg_conc2-y_semi2)^2;

    tempX = currentX+1;
    tempY = currentY+1;
    d_semi3 = sqrt((tempX*stepsizeIx)^2+(tempY*stepsizeIy)^2);
    y_semi3 = semiFun(us,ua,D,S,A,d_semi3);
    y_semi3 = log(y_semi3);
    ylg_conc3 = ylg_I(tempY+1,tempX+1);
    error3 = (ylg_conc3-y_semi3)^2;

    [a,b] = min([error1,error2,error3]);
    if b == 1
```

```
        currentX = currentX+1;
        d_semi(i) = d_semi1;
        y_semi(i) = y_semi1;
        ylg_conc(i) = ylg_conc1;
        errorF_I(i) = error1;
    elseif b==2
        currentY = currentY+1;
        d_semi(i) = d_semi2;
        y_semi(i) = y_semi2;
        ylg_conc(i) = ylg_conc2;
        errorF_I(i) = error2;
    else
        currentX = currentX+1;
        currentY = currentY+1;
        d_semi(i) = d_semi3;
        y_semi(i) = y_semi3;
        ylg_conc(i) = ylg_conc3;
        errorF_I(i) = error3;
    end

    spiralX(i) = currentX;
    spiralY(i) = currentY;
    i = i+1;

    if (currentX+2>xlengthI)||(currentY+2>ylengthI)
        % currentX is the coordinate, currentX+1 is the index
        mystop = 1;
    end
end


%% draw the cylinder and the spiral pattern
figure;  % plot the pattern on the photon fluence rate map
mesh(dtempI,ztempI,ylg_I)
hold on
xlabel('x-axis,d')
ylabel('z-axis,z')
zlabel('photon fluence rate')
for n = 1:length(spiralY)  % spiralY and spiralX should have the same
length
    magni_temp(n) = ylg_I(spiralY(n)+1,spiralX(n)+1);
end
d_vector = spiralX*stepsizeIx;
z_vector = spiralY*stepsizeIy;
plot3(d_vector,z_vector,magni_temp,'ok')
axis equal
hold off

figure;  % plot based directly on d and z
plot(d_vector,z_vector,'.')
title('plot based directly on d and z')
axis equal

figure; % plot on the z and theta map
phi = 2*asin(d_vector/2/Ro);
plot(phi,z_vector,'.')
```

```
title('plot on the d and theta map')
axis equal

figure;  % plot based on the flatened cylinder surface
phi_vector = 2*asin(spiralX*stepsizeIx/2/Ro);
d_flattened = phi_vector*Ro;
plot(d_flattened,z_vector,'.')
title('plot based on the flatened cylinder surface')
axis equal

figure;  % plot the sprial pattern onto the cylinder
z_cylin = linspace(-14*Ro,14*Ro,40);  % a cylinder with height from -12
to 12
theta = linspace(0,2*pi,40);
[z_cylin,theta] = meshgrid(z_cylin,theta);
x_cylin = Ro*cos(theta);
y_cylin = Ro*sin(theta);
hSurf = surf(x_cylin,y_cylin,z_cylin,'EdgeColor','none','LineStyle',...
    'none','FaceLighting','phong');
set(hSurf,'FaceColor',[0 0 0],'FaceAlpha',0.1);
xlabel('x-axis')
ylabel('y-axis')
zlabel('z-axis')
hold on
x_vector = Ro*cos(phi_vector);
y_vector = Ro*sin(phi_vector);
plot3(x_vector,y_vector,z_vector);
axis equal
title('plot the sprial pattern onto the cylinder')
hold off


%%% lie the cylinder and draw the plot
figure;  % plot the sprial pattern onto the cylinder
x_cylin = linspace(-16*Ro,16*Ro,40);  % a cylinder with height from -12
to 12
theta = linspace(0,2*pi,40);
[x_cylin,theta] = meshgrid(x_cylin,theta);
y_cylin = Ro*cos(theta);
z_cylin = Ro*sin(theta);
hSurf = surf(x_cylin,y_cylin,z_cylin,'EdgeColor','none','LineStyle',...
    'none','FaceLighting','phong');
set(hSurf,'FaceColor',[0 0 0],'FaceAlpha',0.1);
xlabel('x-axis')
ylabel('y-axis')
zlabel('z-axis')
hold on
x_vector = Ro*cos(phi_vector);
y_vector = Ro*sin(phi_vector);
plot3(z_vector,y_vector,x_vector);
plot3(-z_vector,y_vector,x_vector);
plot3(z_vector,-y_vector,x_vector);
plot3(-z_vector,-y_vector,x_vector);
axis equal

figure;  % plot the comparison between semi and concave/convex
```

```
plot(d_semi,y_semi,d_semi,ylg_conc,'.r')
ylabel('log(I)')
xlabel('source-detector distance')
legend('semi-infinite','concave/convex results')
```

VITA

ANQI ZHANG

Candidate for the Degree of

Doctor of Philosophy

Thesis: INVESTIGATIONS ON TRANS-LUMINAL PHOTON DIFFUSION IN STEADY-STATE AND FREQUENCY-DOMAIN

Major Field: Electrical Engineering

Biographical:

Education:

Completed the requirements for the Doctor of Philosophy in Electrical Engineering at Oklahoma State University, Stillwater, Oklahoma in December, 2012.

Completed the requirements for the Master of Science in Radio Physics at East China Normal University, Shanghai, China in 2008.

Completed the requirements for the Bachelor of Science in Electronic information science & technology at East China Normal University, Shanghai, China in 2005.

Experience:

Research Assistant August 2008 - Present
School of Electrical and Computer Engineering, Oklahoma State University, Stillwater, OK

Research Assistant February 2005 - August 2008
Microwave Research Institute, East China Normal University, Shanghai, China

Graduate Research Intern August 2007 - October 2007
Atten Electronics Co., Ltd. Shanghai, China

Professional Affiliation:
Student member Optical Society of America (OSA) 2010- Present
Student member The International society of Optical Engineering (SPIE) 2010- Present